ABSTRACT

Title of Document: STUDY OF LONGITUDINAL SPACE CHARGE WAVES IN SPACE-CHARGE DOMINATED BEAMS

Jayakar Charles Tobin Thangaraj,
Doctor of Philosophy, 2009

Directed By: Prof. Patrick O'Shea
Prof. Rami A. Kishek
Department of Electrical and Computer Engineering

Future x-ray free electron lasers will probe matter at the atomic scale with femtosecond time resolution. Such x-ray sources require a high current electron beam with very low emittance and energy spread. Any density fluctuation in an intense beam can launch space charge waves that lead to energy modulation. The energy modulations may cause further density modulations in any dispersive element and can, for example, excite the microbunching instability in x-ray free electron lasers. Hence, it is important to understand and control the evolution of density modulations on an intense beam. This dissertation focuses on long path-length experimental study of intense beams with density perturbations. The experimental results are compared with theory and computer simulation.

We took advantage of the multi-turn operation of the University of Maryland Electron Ring (UMER), to carry out long path-length (100 m) experimental studies of space-charge-dominated beams with density perturbations. First, a single density

perturbation is introduced on a space-charge dominated electron beam using photoemission from a laser. The perturbation splits and propagates as a fast and a slow wave on the beam. The speed of the space charge waves is measured experimentally as a function of beam current and perturbation strength. The results are in good agreement with Particle-in-cell (PIC) simulation and 1-D cold fluid theory in the linear regime. We then show that linear space-charge waves can be used as non-interceptive transverse beam diagnostics in UMER. Using time-resolved imaging techniques, we report the transverse effects of a longitudinal perturbation in a circular machine.

We introduce multiple perturbations on the beam and show that the fast and the slow waves superpose and cross each other. We then present experimental results on the beam response from introducing a controlled energy modulation on the density modulated beam and compare them with the theory. In the non-linear regime, where the strength of the perturbation is large (>25% compared to the beam current), we report, for the first time, a wave train formation of the space charge waves. Finally, experimental observation of a photo-emitted beam pulse splitting into sub-pulses under high laser power is presented and compared with 1-D virtual cathode theory.

From this work, we conclude that density modulations on an intense beam produce fast and slow waves, which, in the linear regime at least, can be controlled through energy modulation. Moreover, a large amplitude density modulation, when allowed to propagate, can break into sub-pulses, causing energy modulation. Hence, a density modulation should not be allowed to grow and must be controlled as soon as possible.

STUDY OF LONGITUDINAL SPACE CHARGE WAVES IN SPACE-CHARGE DOMINATED BEAMS

By

Jayakar Charles Tobin Thangaraj

Dissertation submitted to the Faculty of the Graduate School of the
University of Maryland, College Park, in partial fulfillment
of the requirements for the degree of
Doctor of philosophy
2009

Advisory Committee:
Professor Patrick O'Shea, Chair/ Advisor
Professor Rami Kishek, Co-Advisor
Professor Victor Granatstein
Professor Kristine Rosfjord
Professor Richard Ellis

Dedication

To my beloved family,

Joshua Daniel Thangaraj,

Beulah Thangaraj,

Jeromie Wesley Vivian

Acknowledgements

I thank the Lord God Almighty for providing me with the good fortune to meet many people who have inspired me with their creativity, their compassion and their courage. First and foremost is my advisor Prof. Patrick O'Shea, who leads one of the top engineering schools in the nation, but still took time for my research work. He has motivated me to relish the scientific spirit of exploring unknown challenges in research and to pursue excellence in my professional work. Prof. Kishek has been my mentor and a brilliant scientist. His style of problem-solving, presenting ideas and writing have influenced me heavily. He taught me persistence and motivated me to strive for clarity and to bring this thesis to fruition.

This dissertation is an experimental work involving many people. First, I would like to thank Don Feldman for his guidance from day one. He was with me every single day of the experiment and was an inspiration. His patience coupled with his eye to experimental details has made him a joy to work with. I miss Renee Feldman who enquired about my family and helped me with data processing. I would like to thank Santiago and Brian for keeping the machine running. Santiago is a superb experimental physicist. He taught me that experimental physics is hard but rewarding. I will never forget that lesson. I enjoy his physics conversations peppered with jokes and stories. Brian has been a great friend and always wanted me to succeed. I went home happy after many challenging experiments because of him. I also thank Dave Sutter for helping with dispersion calculations among other things. Whenever I travel to accelerator conferences and physics meetings around the world,

there is always someone asking for Dave! A major achievement in this work is the experimental evidence of solitary waves in beams and I thank Haber for his simulation confirming my findings. I thank Prof. Reiser for the whole idea of UMER that was born from his lifetime of research. He is both an inspiring physicist and a leader in the field. His book is invaluable.

The last year of my research work involved people in Linac Coherent Light Source in Stanford, California and FERMI@Elettra, Italy. I am greatly indebted to Max Cornacchia for this. Max joined the group, instantly recognized my work and involved me with these labs. His expertise along with his cheerful disposition and his enthusiasm for research is stimulating. His leadership was invaluable while we worked on the microbunching instability. I also thank Fiorito and Anatoly for their support for Coherent Optical Transition Radiation research while I was here and abroad.

I also thank all the UMER graduate students, both past and present, especially Mike, Mark and Quinn. I thank Chris, Diktys, Chao and Kai for their support. Thanks to Eric Voorhies for painstakingly proofreading the draft. I greatly enjoyed his historical anecdotes. I also thank the IREAP and ECE staff for their administrative assistance. Last but not least, I would like to thank Prof. Eugenia Kalnay who provided me with complete support during my first year. I enjoyed working with all of them.

I thank my church, Indians for Christ (IFC) for helping me throughout these years. I thank my Pastor Rev. Lite and his family for they took care of me as their

own son. I thank Valentine and Sheba for their generosity and helping me in every single situation through all these years. Fridays with Noble and Chamini have always been filled with love and affection. I thank Mano and Shanthi for they have shown what Christian love is all about with their example. I am greatly indebted to all of them for the rest of my life. I can only aspire to be of such an influence toward someone else. There are many others in the church who have helped me including the Edwins, Bhaskarans, Henrys, Prems and the James family. Regi mentored me during my tough times. His helping nature and positive attitude toward life are inspiring. I am grateful for Regi and Daniel Sumanth for their constant dose of encouragement.

I thank my friend Deepak who taught me to think independently and who has been a great influence. Deepak and Jyoti have provided me with a positive and accepting environment that I have been searching for. I am very grateful to them and the only way to thank them would be to do what they have done for me for someone else. I thank Rahul who has been an understanding friend. I thank Thangamani whom I will miss, for he always shared my success as his very own. I thank Ashwin and Mahesh for their help, especially during my initial years at Maryland. I thank my best friend Satish for motivating me throughout graduate school. I owe my interest in physics research to Dr. Murali from my alma mater Anna University. I thank my parents and teachers who always motivated me to excel in academics and pursue knowledge.

I thank the Department of Energy and the Office of Naval Research and Joint Technology office for supporting our research.

Table of Contents

List of Tables

List of Figures

Chapter 1: Introduction

There is a growing demand for short wavelength free electron lasers (FELs), which have unprecedented brightness and temporal properties for probing biological and material structures [1-4]. Short wavelength FELs place very tight constraints on the quality of the electron beam required for operation. Advanced accelerators like high-luminosity colliders and high energy-recovery linacs also demand both high energy and superior beam quality [5, 6]. Space charge plays a major role in the generation and propagation of high-quality beams. Understanding the role of space-charge in such beams will be pivotal in the design and operation of modern machines. Near the cathode, all beams of interest begin as space-charge dominated beams. As the beam is accelerated to relativistic energies, any beam quality degradation that occurred at low energy, where the collective effects dominate the dynamics, will remain at high energies. Hence, to maintain the beam quality of bright beams throughout the beam transport line, it is important to identify the factors degrading the beam quality at low energy and control them.

As an example, X-ray free electron lasers (XFELs) require a high current beam with a low emittance and a low energy spread. Any density perturbations on the longitudinal distribution can induce energy modulations on the beam through space charge forces at low energies. Such induced energy modulations may lead to density modulations at higher energies when the beam passes through a dispersive section such as bunch compressor, possibly leading to microbunching instability [7, 8]. This instability can adversely affect the operation of the XFEL. Therefore, it is important

to generate and transport a uniform and stable longitudinal current distribution. As another example, in ion machines, where the beam for the most part is space charge dominated, any fluctuations on the beam can cause resistive wall instability, leading to unacceptable energy spread.

Upon their generation at the cathode, beams typically have density modulations, velocity modulations, or both. Some of the sources of these perturbations are the drive laser fluctuations in a photoinjector, RF modulations, cathode non-uniformity, shot noise or impedance mismatch in the transport lines. These modulations can be desirable or undesirable, depending on the application.

By pre-modulating a beam, say at mm-wave or THz frequencies, an efficient radiation source can be implemented. For certain applications like XFEL, where the beam quality is critically important, such beam modulation can be undesirable. In a high brightness beam, initial density modulations on the beam get converted into energy modulations and hence distort the longitudinal phase space. This will cause emittance growth and thus reduce FEL output. Moreover, the microstructures inside the beam can radiate coherently when passing through a bend, thereby introducing energy modulation. This microbunching instability, currently observed in the Linac Coherent Light Source (LCLS) as Coherent Optical Transition Radiation (COTR) [9], may potentially degrade the beam quality and is undesirable for seeded machines like FERMI@Elettra [10]. Bright COTR may swamp OTR radiation and therefore prevent the use of OTR as a diagnostic tool [11].

One of the goals of the University of Maryland Electron Ring (UMER) is to study beams in such a non-ideal state. In this work, we deliberately introduce a stable,

localized, density perturbation on a space charge dominated beam and observe its evolution over a long path length.

1.1 *Previous work on Space-Charge Waves*

Space-charge wave studies began with microwave generation during the 1950's. Research on space charge waves in beams continued with the Heavy Ion Fusion research [12, 13]. In the 1990's, J.G. Wang [14, 15] and D.X. Wang [16] worked on several experiments on the Maryland Electron Beam Transport (MEBT) facility. In their experiments, they generated perturbations by modulating the grid-voltage of an electron gun. They measured the phase velocity of the space charge waves and found good agreement with 1-D cold fluid theory and experiment. They also observed the space charge waves reflecting off the beam edges [17]. Their work was done in a beam pipe with a conducting wall.

Suk [18] found a good agreement of the growth rate of the slow space charge wave with cold fluid theory in the linear regime. In the linear regime, the strength of the perturbation is small compared to the main beam current. Similarly, Zou [19] observed the energy width of the slow wave growing and of the fast wave decaying. A theory on the possibility of launching solitary waves in a space charge dominated beam was also developed [20].

Further work was done by Neumann [21] who used a pre-modulated beam to generate radiation. On UMER, Huo [22] demonstrated generating perturbations using a UV laser and found good agreement between theory, simulation, and experiment for the wave velocity in the linear region under various initial conditions. Also, on UMER, Harris and Neumann [23, 24] investigated generating perturbations in the

UMER gun both by modulating the cathode and by using photoemission from a laser. Tian [25] has observed initial density modulations getting converted into energy modulations through space-charge waves in current space as well as velocity space in the Long Solenoid Experiment (LSE) facility.

Although these experiments revealed information about space charge wave propagation in intense beams, the experiments were limited in two aspects. First, the beam transport in all these experiments was limited to 10 meters or less. A longer transport distance has an advantage of increasing data resolution by probing the space charge waves for a longer time and also allows long path length experiments. Secondly, when introducing a perturbation on the beam by modulating the grid voltage of an electron gun, both the energy and the density of the beam are modulated and this makes it difficult to know the exact initial conditions. A pure density or a pure velocity modulation on the electron beam can simplify the initial conditions.

Therefore, in this work we first extend the studies on a longer distance and secondly introduce a pure density modulation to simplify the initial conditions. We conduct our experiments on the University of Maryland Electron Ring [26, 27], which is a circular machine 11.52 m in circumference. Even modest multi-turn operation of UMER makes it is possible to conduct experiments over path lengths much longer than 100m compared to 5-m of previous experiments. Secondly, in our experiments we introduce a density modulation using photoemission from a laser. With the use of a laser, we can introduce a localized charge modulation without changing the velocity of the electron beam. Using multiple lasers, we extend this technique to introduce multiple perturbations on the beam. We also report the observation of space charge induced instabilities above a critical value of the laser power. Though such effects

have been observed before in photoinjectors [28, 29], we compare our observations with theory and discuss the relevance of such effects for future photoinjectors. As of this writing, Beaudoin [30] introduced energy modulations on a space-charge dominated beam, using an induction cell, and found good agreement between theory, measurement and simulation over a distance of 60 meters in UMER.

The outline of this chapter is as follows. We begin by a brief overview of 1-D cold fluid theory in Section 1.1. We then discuss the longitudinal geometry factor in Section 1.2 and sound speed in Section 1.3. We discuss the limitation of the 1-D cold-fluid theory in Section 1.4 and extend it to nonlinear regime in Section 1.5 and we finally conclude in Section 1.6 with the organization of the thesis.

1.2 One-dimensional cold fluid theory

The cold fluid theory is derived by truncating the hierarchy of fluid equations. This truncation is done by assuming a cold beam without energy spread. Since the theory treats the beam as a fluid, the fluid model is suitable to explain phenomena which are inherently fluid in nature like wave propagation and wave growth. The fluid equations are obtained by taking moments of the Vlasov equations. We refer to [31] for details of Vlasov equation and its moments. We begin with the continuity equation (1.1) and the momentum equation(1.2).

$$\frac{\partial(\lambda v)}{\partial z}+\frac{\partial \lambda}{\partial t}=0 \tag{1.1}$$

$$\frac{\partial v}{\partial z}v_0+\frac{\partial v}{\partial t}=\frac{qE_z}{\gamma_0^3 m} \tag{1.2}$$

Let us assume that the initial perturbation is small compared to the beam. This allows the equations to be linearized later on. The symbols used in the equation are described in Table 1-1 .

Table 1-1: Table referring to the quantities used in 1-D cold fluid theory

Symbol used	Quantity referred
q	Charge of an electron (-1.6x10^{-19}C)
z	Distance along the beam (m)
t	Time (s)
λ	Line charge density (C/m)
I	Beam current (A)
υ	Velocity of the beam (m/s)
γ	Gamma factor of the beam
m	Mass of an electron (kg)
Ez	Longitudinal electric field (V/m)
p(t)	Function representing the perturbation
K	Perveance
β	Ratio of beam velocity to the velocity of light
a	Transverse Beam size (m)
b	Beam pipe radius (m)

In our experiment, we introduce a pure charge density perturbation that can be expressed in the form:

$$\lambda_1(z,t) = \lambda_1(z=0,t) = \eta\lambda_0 p(t), \tag{1.3}$$

where η is the amplitude of the density perturbation relative to the main beam current, λ_0 and λ_1 are the non-perturbed and perturbed values of line charge density. $p(t)$ is a smooth function with unit amplitude and it represents the shape of the perturbation. Since it is a pure density perturbation, $\upsilon_1(0,t)=0$, where υ_1 is the perturbed velocity. The initial perturbation current can then be expressed as:

$$\begin{aligned} I_0 + I_1 = \lambda\upsilon &= \lambda_1\upsilon_0 + \lambda_0\upsilon_0 \\ &= \eta\lambda_0 p\left(t\right)\upsilon_0 + I_0(0,t) \\ &= I_0\eta\, p(t) + I_0 \\ \Rightarrow I_1(0,t) &= \eta I_0\, p(t), \end{aligned} \tag{1.4}$$

,where I_1 is the perturbed current. Equation (1.4) shows that a pure charge modulation converts to a beam current modulation of same strength. For a pure initial density modulation, the linearized continuity and momentum equations are reduced to the following set of equations.

$$\upsilon_0 \frac{\partial\lambda_1}{\partial z} + \frac{\partial\lambda_1}{\partial t} + \lambda_0 \frac{\partial\upsilon_1}{\partial z} = 0 \tag{1.5}$$

$$\begin{aligned} \frac{\partial\upsilon_1}{\partial t} + \upsilon_0 \frac{\partial\upsilon_1}{\partial z} &\simeq \frac{qE_z(z,t)}{\gamma_0^3 m} \\ &= -\frac{qg}{4\pi\varepsilon_0\gamma_0^5 m}\frac{\partial\lambda_1(z,t)}{\partial z} \end{aligned} \tag{1.6}$$

The geometry factor, g , given by $g=\alpha+2\ln\frac{b}{a}$, represents the dependence of the longitudinal electric field on the transverse beam properties with "*b*" being the beam

pipe radius and "*a*" the transverse beam radius and α is a constant ranging from 0 to 1. A complete derivation of these equations is shown in [31] .

1.3 Longitudinal Geometry factor (g-factor)

Initial work [32] used a uniform beam model with a constant radius leading to a value of α=0.5. But this assumption breaks down for perturbations in a space-charge dominated beam because in a space-charge dominated beam it is the volume charge that remains constant while the radius changes with the variation of the line-charge density. To show this, let us calculate the line-charge density for a uniform beam of radius *a* and volume charge density ρ. The line-charge density λ is

$$\lambda(z) = \pi a^2(z)\rho(z) \tag{1.7}$$

In a machine with a periodic focusing lattice like UMER, the average matched radius of the beam, which depends on the wave constant k_0 of the focusing lattice, the perveance K and the emittance ε, is approximately given by

$$a \approx \left(\frac{K}{k_0^2} + \frac{\varepsilon}{k_0} \right)^{\frac{1}{2}} \tag{1.8}$$

The equation (1.8) is obtained from equation 5.293 of [31]. The relation is exact only for either a zero emittance beam (ε=0) or beam with negligible space charge (K=0). Combining (1.7) and replacing perveance with beam current, we get:

$$a^2 = \frac{\lambda(z)}{2\pi\varepsilon_0\beta^2\gamma^3 k_0^2 \left(\frac{mc^2}{e} \right)} + \frac{\varepsilon}{k_0} \tag{1.9}$$

If the beam is emittance-dominated such as beams in a high energy accelerator, then the beam size will be determined by the second term in equation(1.8), then

$$a^2 = \frac{\varepsilon}{k_0} = constant \qquad (1.10)$$
$$\Rightarrow \lambda(z) = \pi\rho(z)a^2$$

In this case, modulating the charge density is essentially modulating the volume charge density in an emittance-dominated beam with a constant beam radius.

But, if the beam is space-charge dominated, which is the situation in high-brightness injectors, then the first term in equation (1.8) dominates leading to

$$a^2(z) = \frac{\lambda(z)}{2\pi\varepsilon_0\beta^2\gamma^3 k_0^2\left(\frac{mc^2}{e}\right)} = \frac{\pi a^2(z)\rho(z)}{2\pi\varepsilon_0\beta^2\gamma^3 k_0^2\left(\frac{mc^2}{e}\right)} \qquad (1.11)$$
$$\Rightarrow \rho(z) = constant$$

In this case, the volume charge density remains constant. This means any variation in the line-charge density on the beam changes the beam size accordingly to keep the volume charge density a constant. This is a very important feature of space-charge dominated beams causing a change in g-factor. The value of α in the g-factor formula for a space-charge dominated beam was measured experimentally [15] showing it be equal to zero. Hence, the g-factor for a space-charge dominated beam of radius *a* inside a pipe of radius *b*, is given by

$$g = 2\ln\frac{b}{a} \tag{1.12}$$

Because the g-factor is different between the space-charge dominated beam and the emittance-dominated beam, there is a difference in the longitudinal electric field E_z produced by the waves in those beams. From equation(1.6), the longitudinal electric field E_z is

$$E_z(z,t) \propto g\frac{\partial\lambda_1(z,t)}{\partial z} \tag{1.13}$$

In the case of an emittance dominated beam, the beam size *a(z)* is constant along the beam and so the E_z field is a function of radius r across the beam, so $E_z(r,z)=E_z(r)$. But when the space-charge forces dominate, the longitudinal field E_z is constant across the beam radius and changes along the beam, so $E_z(r,z)=E_z(a(z))$. In high brightness photoinjectors, density modulations can create longitudinal space charge fields in the beam leading to rapid transverse beam size variation across the beam. So, any efforts to model the physics of the beam inside modern photoinjectors should take the radial dependence of longitudinal space-charge forces into account [33].

1.4 Sound Speed of the fast and slow space-charge waves

Solving the linearized fluid equations (1.5) and (1.6) along with Maxwell's equation [31] in the beam frame, we obtain a wave solution for the perturbation

current ,velocity and charge density. The solution in the beam frame can be expressed as:

$$I_1(z,t) = \frac{\eta I_0}{2}\left[1-\frac{c_s}{v_0}\right]p(t+\frac{z}{c_s}) + \frac{\eta I_0}{2}\left[1+\frac{c_s}{v_0}\right]p(t-\frac{z}{c_s}) \tag{1.14}$$

$$v_1(z,t) = \frac{-\eta c_s}{2}\,p(t+\frac{z}{c_s}) + \frac{\eta c_s}{2}\,p(t-\frac{z}{c_s}) \tag{1.15}$$

$$\lambda_1(z,t) = \frac{\eta \lambda_0}{2}\,p(t+\frac{z}{c_s}) + \frac{\eta \lambda_0}{2}\,p(t-\frac{z}{c_s}) \tag{1.16}$$

The solution shows that the density perturbation propagates along the beam in the form of waves, one of which has a phase velocity greater than the beam velocity and hence is called the fast wave, while the other one has a phase velocity smaller than the beam velocity and hence is called the slow wave. Here

$$C_s = \sqrt{\frac{qg\Lambda_0}{4\pi\varepsilon_0 m\gamma^5}} \tag{1.17}$$

is the velocity of the space charge waves in the beam frame, in analogy to the propagation of sound in a gas and hence is called the "sound speed". Equations from (1.14) through (1.16) reveal some of the properties of the space-charge waves. First, the fast wave has higher amplitude than the slow wave in the perturbed beam current as seen in equation(1.14). The polarity of the fast and the slow waves are both positive in the density space (equation(1.16)) while they are opposite in velocity space (equation(1.15)). This is a fundamental difference between a density

perturbation and an energy perturbation. In the latter, the fast and the slow waves have positive polarity in the velocity space and have opposite polarity in the density space [30]. Finally, the space charge waves have the same shape as that of the initial perturbation. The same conclusion can also be arrived by constructing the dispersion relation for the space charge waves

$$\begin{aligned} &\omega = k(\upsilon_0 \pm C_s) \\ &\Rightarrow \left(\frac{\partial \omega}{\partial k}\right)_{group\ velocity} = \upsilon_0 \end{aligned} \tag{1.18}$$

where k is the wave constant of the perturbation. The dispersion relation shows that the group velocity is equal to the phase velocity of the waves meaning the space charge waves are dispersion free.

1.5 Limitations of the cold-fluid theory

Both the cold-fluid theory and the g-factor model have some limitations in their validity. First, the cold-fluid theory assumes a cold beam with zero energy spread. Also, the linearization of the continuity and momentum equation means the amplitude of the perturbations is assumed to be small compared to the beam current: i.e. $\lambda_1 << \lambda_0$. Additional terms must be taken into account if the perturbation is sufficiently large compared to the small amplitude perturbation approximation.

The g-factor model has at least two limiting cases. First, the g-factor model cannot be applied near beam ends where the line-charge density changes rapidly in a short distance thereby violating the assumption of uniform beam density. Secondly, the g-factor calculation changes significantly for highly compressed beams. This is also called the short-wavelength limit - when the wavelength of the perturbation is

comparable to the dimension of the beam radius or pipe radius ($\lambda_{pert} \approx a_{beamsize}$). For an ultra-short beam bunch the beam length is comparable to the pipe radius. So any perturbation on such a short beam affects the overall E_z-field of the beam causing the g-factor to be a function of the wavelength of the perturbation.

Only in the long-wavelength limit of $\lambda_{pert} \gg a_{beamsize}$ does the g-factor become independent of the wavelength of the perturbation.

In UMER, we introduce a 5-ns perturbation (28 cm long) on a 100-ns (5.6 m long) coasting beam with a beam pipe radius of one inch (2.54 cm) and hence we operate in the long-wavelength limit. The density perturbation will be introduced near the beam center where the charge density is uniform. Hence the g-factor model is a valid model for calculating the space-charge wave velocity in our experiments.

There are also other longitudinal space charge wave models beside cold-fluid theory that take a gas-dynamic approach with an adiabatic equation and an index [34].

As seen from eqn(1.15), a pure density modulation introduces a modulation in velocity. The sound speed varies as $\gamma^{-2.5}$. As the beam is accelerated, C_S decreases very fast according to eqn(1.17). This implies that in an accelerated beam, the waves slow down and the modulations are essentially frozen in the beam. Such frozen energy modulations can still get converted into further density modulation when the beam passes through a dispersive section. In proton machines, where the beam for the most part is space-charge dominated, such perturbations can lead to large energy spread and wave-growth leading to instabilities.

1.6 Nonlinear waves, Korteweg-de Vries equation and Burgers equation:

Previous studies predicted that a space-charge dominated electron beam is capable of supporting solitary waves and wavebreaking[35, 36]. Detailed mathematical analysis shows that the 1-D cold fluid theory can be reduced to a more general form of the Korteweg-de Vries Equation (KdV) equation[37]. The KdV equation describes wave propagation in physical phenomena ranging from water waves to solitary wave transport.

We extend Suk's analysis to the specific case of *non-dispersive, non-linear* wave transport and show that it reduces to the inviscid Burgers' equation. The Burgers' equation is a partial differential equation that exhibits shock waves solutions for smooth sinusoidal initial conditions.

We begin with the classical Korteweg-de Vries equation for the line-charge density [35]:

$$\frac{\partial \lambda_1}{\partial t} + c_1 \lambda_1 \frac{\partial \lambda_1}{\partial z} + c_2 \frac{\partial^3 \lambda_1}{\partial z^3} = 0, \tag{1.19}$$

Where λ_1 is the line-charge density of the perturbation and the arbitrary coefficients c_1 and c_2 describe the nonlinear effect and the dispersion term respectively. In our case, as mentioned before we are in the long-wavelength limit and hence we assume a non-dispersive or weakly dispersive medium. Thus equation (1.19) reduces to

$$\frac{\partial \lambda_1}{\partial t} + \lambda_1 \frac{\partial \lambda_1}{\partial z} = 0, \tag{1.20}$$

where we have made c_1=1 for convenience. Equation (1.20) is the classical inviscid Burger equation. We will discuss this equation and its relevance for wave train formation in Chapter 4.

1.7 Organization of the thesis

The outline of the thesis is as follows:

In Chapter 2, we discuss the experimental setup, and the beam diagnostics that are used in this work.

In Chapter 3, we begin by presenting experimental results on the evolution of a single density perturbation under various initial conditions. We then compare the results with PIC simulation and 1-D theory. We show how space-charge waves can be used as a non-interceptive, transverse beam diagnostic. We also present time-resolved measurement of the transverse effects of longitudinal perturbation.

In Chapter 4, we present experimental study on the evolution of multiple perturbations on the beam and compare with PIC simulation. We then demonstrate experimentally how energy modulation can be used to cancel a fast or a slow wave from a density modulation. Experimental results of a large amplitude perturbation and wave breaking are discussed with a simple theory to explain the nonlinear behavior.

In Chapter 5, we investigate sub-pulse formation in the photo-emitted beam pulse when the laser power is increased above a certain value. We briefly discuss the 1-D virtual cathode theory and the short-pulse Child-Langmuir limit and conclude by extending our results to a high gradient gun.

In Chapter 6, we summarize the dissertation work and then suggest possible ideas for future work in understanding the behavior of longitudinal dynamics of space-charge dominated beams.

Chapter 2: EXPERIMENTAL SETUP, DIAGNOSTICS AND THE UNIVERSITY OF MARYLAND ELECTRON RING

In this chapter we briefly discuss, the University of Maryland Electron Ring (UMER) [26, 27, 38, 39], which forms the centerpiece of the apparatus used for this work. UMER is a circular machine with a circumference of 11.52 m. It uses a 10-keV electron beam with other scaled beam parameters. The primary scientific goal of the machine, among other things, is to investigate the effects of space charge forces on intense beams among other things. By using a scaled, low-energy electron beam, UMER deliberately enhances space charge effects and is able to model high-brightness injectors but at a lower cost. Most modern and proposed future machines, as described earlier, use bright beams, therefore, understanding space charge effects is important for their successful commission and operation. UMER parameters of interest are listed in Table 2-1.

After the first multi-turn operation of UMER [40] and subsequent developments in the steering algorithms [41], UMER is capable of transporting the low current beam (0.55mA) to more than two kilometers and the high current beam (χ=0.9) to 100-m. In this thesis, we focus on longitudinal dynamics and hence will only describe those parts of the machine that are directly relevant to the work. The history and the details of the machine progress over the years are provided in [31].

In this chapter, after providing a brief overview of UMER in section 2.1, we discuss the UMER gun in section 2.2, the laser setup in section 2.3, the UMER beam diagnostics in section 2.4 and finally summarize in section 2.5.

2.1 University of Maryland Electron Ring (UMER)

The layout of the University of Maryland Electron Ring (UMER) is shown in Figure 2.1 and some important parameters of the machine is listed in Table 2-1.

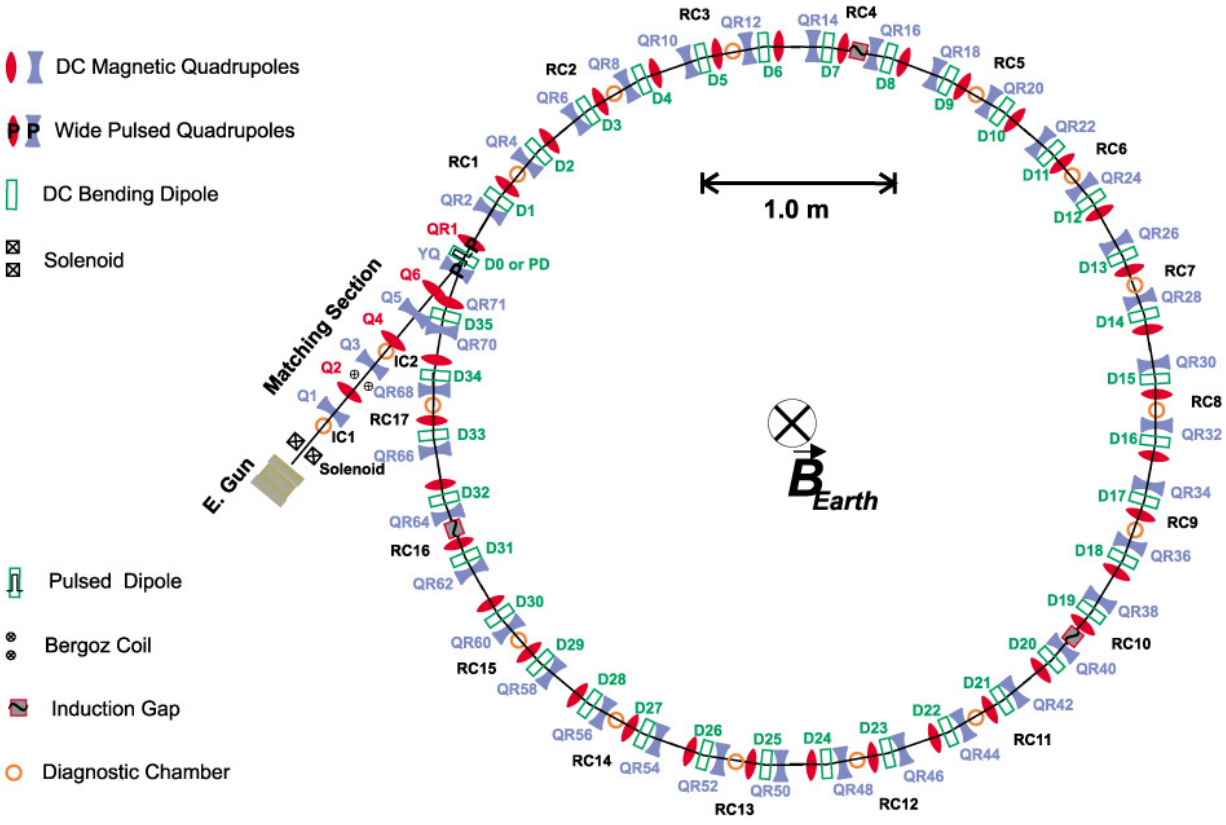

Figure 2.1: The layout of the University of Maryland Electron Ring (top view).

Table 2-1: Beam and lattice parameters of UMER

Beam Energy	10 keV (γ=1.02)
β (= beam velocity/speed of light)	0.2
FODO Period	0.32 m
Circulation time	197 ns
Pulse length	120-5 ns
Beam current	0.55 - 100 mA
Circumference	11.52 m

UMER employs a thermionic gun, the details of which are given in the next section. The UMER gun is followed by a 1.4 m injection line containing a solenoid and six matching quadrupoles. A Bergoz fast current transformer, located 64 cm from the anode plane of the gun section, is used to measure the beam current before injection into the ring. The UMER ring section consists of 36 FODO cells, with a periodicity of 32 cm, distributed over the 11.52 m circumference. As shown in the figure, there are three glass gaps for induction modules, which can provide electric fields for longitudinally focusing the beam. Out of these three glass gaps, two house a wall current monitor. Beam position monitors, one per section except the three glass gaps, are used to measure and steer the beam centroid through a computer-controlled LabView interface.

2.2 UMER Gun

The UMER gun has a thermionic dispenser cathode, which is made of a porous tungsten (W) matrix impregnated with barium oxide and calcium aluminate. While the cathode is typically operated at a temperature of 900^0C as a thermionic gun, it can also be used as a photocathode [42]. The dispenser photocathode provides the flexibility to simultaneously generate electrons using both thermionic emission and photoemission. The gun has a Pierce geometry cathode and anode with a grid placed between them. A general feature of these electrodes is: they make an angle of 67.5 to the beam edge [43]. By shaping the electrodes to this angle, a suitable potential can be produced to generate a uniform, laminar beam flow through the gap. Normally, a negative bias voltage (15 V) is applied to the grid relative to the cathode to suppress the emission of the electrons. To generate a beam, a positive pulse (36 V) is applied at the grid at 60 Hz, thus allowing the electrons to escape towards the anode. At the exit of the gun, there is an aperture wheel which consists of six apertures, each in different sizes. By selecting an aperture (shown in Table 2-2) on the wheel, the desired beam current can be chosen.

Table 2-2: Cathode aperture sizes used in longitudinal experiments and related parameters. Beam size values courtesy of [44].

Aperture size	Cathode current in the space-charge limited mode (mA)	Cathode current range in the temperature limited mode (mA)†	Beam radius#
0.875	7	2-5	3.19
1.5	23	7-18	4.89
2.85	78	10-50	8.7
3.2*	104	20-80	9.92

*full beam aperture: used for parabolic beam studies and alignment only.

Matched beam radius at $\sigma_0=76^0$

† Though the temperature limited current can be lowered by reducing the cathode temperature, the current range provided in the table corresponds to those values that will remain stable for a sufficient period of time before the cathode cools down.

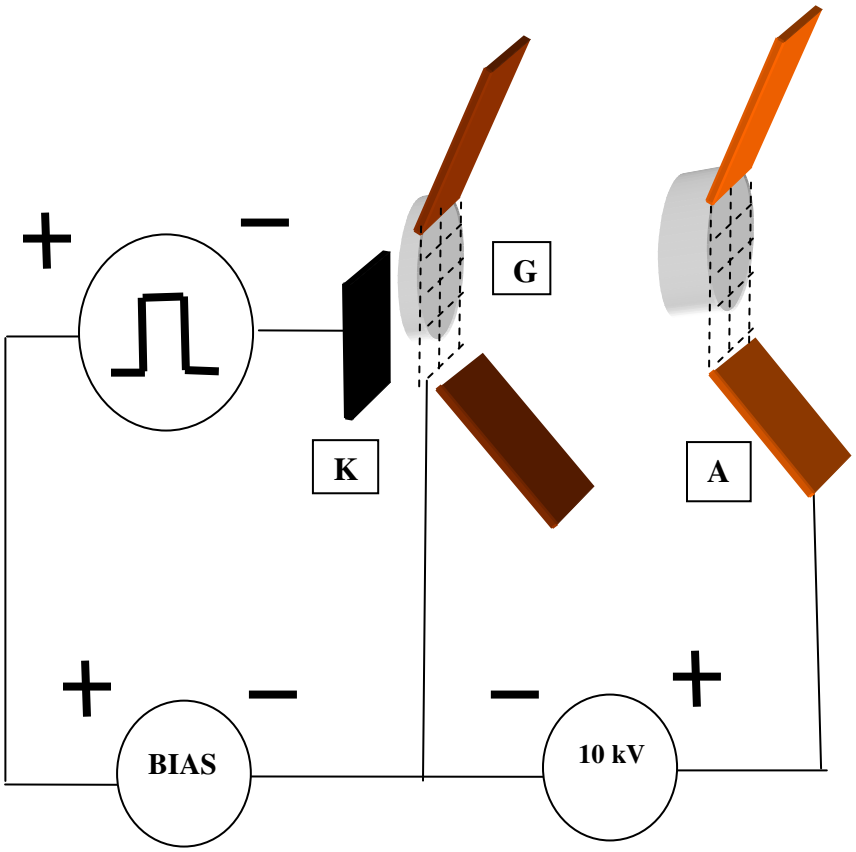

Figure 2.2: Schematic of the UMER gun electronics showing the Cathode (K), Grid (G) and Anode (A). The Grid is biased and an accelerating voltage of 10kV is applied in the gap. Distances not to scale.

Table 2-3: The table showing the important parameters of the UMER gun

Type	Triode, gridded
Geometry	Pierce
Cathode type	Barium dispenser
Cathode	Eimac Y-646B
Cathode radius	4 mm
Cathode grid voltage	Variable from 0 to 50 V
Accelerating voltage	10 kV
Cathode Temperature (normal)	1100^0 C
Space-charge limited mode	> 1000^0 C
Temperature-limited mode	650-850^0 C
Heater voltage (V)	4.0 – 7.5

Instead of holding the cathode current constant and changing the grid as done in a typical triode, UMER pulses the cathode while keeping the grid at a fixed voltage. The anode is gridded to provide uniform potential across the extracted beam. A schematic of the UMER gun is shown in Figure 2.2 .

Various transverse effects have been observed by changing the grid bias. A detailed description of the gun is given in [23].The Table 2-3 lists the important gun parameters of interest.

The UMER gun can be operated in two different modes: temperature-limited and space-charge limited. In the temperature-limited mode, the current across the gap is controlled by the cathode temperature. In this region, anomalous behavior such as a decrease in the beam current when the temperature is increased is observed owing to the triode nature of the gun and the transverse effects. In the space-charge limited emission mode, the gun follows the Child-Langmuir law [45, 46]. The space-charge limited mode is the normal mode of UMER operation. We use photoemission from a laser to enhance the electron density above the surface of the cathode. To be able to use that as a method for perturbing the beam, the gun needs to be operated in the temperature-limited mode. There are two reasons for operating the gun in the temperature-limited mode. By controlling the laser power and changing the cathode temperature, the total beam current- from both the thermionic emission and the photoemission- can be adjusted. This helps us to introduce controlled perturbation for beam experiments. Secondly, by turning the laser on when the gun is in the space charge limited mode, the current density can exceed the Child-Langmuir limit and hence lead to instabilities. So, unless otherwise noted, all the experiments in this dissertation involve operation in the temperature limited mode.

In the UMER gun, we can produce either a positive or a negative perturbation using the laser. We discuss here the physics behind a negative perturbation. By design, when the UMER gun is operated in the space-charge limited mode, the

current density is held uniform across the gap for the full beam current. When the laser is turned on, the current density inside the gap increases for a short time leading to increase in self-field forces. Due to the defocusing effects of space charge, the beam radius at the aperture increases and becomes larger than the aperture size and is cut-off causing a gap in the current flow i.e. a negative perturbation [31]. So, the negative perturbation is due to the transverse effects caused by sudden increase in current density by the photo-emitted electrons. Negative perturbations can also be produced by changing the grid bias and overfocusing the beam [23]. Since the primary focus of this dissertation is longitudinal effects of density perturbations, we will consider only positive perturbation on the beam.

2.3 Laser Setup

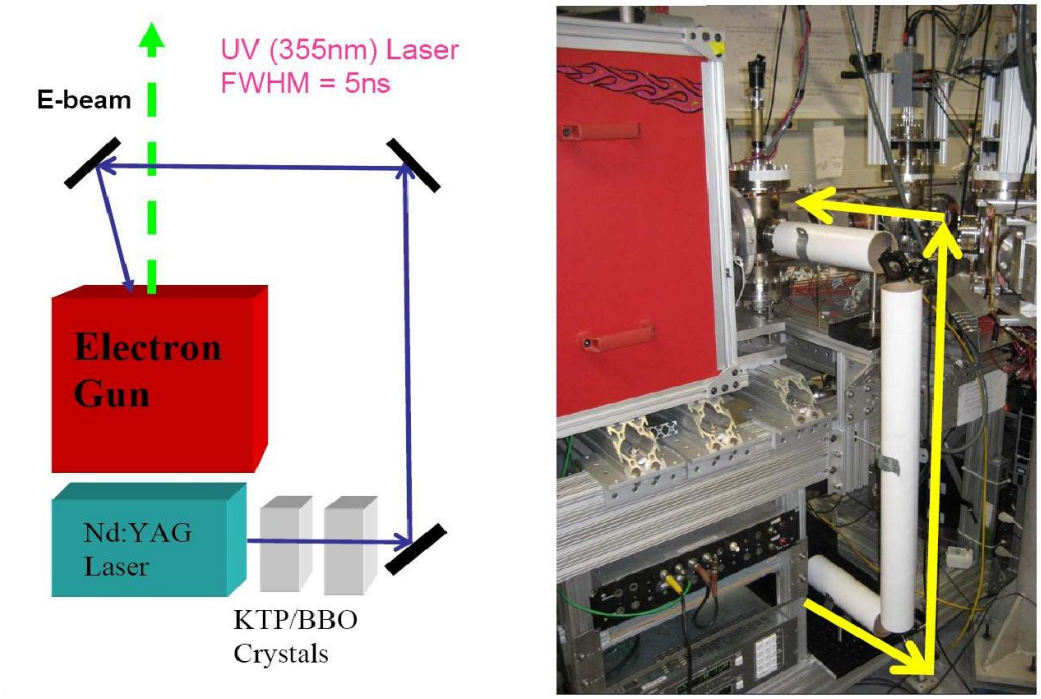

Figure 2.3: Schematic of the laser setup (left) with the experimental setup (right)

Figure 2.3 shows the laser setup. A Minilite [47] Q-switched Nd: YAG laser from Continuum Inc. forms the source of optical power. The wavelength of this laser is 1064 nm. The specified energy at this wavelength is 50 mJ. The full-width half-maximum of the laser (FWHM) is around 5 ns. The pulse repetition frequency can be varied from 1 Hz to 15 Hz. During the experiment, the laser is operated at 15 Hz. A second harmonic of this frequency 532 nm is generated using Potassium Titanium Oxide Phosphate (KTP) crystal. A BBO crystal is used to generate a third harmonic, ultraviolet light at 355 nm. The maximum energy measured at this wavelength was 3 mJ. The UV light is reflected by two dielectric mirrors whose wavelength of reflection is 355 nm. The dielectric mirrors are optional and can be changed to 266nm

by adding additional BBO crystals. The crystals can be either inside the laser or can be external as shown in Figure 2.4. The laser power is controlled by the knob which rotates the polarizer inside the laser providing the needed attenuation.

By allowing the laser light to pass through another multiplying crystal, a fourth harmonic (266 nm) can be produced. After the UV light is reflected by these mirrors, the light passes through the quartz window and is reflected by another mirror installed inside the chamber (IC1) then hits the cathode. The final energy deposited on the cathode is approximately 3 mJ.

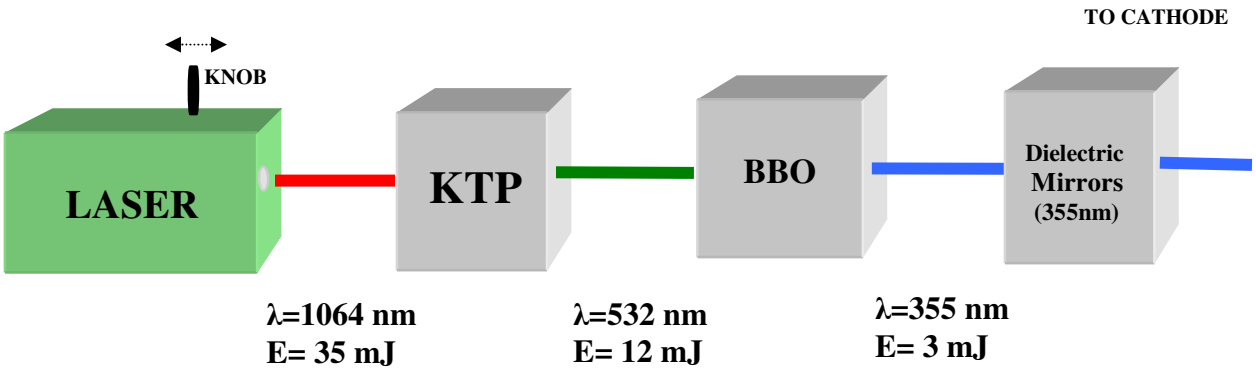

Figure 2.4: A block diagram of the laser setup in UMER along with the multiplying crystals. Measured energy output at each stage is indicated

Table 2-4: Nd:YAG laser parameters

Repetition Frequency (Hz)	1-15
Pulse width (ns)	5
Diameter (mm)	3
Divergence (mrad)	< 3
Jitter (ns)	$\pm$ 0.5
Energy (@1064nm,@355)	35,3
Polarization(@1064nm,@355nm)	Horizontal, Horizontal

The flash lamp of the laser source is triggered at 15 Hz. Around 150 μs after the flash lamp triggers, the Q-switch triggers. The laser pulse is produced 60 ns later than the Q-switch trigger. So, by triggering the electron gun and the Q-switch at the same time, the perturbation is generated at around the middle of the electron beam pulse which is 100 ns long. A schematic optical layout is shown in Figure 2.5 and the timing is shown in Figure 2.6.

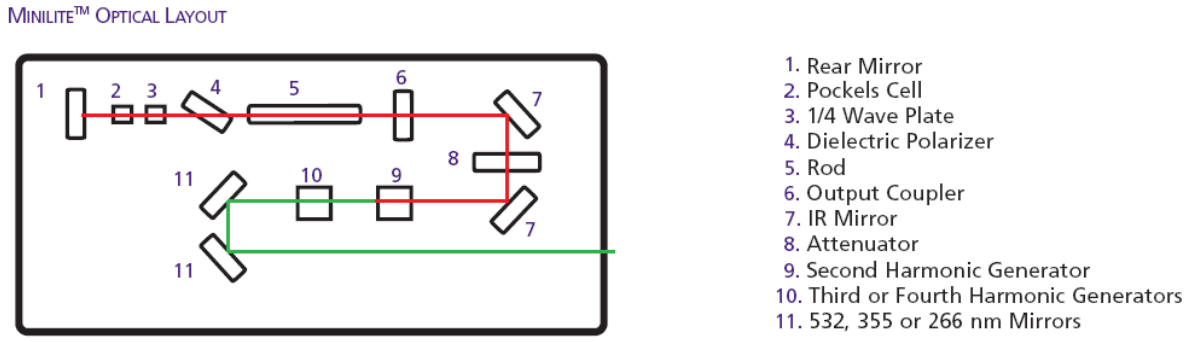

Figure 2.5: Schematic layout of Minilite II laser showing the internal optical setup. The red line is IR while the next harmonics are shown in green.

2.4 Beam Diagnostics:

UMER is equipped with several diagnostics for measuring the beam along the injection line as well as the ring section. We will briefly discuss some of them with a focus on longitudinal dynamics.

2.4.1 Beam Current Diagnostics

The Bergoz fast current transformer, model number FCT-082-20:1, is placed at 64 cm from the anode plane in the injection line. It is basically a transformer with the beam as the primary. The output voltage of the transformer is proportional to the beam current. The measured rise time for a 23 mA rectangular beam is ~2 ns. An oscilloscope trace from the Bergoz current transformer is shown in Figure 2.7

At low- current operation, the beam current at the Bergoz shows some ringing noise. The noise is associated with the injection pulsar and is suppressed appreciably when the injection and recirculation pulsars are turned off.

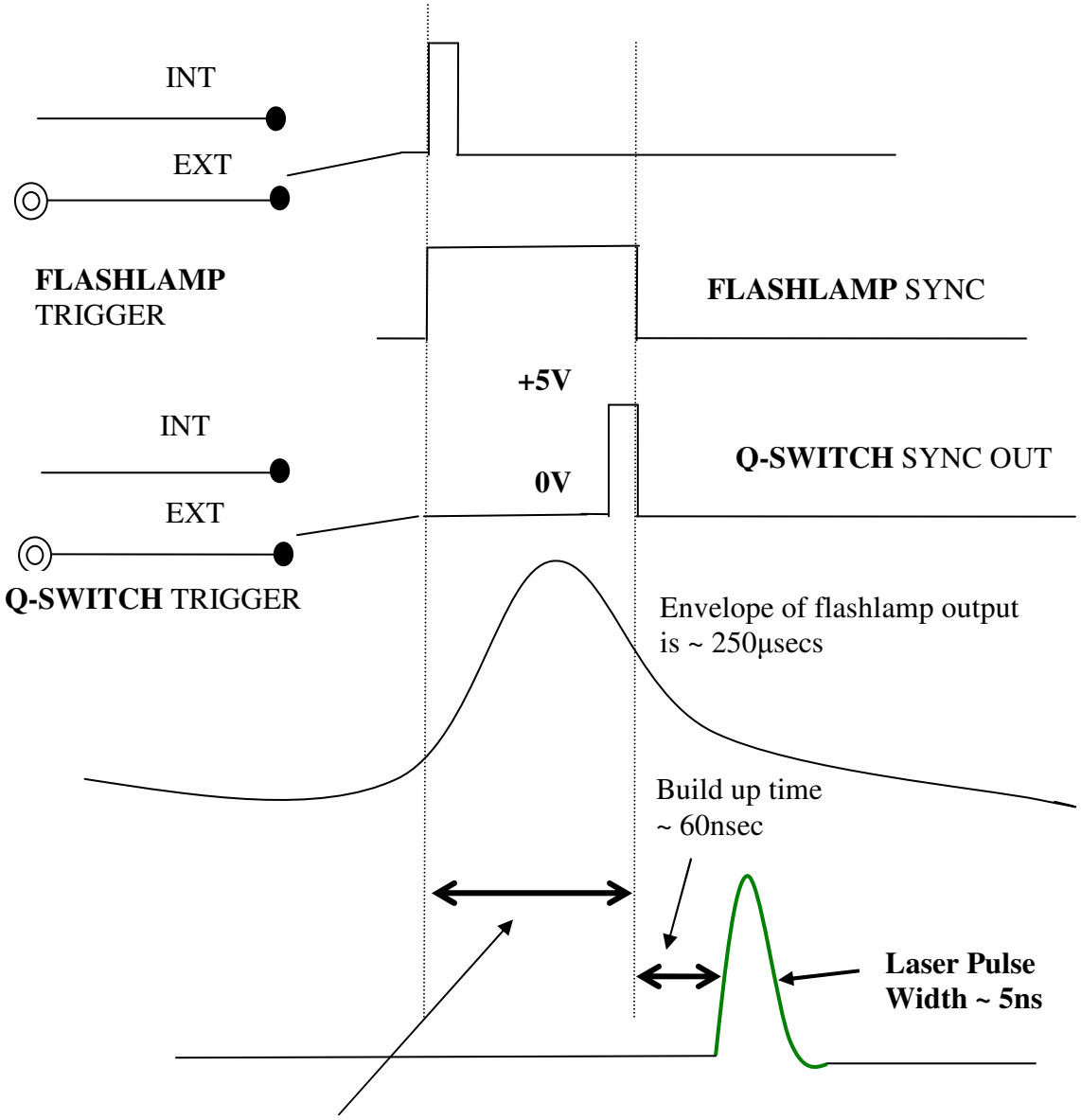

Figure 2.6: Timing pulse sequences of the laser. The flash lamp is triggered externally with the gun trigger. On a 100ns beam, the perturbation is around 60ns from the head of the beam.

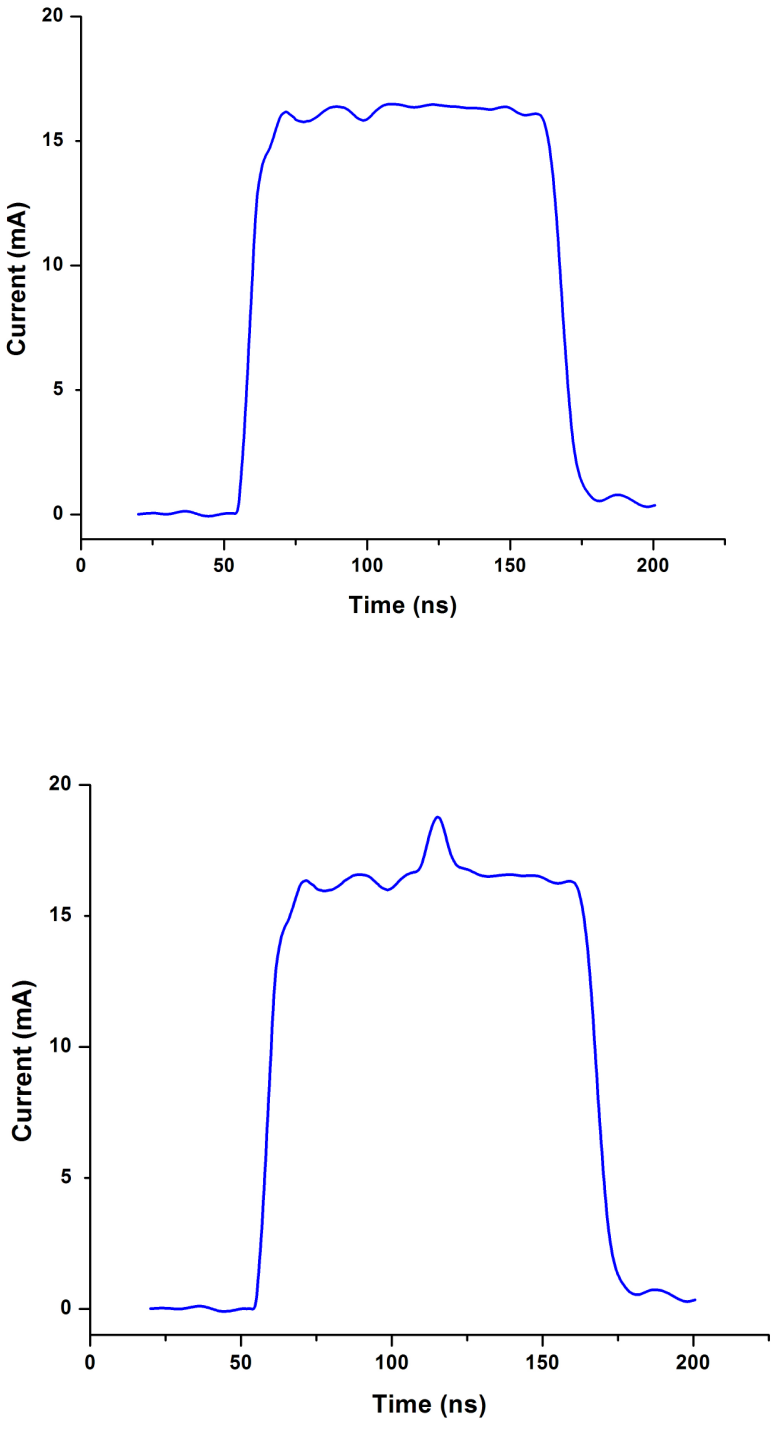

Figure 2.7 :Beam current profile measured using Bergoz current monitor before injection into ring. A 100-ns rectangular beam pulse without the perturbation (Top) and with a 5-ns pure density perturbation is at the center of the main beam pulse (Bottom).

Beam position monitors (BPM) are standard diagnostics used in storage rings for measurement and correction of beam position. They measure beam position by coupling to the electric field of the beam. They consist of four electrodes placed symmetrically around the beam axis. The signal at the individual electrode is proportional to the distance of the beam from the electrode. UMER BPM [48] are designed to achieve good spatial and temporal resolution of the order of 2 ns. Recent work [39, 49] increased the signal-to-noise ratio of the BPM signal and measured its linearity. An experimental BPM trace tracking a UMER beam is shown in Figure 2.8. All the beam centroid measurements in UMER use the BPM signals to track the beam. Beam-based steering solutions obtained from simulation are used to make corrections to the orbit.

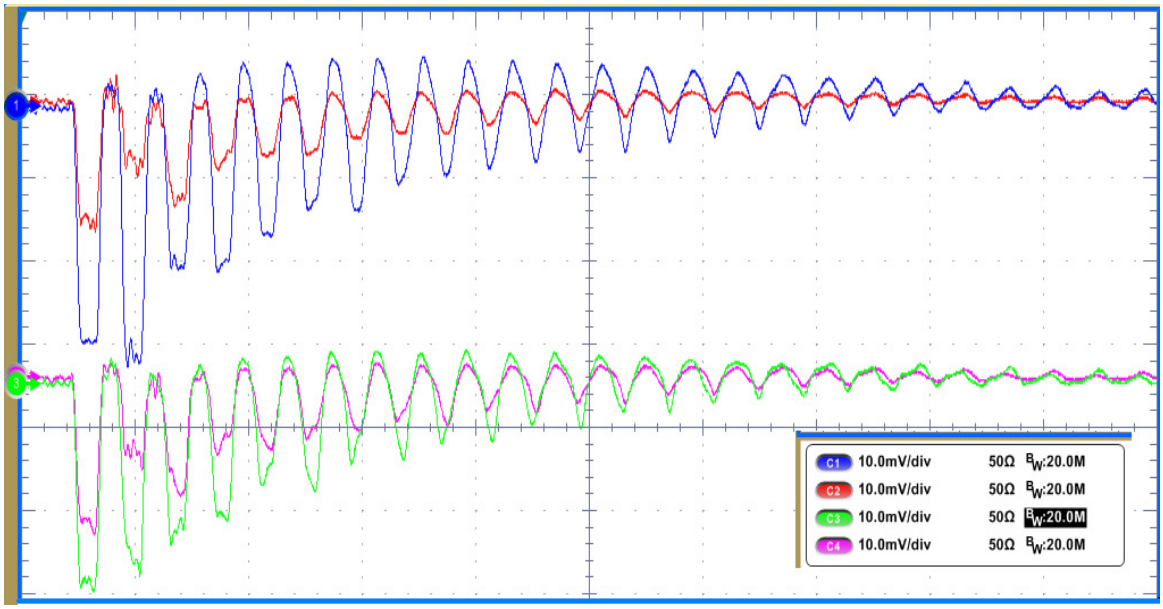

Figure 2.8: The four signals are from the top, bottom, left and right plates of the beam position monitor. The beam current measured was 23mA at 1.84 A quad current settings. As the beam propagates, the beam expands and fills the ring.

2.4.2. Wall Current Monitor

In the closed path around the vacuum chamber, there is no magnetic field. i.e. $\oint B_{external}.dr = 0$; whereas inside the chamber $\oint B_{inside}.dr = I_{beam}$. So there must be an equal and opposite current, called the image current, flowing on the beam pipe. A wall current monitor measures this image current. In order to measure the image current, a ceramic (glass in UMER) gap is created in the beam pipe and a resistor is added parallel to the gap. By measuring the voltage drop across the resistor, the beam profile is captured. In UMER there is an added complexity. The image current actually flows through a ground loop created by the plates that hold the FODO sections. In order to choke off the image current from flowing through the ground loop created by the plates, a high ferrite material is added and the image current is forced to flow through the resistor. The details of the wall current monitor and the equivalent circuit model are given in [30]. A schematic of the wall current monitor is shown in Figure 2.9 . The wall current monitor is AC coupled and hence when the beam expands and fills the ring (especially near the ends), the DC component registers as an apparent beam loss.

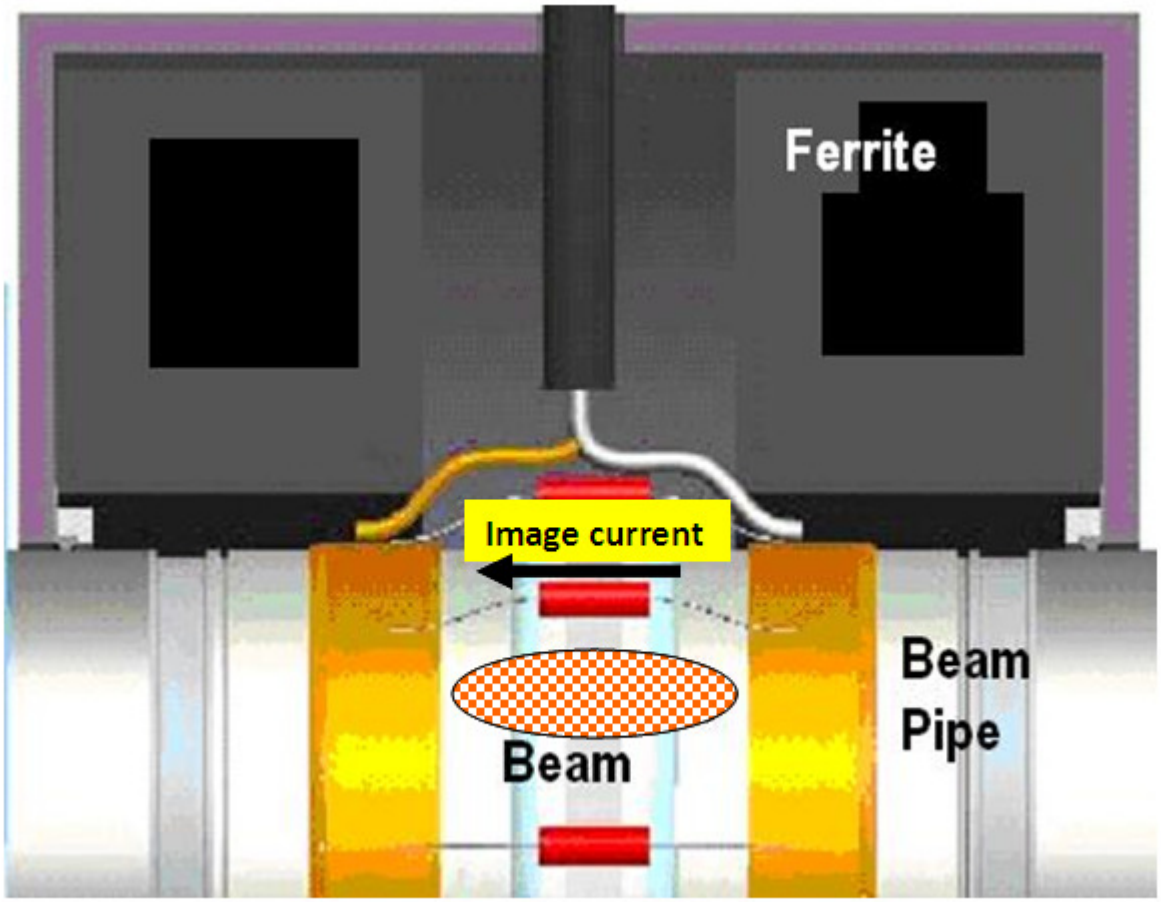

Figure 2.9:The wall current monitor principle: The image current induced in the beam pipe is forced to flow through the resistors using the ferrite core and the voltage across the resistors measured is proportional to the beam current. Courtesy [30]

2.4.3 Fast Imaging Diagnostics

Conventional fluorescent screens such as P-43 have a long response time on the order of microseconds. Therefore, they are not capable of resolving nanosecond time structures inside the beam. Lexel Imaging Systems, Inc [50] manufactures fast phosphor screens that have a time response around 3 ns. The screen consists of ZnO:Ga formulation on a quartz plate. When an electron beam hits the screen, it emits a bluish light in the near UV (around 390 nm), visible to the eye. A thin layer

(1μm) of aluminum is coated on the screen to conduct the electrons away from the screen and prevent charge buildup. In UMER, the fast phosphor screens are installed at IC1 (31.1 cm from the aperture), RC 8 and at RC 15, while the conventional P-43 screens are installed at all the other locations of the beam position monitors. The light from the screen is reflected by a mirror, placed 45° the beam line, and seen through the viewport.

The light from the fast phosphor screen is captured by an ICCD (Intensified charge coupled device) PIMAX-2 camera manufactured by Princeton Instruments[51]. The bandwidth of the camera is between UV and Near-IR making it suitable for the experiments. The high-speed camera has an internal pulse generator for adjusting the gate/delay time and can do time-gated imaging at nanoseconds (3-ns). A wide dynamic range (16-bit) makes the camera sensitive to halos and internal structures in the beam. A general setup of the image acquisition system used in UMER is shown in Figure 2.10.

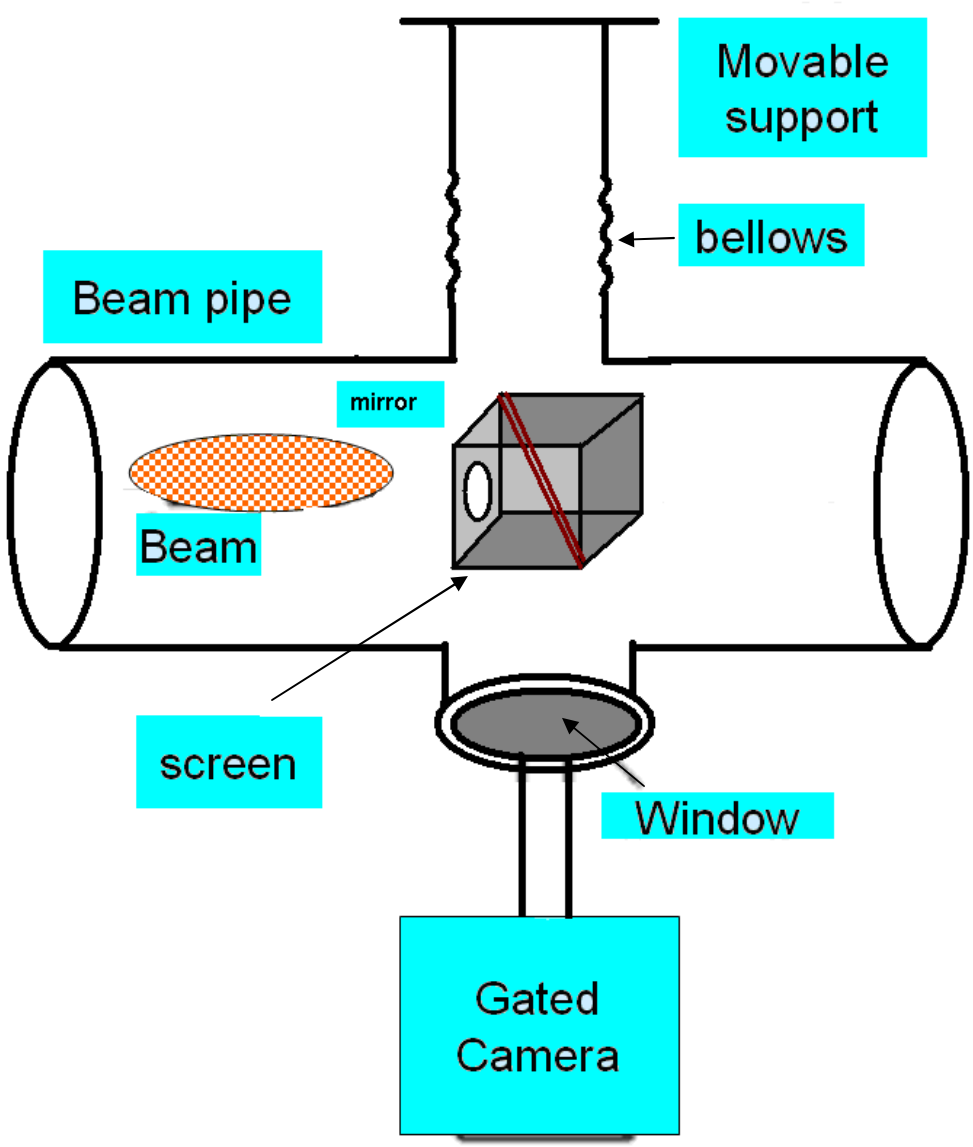

Figure 2.10: Fast imaging diagnostics set up in UMER. The beam hits the fast phosphor screen (ZnO:Ga) and the light emitted is captured by the camera (ICCD PIMAX2) for further processing via the quartz window.

2.5 Summary:

We have briefly discussed the University of Maryland Electron Ring and the beam current diagnostics. In this thesis, the primary diagnostic for all the experiment will be the wall current monitor and the fast current transformer (Bergoz). The fast imaging diagnostics will be used to study the transverse effect of

perturbation in the following chapter. In addition to all these diagnostics, we are currently testing the energy analyzer on UMER and have not used it in this work. The measurements from the energy analyzer will complement the work done in this thesis.

Chapter 3. Experimental investigation of a single perturbation on a space-charge dominated beam

Laboratory beams have either density or velocity modulations. These modulations are due to cathode non-uniformities, laser fluctuations and various other sources. In order to study the effect of such modulations, we begin by introducing a single, localized and controlled density perturbation on a beam using a laser.

In this chapter, we present various experiments with a single perturbation on the beam. We know that a perturbation emits a pair of space charge waves that travel at the sound speed. We begin by measuring the sound speed as a function of the beam current in Section 3.1. In Section 3.2, we measure the sound speed as a function of the perturbation strength by keeping the beam current constant. In Sec 3.3, we compare the experimental results with theory and WARP simulation. In Section 3.4, we show how space charge waves can be used as a beam diagnostics. Finally, in section 3.5, we present time-resolved measurements of the perturbation and conclude.

3.1 Wave speed as a function of beam current

In order to measure the variation of the wave speed as a function of beam current, the following experiment was performed in UMER. We use the gun aperture (2.85mm) and then adjust the cathode temperature to generate a 100ns rectangular beam pulse with 16mA peak beam current. An UV laser (355nm) is switched on to generate a 5ns perturbation on top of the main beam current. The current settings on the focusing and steering magnets were set for a phase-advance of $\sigma_0 = 61^0$. The

quadrupoles current was set at 1.83 A which corresponds to a peak gradient of 6.63 G/cm. The beam pulse is measured at the Bergoz coil which is shown in the

Figure 2.7.

After injecting the beam into the ring, the beam current is measured using the wall current monitor at RC10. Figure 3.1 shows the turn-by-turn beam current profile from the wall current monitor. The perturbation splits into a fast and a slow wave with the waves travelling toward the head and the tail of the beam respectively with sound speed. Since there is no longitudinal focusing applied to confine the beam longitudinally, the beam itself is expanding and the edges of the beam move inwards. By applying ear-fields using the induction modules, longitudinal focusing and acceleration can be provided for the UMER beam [30].

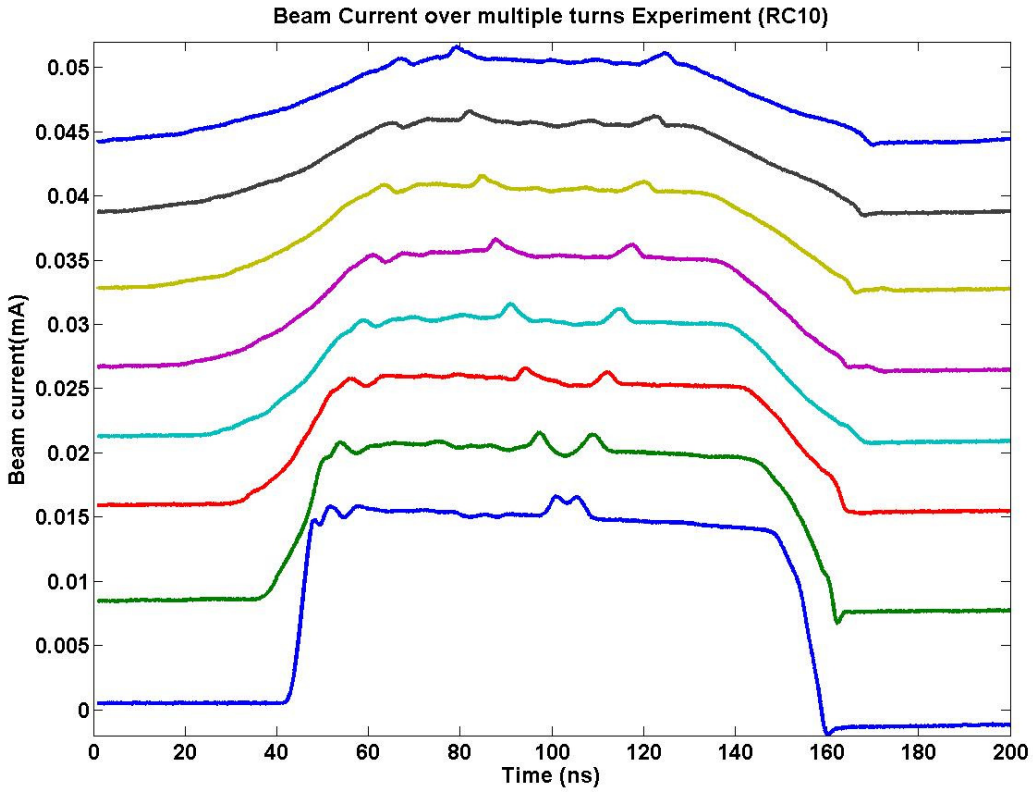

Figure 3.1: Turn-by-Turn plot of the beam current obtained from wall current monitor. Turn 1 is on the bottom with subsequent turns plotted on top of each other. Injected beam current was 16 mA. For clarity, every turn of beam current is shifted with a constant value of 5mA. The tune of the machine was set at $\upsilon_0 = 6.1$.

The wall current monitor is AC-coupled and hence measures only time-varying component of the beam current. When the beam ends meet, the beam becomes quasi-DC and so the AC component is lost and appears as the beam loss at the wall current monitor. Hence, the actual beam loss in the ring is smaller than the measured beam loss.

After recording the beam profile from the wall current monitor, the main beam current is changed by changing the temperature of the cathode, keeping the

relative perturbation strength (η=0.2) constant. In this experiment, the beam currents used were 8mA, 16mA and 24mA. A 3-D waterfall plot is shown in Figure 3.2.

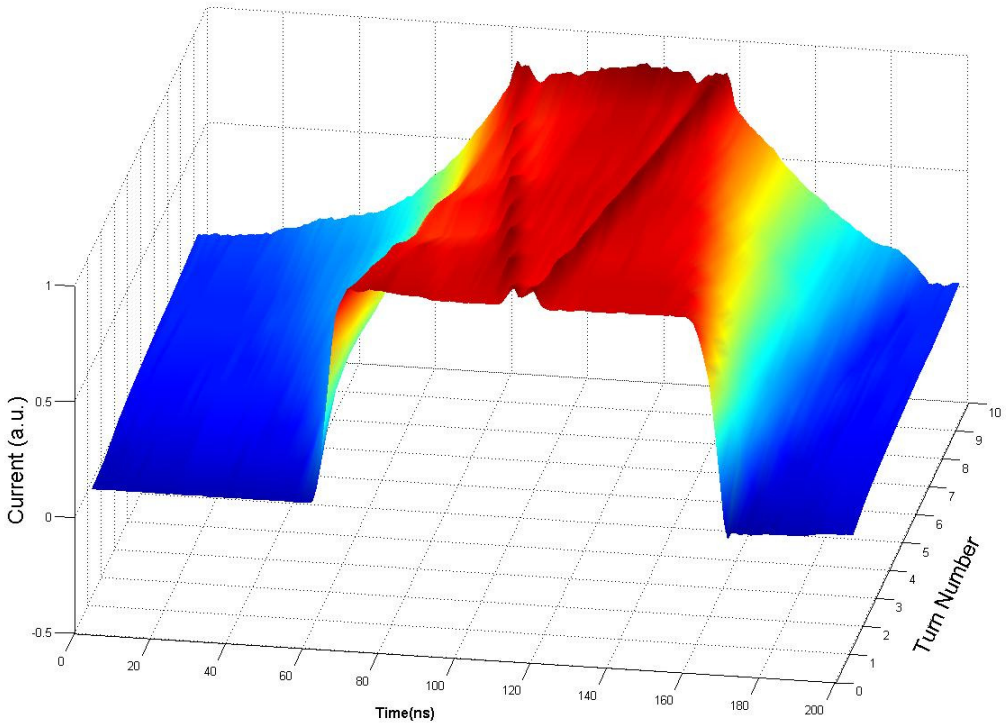

Figure 3.2: 3-D plot of beam current evolution with single density perturbation. The plot is generated by interpolating the turn by turn data obtained using the wall current monitor. The injected beam current is 16 mA at 10keV.

We use the following method to calculate the sound speed from the experimental data. Let us assume the fast and the slow waves travel a distance of Δz in a given time Δt. The velocity of the fast and the slow waves are $\upsilon_0 + C_s$ and $\upsilon_0 - C_s$ respectively in the lab frame. Let us take the fast-wave as a reference for calculation

purposes. The fast and the slow waves move away from each other at twice the sound speed. So,

$$
\begin{aligned}
2C_s &= \frac{Distance}{Time} = \frac{(\upsilon_0 + C_s)\Delta t}{\Delta z/(\upsilon_0 - C_s)} \\
\Rightarrow C_s &= 0.5\frac{\Delta t}{\Delta z}\left(\upsilon_0{}^2 - C_s{}^2\right) \\
\therefore C_s &\simeq 0.5\frac{\Delta t}{\Delta z}\beta^2 c^2 \qquad \text{since } \upsilon_0{}^2 \gg C_s{}^2
\end{aligned}
\tag{3.21}
$$

β is the ratio of the beam velocity to the velocity of light $\beta = \upsilon_0 / c$. Δz is equal to 7.67 m+ (n-1)11.52 m where n is the number of turn, with n=0,1,2..

The center- difference method to calculate Cs:

The eqn (3.21) has few limitations. It assumes that the beam current is not changing between the measurements. This is a good assumption for a short distance beam transport like Long Solenoid Experiment [52] or within the first turn of UMER [22]. But, in our case, we have many turns and the beam current is changing between the turns. So, we have to include the effect of varying beam current into the formula for Cs.

Let us begin by plotting Δt, the time separation between the peaks of the fast and the slow waves against the distance. We then plot the beam current as a function of distance to show how the current varies with distance. This is shown in Figure

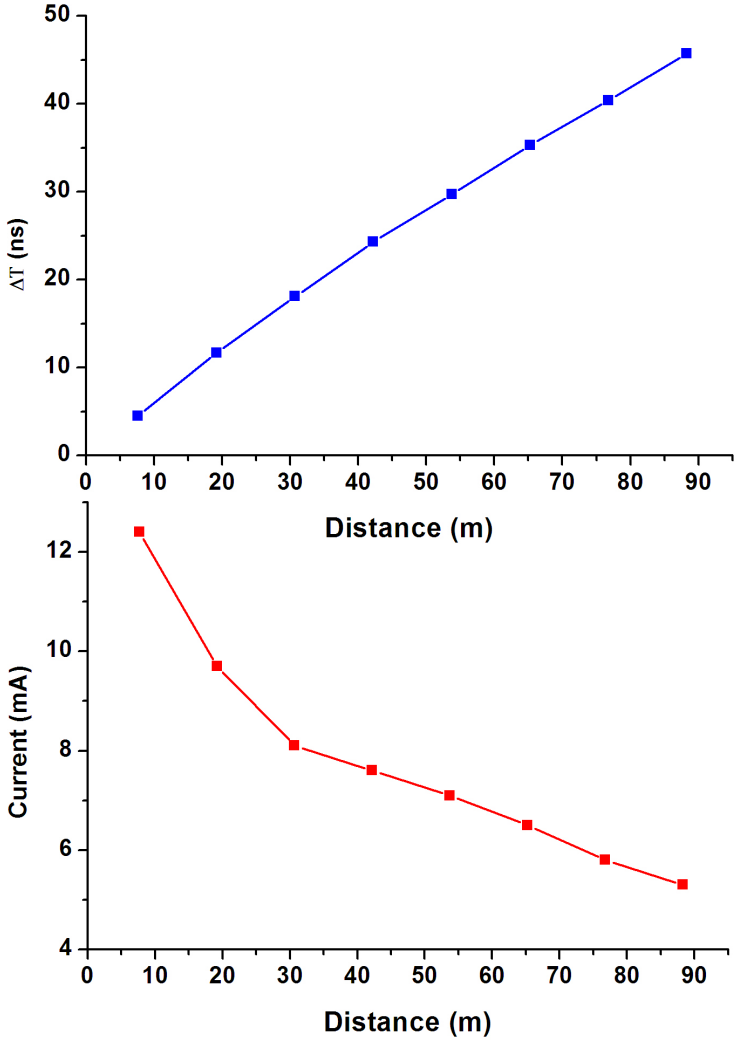

Figure 3.3: The top graph plots the time separation of space-charge waves with the distance. The bottom graph is the beam current as a function of distance. The beam current is changing as a function of distance which affects the linearity of the wave speed. Hence, we have to take into account the varying beam current in calculating the value of sound speed from the measurements.

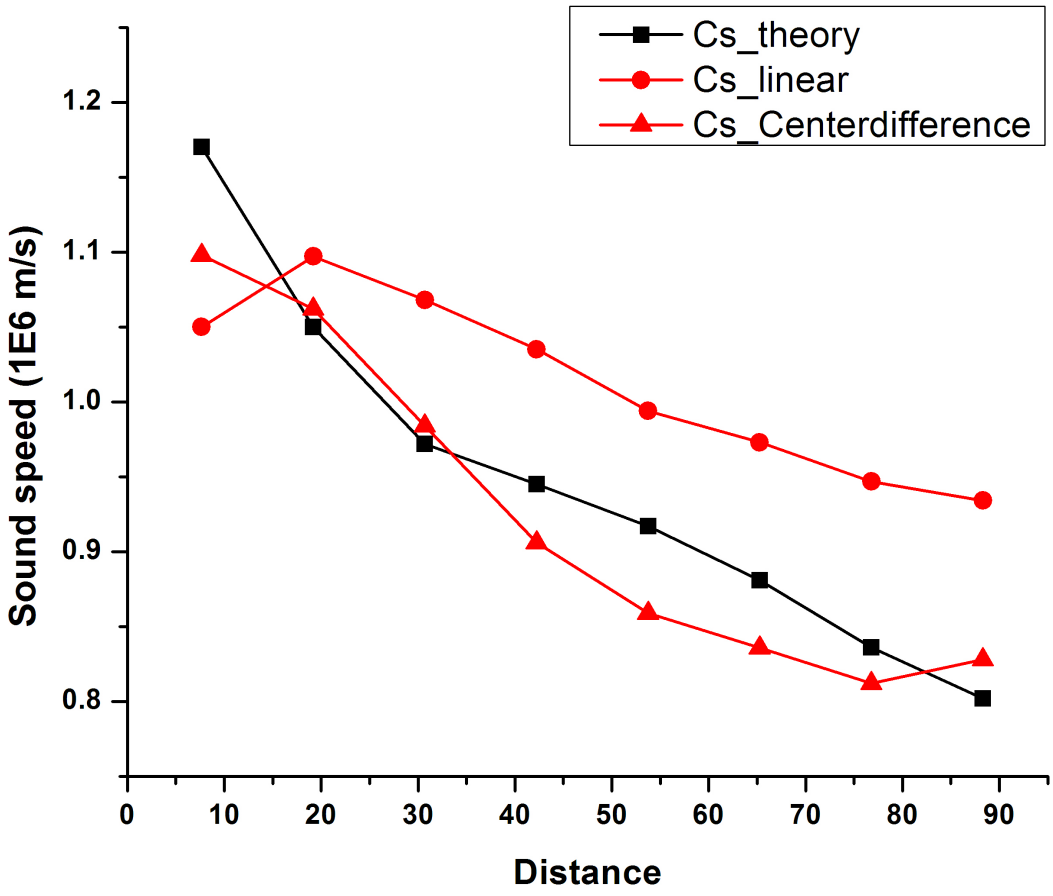

Figure 3.4 : The graph shows two ways of measuring the value of Cs from the experimental data. The black curve is the sound speed calculated from the theoretical formula. The two red curves correspond to the calculation of the sound speed from experimental values using the linear method eqn (3.21) and the center-difference method eqn(3.22) . As the distance increases, the center-difference method is closer to the theory as expected.

Since our quantity of interest is $\frac{d(\Delta t)}{d(\Delta z)}$,we use the center-difference method, a form of finite difference method, to calculate Cs. Though an ideal method would fit a function and calculate slope, we use difference equations as follows: Let us assume we want to calculate the sound speed at turn 5 say C_{s5}. To do this, we measure the time separation of the space charge waves in turn 5 and record it as Δt_5. Then C_{s5} is calculated using the formula: $Cs_5 = \frac{\Delta t_6 - \Delta t_4}{2 \times 11.52\text{m}}$. For calculating Cs for the first and

the last turn we use $Cs_m = 0.5\left(\frac{\Delta t_{m+1}}{11.52\text{m}}\right)\beta^2 c^2$, $Cs_1 = 0.5\left(\frac{\Delta t_2}{11.52\text{m} + 7.67\text{m}}\right)\beta^2 c^2$, where m is the last turn number. This reduces the uncertainty due to the variation in beam current. So, in general we can write, Cs from the center-difference method as

$$Cs_m = 0.5\left(\frac{\Delta t_{m+1} - \Delta t_{m-1}}{2\times 11.52\text{m}}\right)\beta^2 c^2 \tag{3.22}$$

In order to calculate the value of sound speed from theory, the following method is used. For every turn of data, the beam current I is measured. Now, we need to know the beam radius every turn. Assuming smooth approximation in a periodic focusing lattice, the beam size a can be calculated from $a = R(u + \sqrt{1+u^2})^{1/2}$ [31] , where $R = \sqrt{\frac{\varepsilon S}{\sigma_0}}$ is the matched beam radius in a smooth focusing lattice with emittance ε = 30 microns and S=32cm is the lattice periodicity in UMER and σ_0 is the zero current phase advance and $u = \frac{KS}{2\varepsilon\sigma_0}$ where $K = \frac{2I}{I_0(\beta\gamma)^3}$ is the beam perveance and I_0 = 17 kA for electrons. For this experiment, as mentioned before σ_0 is set at 61^0.

Table 3-1: Table showing the values of the time separation ΔT of the space charge waves with distance and the corresponding values of Cs calculated using linear and center difference techniques.

Distance (m)	ΔT (ns)	Cs_Theory (10^6m/s)	Cs_linear_technique (10^6m/s)	Cs_center_difference (10^6m/s)
7.67	45	1.17	1.05	1.09
19.19	117	1.05	1.09	1.06
30.71	181	0.97	1.06	0.98
42.23	243	0.94	1.03	0.90
53.75	297	0.91	0.99	0.86
65.27	353	0.88	0.97	0.83
76.79	404	0.83	0.94	0.81
88.31	457	0.80	0.93	0.82

The calculated values of the sound speed versus the values predicted by theory are shown in Figure 3.5. As predicted by the 1-D theory, the wave speed increases as the beam current increases. This is because as the beam current increases, the line-charge density increases, leading to the increase of longitudinal space charge field, which drives the waves faster. This is similar to sound waves, which travel faster in denser media.

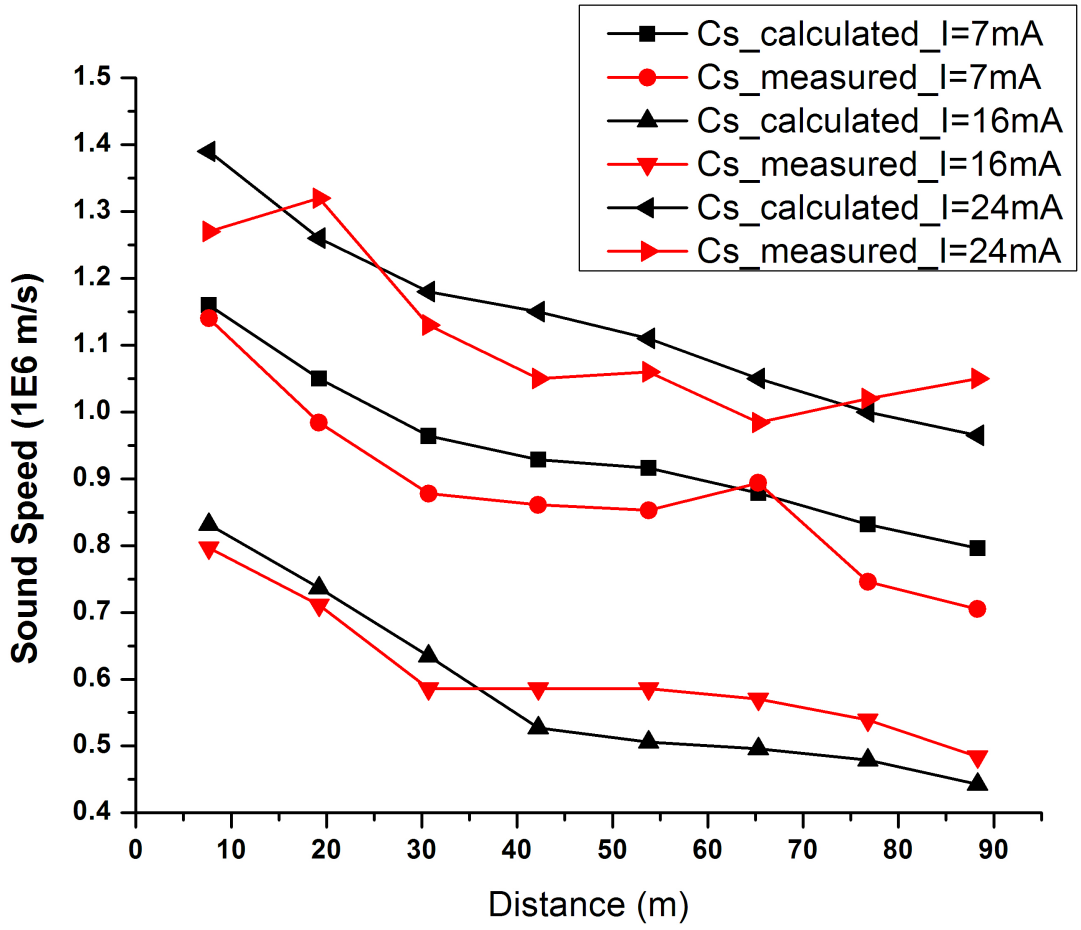

Figure 3.5: Graph comparing the sound speeds for different main beam current for the same strength of the initial density modulation along with values predicted by theory. The higher the main beam current, the faster the waves depart from each other. A 5% error bar in the data is not shown in the graph for clarity.

3.2 Wave speed as a function of perturbation strength

Further experiments were carried out to study the effect of the perturbation strength (η) on the wave speed of the space-charge waves. In these experiments, we used three beams: 15.5 mA beam with 1mA perturbation, 16.4 mA beam with 2 mA perturbation and 17.4 mA beam with 4 mA perturbation. The perturbation strength was 6%, 10% and 20% of the main beam current for each of these cases. The sound

speed is calculated from the theory and the experimental data as described in the previous section. The results are plotted in Figure 3.6 .

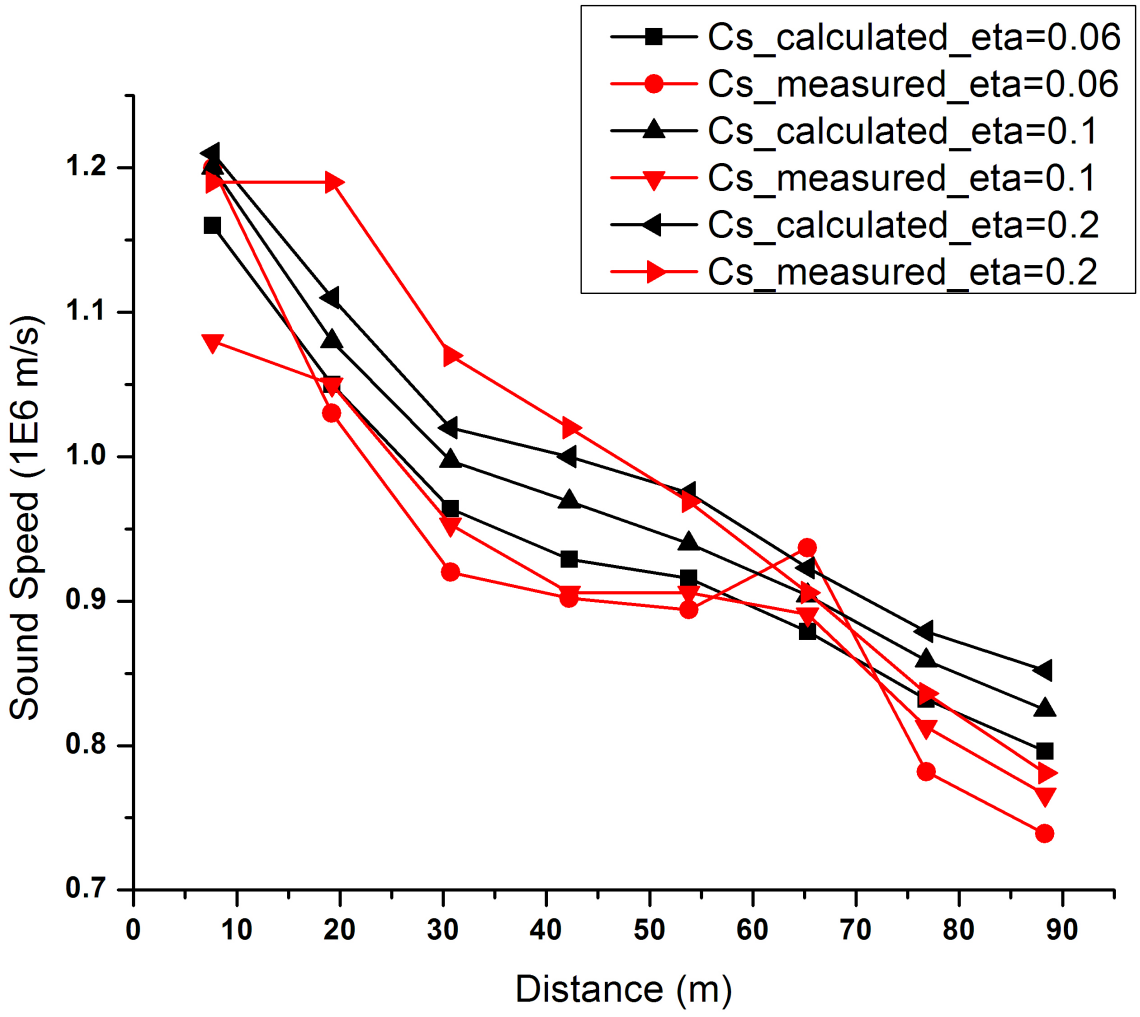

Figure 3.6: Sound speed as a function of distance for different strengths of the initial density modulation. The higher the strength of the perturbation, faster the wave moves.

We see that, as the perturbation strength increases, the wave speed increases indicating a non-linear trend. One of the important properties of a non-linear wave is that the speed of the wave will depend on its amplitude. Such nonlinearity can lead to wave breaking. Moreover, there is a discrepancy between the theory and the experiment for the value of the sound speed in the case of η=0.2. This is because the

1-D cold-fluid model assumed a small initial perturbation to linearize the variables ($\lambda_1 << \lambda_0$) while η is not negligible in this case. In conclusion, these experiments illustrate the range of perturbation strengths for which 1-D cold fluid theory holds true.

3.3 Simulation using WARP

In order to simulate the evolution of perturbations in the beam, we use the particle-in- cell code (PIC) WARP. WARP is a self-consistent code, meaning that once the density and velocity distribution of the particles is given, WARP correctly includes the effect of the evolving self-fields. It does so by creating grids and by calculating self-fields at every grid point for the given distribution and the given boundary conditions. The calculated self-field and the external fields are then applied to move the particles to a new position resulting in a new distribution, whose self-field is calculated again, and the procedure is repeated until the end of the simulation. The initial particle density distribution and velocity distribution as well as other boundary conditions (such as the pipe radius, pulse length) must be specified in WARP.

In our case, since the laser introduces a pure density modulation, we have no velocity modulation at the cathode. Therefore, we import the Bergoz current transformer signal directly into WARP for the initial current distribution. We assume that the velocity modulation is still zero at the Bergoz coil. We also initialize the code with the values of matched beam radius, current, energy and emittance. We made the following approximations. We assumed a smooth uniform field (solenoid field) to represent the UMER FODO lattice. Since we use a long solenoid field for focusing,

we have an external field which is symmetric in the x and y-axis. Hence we used WARP-RZ, a version of WARP-3D, for all our simulations.

The initial transverse distribution used is a semi-Gaussian (uniform in density and Gaussian in velocity). Two important quantities of interest in our simulation were the number of particles and the longitudinal thermal spread. When we attempted to increase the accuracy of the simulation by increasing the number of particles, we ran into numerical instabilities. We avoided instabilities by increasing the longitudinal thermal speed. The values we used are: the number of particles = 1 million and the thermal speed was 1.5×10^5 m/s, which corresponds to $\Delta p/p = 0.25\%$. The transverse grid size was 64x1 cells (R-Z) and the z-grid was 256x256. Before running every simulation, the appropriate dE/dr was calculated for matching the beam with the assumed solenoidal field. All simulations are done in the beam frame without any longitudinal focusing.

For simulating the experiment discussed in the previous section, we loaded the 16 mA beam current with a density perturbation strength of $\eta = 0.2$. The beam current profile obtained from the current monitor in the injection line is used as the initial longitudinal distribution. Figure 3.7 shows the turn by turn plot of the beam current profile obtained from WARP. The space charge wave velocity is calculated from the simulation for every turn and is in good agreement with the theory. But the experimental values of wave speed differ from the values obtained from WARP. This is because we assume there is no beam loss in the WARP simulation. In other

words, WARP agrees with the predicted theory. But both differ from the experimental results possibly due to exclusion of beam loss from the simulation and the theory.

So we deliberately introduced beam loss into the simulation and compared it with the experiment. We used the WARP variable (top.pgroup.sw) to change the particle weights every turn. The variable effectively changes the number of real particles per macro particle. We changed the particle weight such that the beam current in the simulation equals the beam current in the experiment after every turn. Figure 3.8 shows the experimentally measured wave speed values and compares them with the prediction for theory and simulation, with and without beam loss. This improves the agreement between WARP and the experiment for many turns as shown in Figure 3.9. In essence, we have predicted, measured and numerically verified the wave speed with a good accuracy. The discrepancy in the zero-th turn is because the waves have not separated yet and hence those points should be ignored. We can still improve the accuracy by doing the following: the simulation can be done in the lab frame rather than the beam frame. This will compensate for the slight asymmetry between the fast wave and the slow wave in time separation from the beam centre. Also, we have ignored the energy profile at the Bergoz and have taken it to be zero. This could be measured and the velocity profile loaded into the simulation to improve the accuracy.

We have also neglected transverse effects of space charge. The transverse effect can play an important role in space-charge dominated beams. We discuss in the next section how transverse effects of space charge waves can be used to measure beam size.

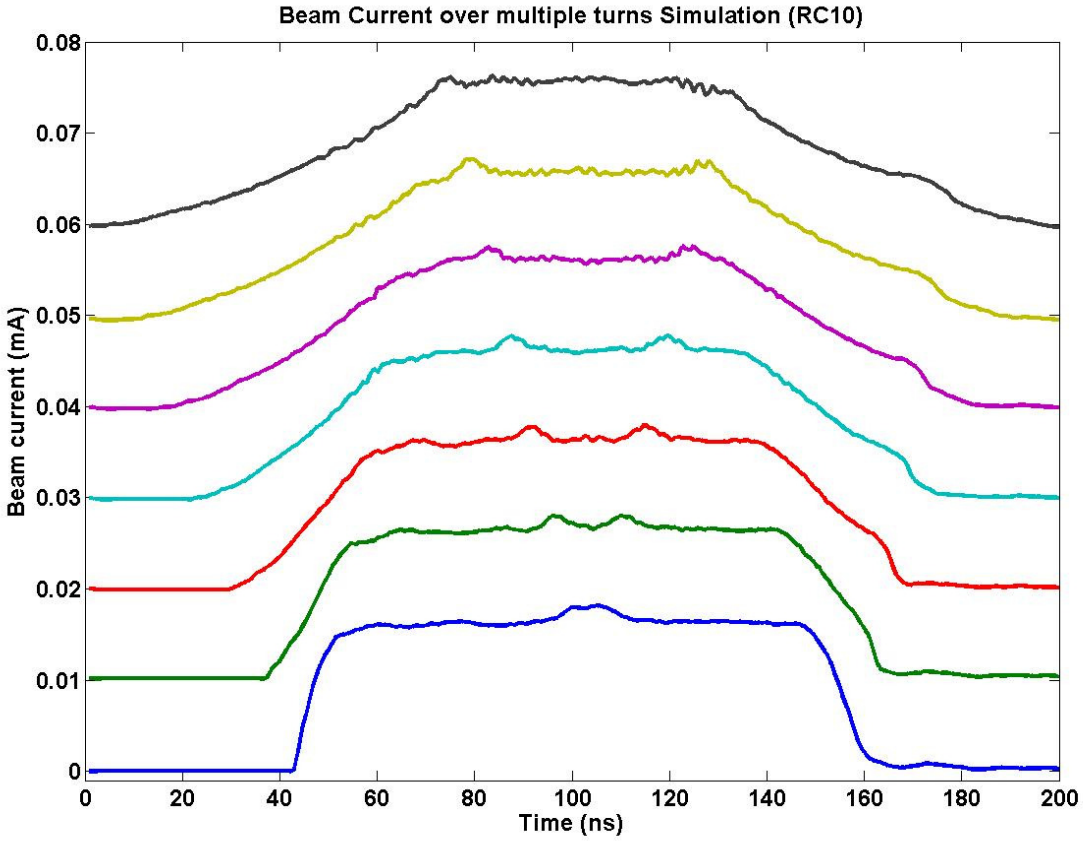

Figure 3.7 : Turn by turn plot of beam current obtained from PIC simulation using WARP. Since there is no beam loss assumed in the simulation, the waves reach the ends of the beam faster than in the experiment. The injected beam current is 16mA. For the sake of clarity, the beam profile from every turn is shifted vertically.

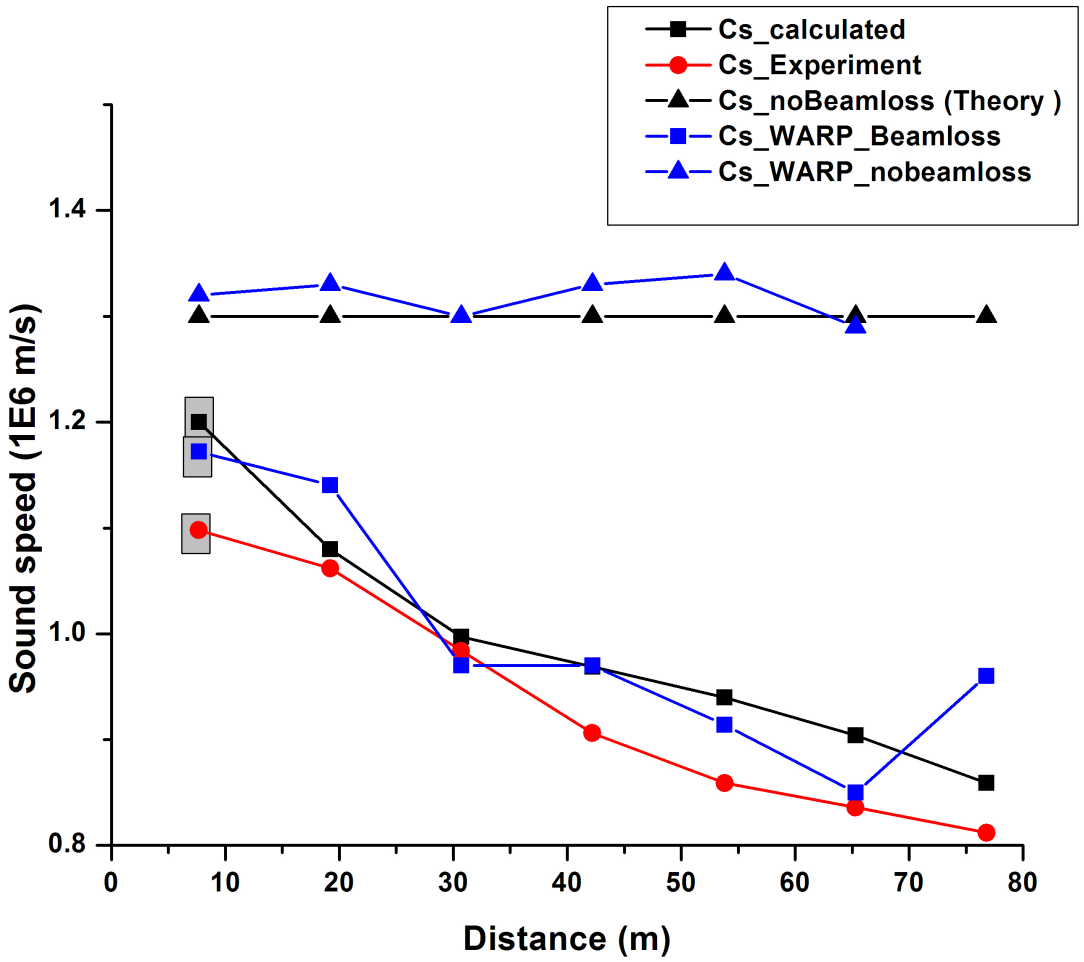

Figure 3.8 : Sound speeds measured from the experiment, and theory along with those obtained from simulation with and without beam loss. Theory and WARP agrees with measured data when beam loss is included in the calculation. For the zero-th turn, the measured and the calculated values of the sound speed show a large discrepancy. This is because the fast and the slow waves have not yet separated at this distance. These points are indicated by gray boxes. The black line with the black triangles uses the formula for Cs for a given beam current and hence does not change with the turn. But, in the experiment, the current changes and taking this account the Cs is calculated and this is the black line with the black boxes. The red line is the experimentally measured value of Cs. The blue lines correspond to the WARP simulation. The blue line with the triangle ignores beam loss while the blue line with the boxes includes beam loss.

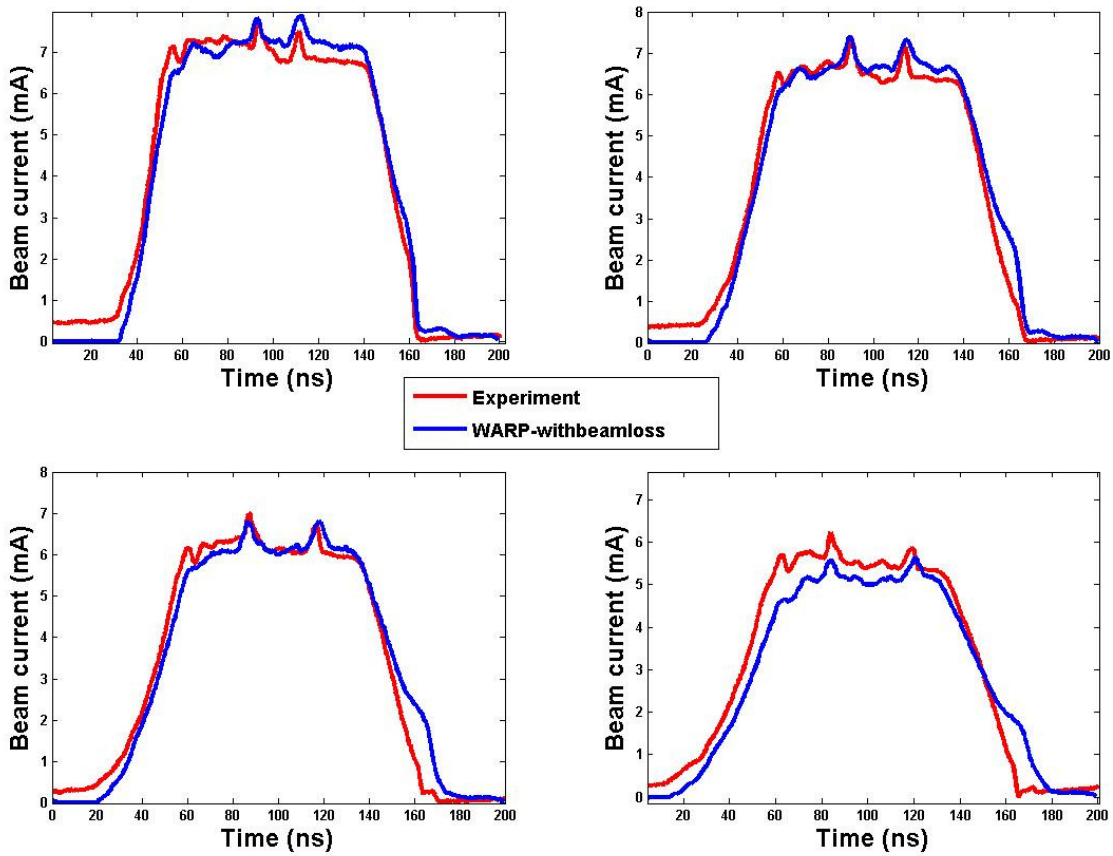

Figure 3.9: WARP simulation including beam loss is compared with the experimental data. The beam current is 16mA with a 20% perturbation. The time-evolution of the perturbation obtained from WARP is overlaid on the experimental measurement showing both the fast and the slow waves evolving at almost the same speed as seen in the experiment. The turns shown in this plot are turn 3 (Top: left), turn 4 (Top: right), turn 5 (Bottom: left) and turn 6 (Bottom: right).

3.8 Beam End Erosion

As seen from the experimental data, the beam ends erode inward as the beam propagates. There is no longitudinal focusing applied to the beam causing the beam to expand and fill the ring. At the edge, the charge density varies sharply leading to a large electric field. Appropriate external fields, called "ear-fields", have to be applied to focus the beam.

Currently, they are applied at RC4 through the induction module. For the low-current beam (0.55 mA), this increases the number of turns to 200 turns. Space-

charge wave experiments have shown that the waves reflect off the beam ends[17]. With the induction module, UMER is capable of repeating such experiment over a longer distance and track the propagation of the waves after reflection from beam ends. In theory, the fast wave after reflection from the beam ends will become a slow wave and vice-versa. Experiments conducted in UMER, without the longitudinal focusing, show that the waves walk off the edge of the beam without any reflection.

3.4 Space-charge waves as beam diagnostics for measuring transverse beam size

In order to measure the beam size over multiple turns, we need a non-intercepting beam diagnostic. As an alternative to fluorescent gas monitors or diagnosis through an extraction line, space-charge waves can be used to measure transverse beam size turn-by-turn. The principles behind the technique are Equation (1.17) and (1.12). Combining those two equations, we get:

$$\ln\frac{b}{a} = \frac{2\pi\varepsilon_0\gamma_0^5 c_s^2 m\upsilon_0}{qI} \tag{3.23}$$

After measuring C_s and I for every turn, Equation (3.23) can be used to calculate the values of beam radius. As the flat-top erodes, the beam current decreases leading to a decrease in beam size. Other sources of particle loss like beam scraping can also lead to decrease in beam current. Therefore, we expect a decrease in beam radius as the distance increases. Figure 3.10 shows the turn by turn plot of the beam size as a function of distance for three different beam currents. As the beam propagates a longer distance, the beam size decreases and then settles to a final value. The beam

self-matches itself into the ring. The error percent is calculated by assuming 2% error in the measurement of Cs which causes a 4% change in the beam size. There are some limitations on this diagnostic. Firstly, Cs becomes ill-defined at the beam ends. The higher the beam current, the faster the space-charge waves reach the beam ends and so this diagnostic is unreliable after some turns depending on the beam current.

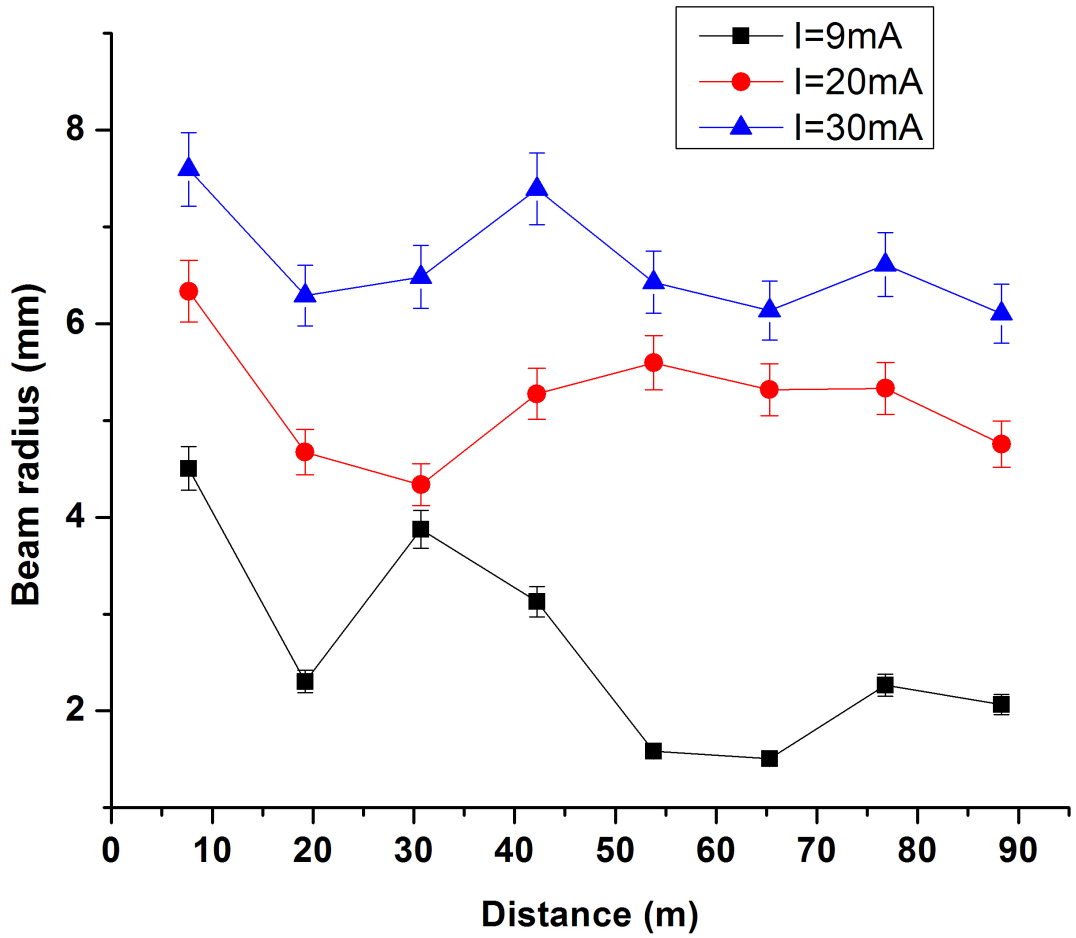

Figure 3.10: The average beam radius of various beams as a function of distance in the ring. The beam radius is calculated from measuring the wave-speed and beam current for each turn and applying equation(3.23). The beam size tends to decrease slightly as the distance increases.

Hence this diagnostic is useful only in that range of beam currents where the waves spend a longer time in the flat-top portion of the beam. Secondly, since the formula depends on the g-factor, this diagnostic cannot be applied for compressed beams or very short bunches. Finally, the perturbation applied to the beam should be very small. A large perturbation produces a non-linear wave which causes a larger error in the measurement of Cs and hence the beam size.

Another important longitudinal parameter in accelerators and storage rings is the longitudinal impedance. Though there are several types of impedances that can occur in a machine, we focus on space-charge impedance. When a charged particle beam travels through vacuum it does not experience a resistance directly like electrons moving inside a wire. Rather, the beam encounters impedance due to image space-charge fields that can interact back with the beam. The space-charge impedance per unit length is given by

$$Z_s^*(k,\omega) = -\frac{E_z(k,\omega)}{I_1(k,\omega)} \tag{3.24}$$

where E_z and I_1 are the perturbed longitudinal electric field and the perturbed current. The impedance is a function of frequency and hence is expressed in the Fourier transformed coordinates of space and time. Since low-amplitude space charge waves are dispersionless, we can assume $\omega \approx k\upsilon_0$ and the space charge impedance can be calculated as

$$Z_s^*(\omega_0) = -iX_s^*(\omega_0) \approx -i\frac{g\omega_0}{4\pi\beta^2\gamma^2 c}Z_0 \tag{3.25}$$

As can be seen from eqn (3.25) , the space-charge impedance is a function of the g-factor and the perturbation frequency for a give beam energy. Z_0 is the free space

impedance and equals 377 Ω. For a given perturbation wavelength, the space-charge impedance can be normalized as

$$X_s = \frac{X_s^*(\omega_0)\lambda_p}{Z_0} = \frac{g}{2\beta\gamma^2} \tag{3.26}$$

By measuring the g-factor, the space charge impedance can be calculated experimentally. We can extend this technique to calculate the growth rate of the slow wave or the decay of the fast wave [53]. We list the space-charge impedance for three different beam currents in the Table. As expected the table shows that when the beam current increases the product of beam current and the normalized space-charge impedance increases- a high current beam produces a larger self-field. The 20 mA beam with a perturbation of frequency 200 MHz (5 ns) would have a space-charge impedance X_s^*=12kΩ/m.

Table 3-2: Normalized Space-charge impedance values for different beam current as a function of distance as per eqn (3.26).

Distance (m)	I=9mA	I=20mA	I=30mA
7.67	12	9.6	8.3
19.19	16.6	11.7	9.6
30.71	13.0	12.2	9.4
42.23	14.5	10.9	8.5
53.75	19.2	10.5	9.5
65.27	19.6	10.81	9.8
76.79	16.7	10.8	9.3
88.31	17.4	11.6	9.9

3.5 Transverse effects of the space-charge waves

In a space charge dominated beam, as mentioned earlier, any line charge modulation manifests as a change in the beam radius to make the volume charge density a constant. We are also interested in the transverse effects because they may be responsible for nonlinear effects. To study the transverse effects of longitudinal modulation, we need diagnostics that can resolve the perturbation. In our case, the perturbation is 5 ns and hence we need a high resolution optical diagnostic. The fast phosphor screen emits UV light when a charged particle hits the screen and has a good temporal response making it suitable for our experiment. In our experiment, the

light from the phosphor screen is captured by a PIMAX camera and the image is stored in a computer. The fast phosphor screen and the camera were discussed in Chapter 2.

A 5-ns density perturbation is introduced on a 100-ns long beam using the laser. After injecting into the ring, the beam hits the fast screen at RC15 and emits a UV light. The light is captured by a PIMAX camera in the auto focus mode. After focusing the camera onto the beam, the camera is set to gated mode in which the camera is triggered by an internal pulse generator. The timing sequence is adjusted with the BPM trigger (RC14) and camera runs at 15Hz. Once the timing sequence is checked, a gate is set for 3-ns width. Finally, the internal sequence generator is turned on with the appropriate start time and end time. A window of 51ns is used to generate 17 images of 3-ns each. The camera collected images are stored in a single file which is then sliced into TIFF images for processing.

The wall current monitor output is shown in the Figure 3.11 indicating the width of the gate and the scanning range of the gate within the pulse. The integrated beam image when on the camera is in the auto-focus mode is shown in the Figure 3.12.

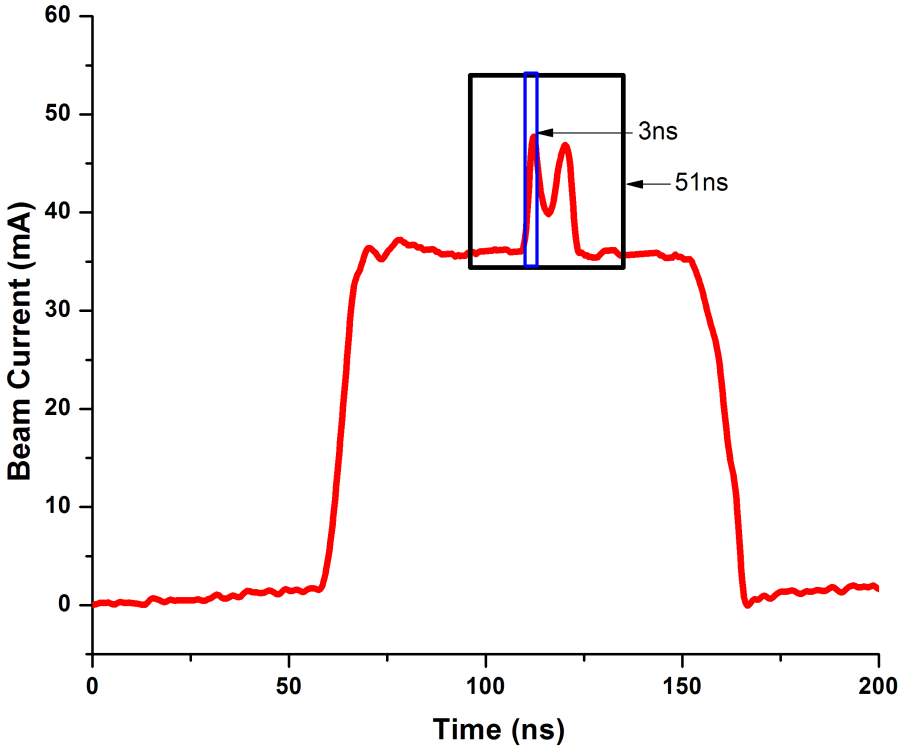

Figure 3.11: The wall current monitor signal at RC10 showing the measured beam current of 45mA peak with a 12% perturbation. The strength of the perturbation was deliberately increased to capture the splitting before the fast screen at RC15.

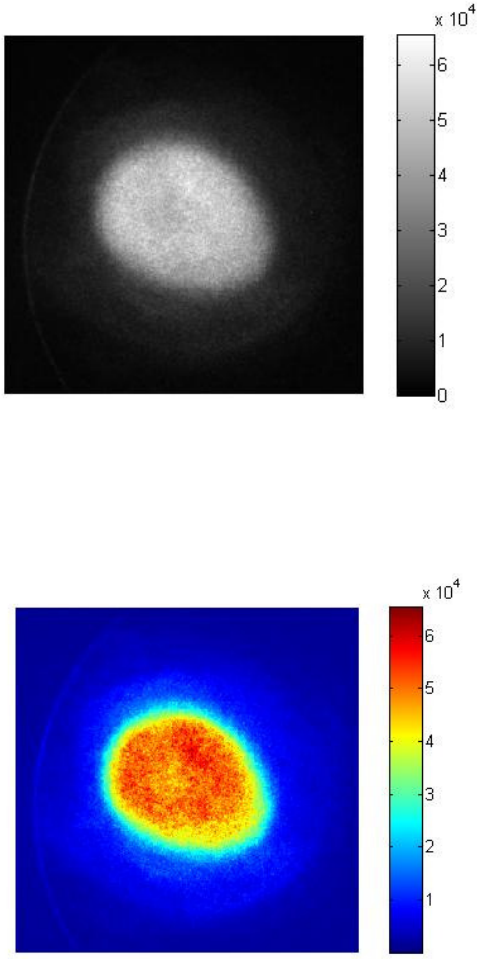

Figure 3.12: Integrated beam image of the whole beam. Top: 45mA with a positive perturbation; Bottom; the same beam in color-coded format.

The sliced images are processed and then calibrated according to the intensity of the light collected per gating. The montage is shown in the Figure 3.13 and Figure 3.14 below along with the calculated beam current.

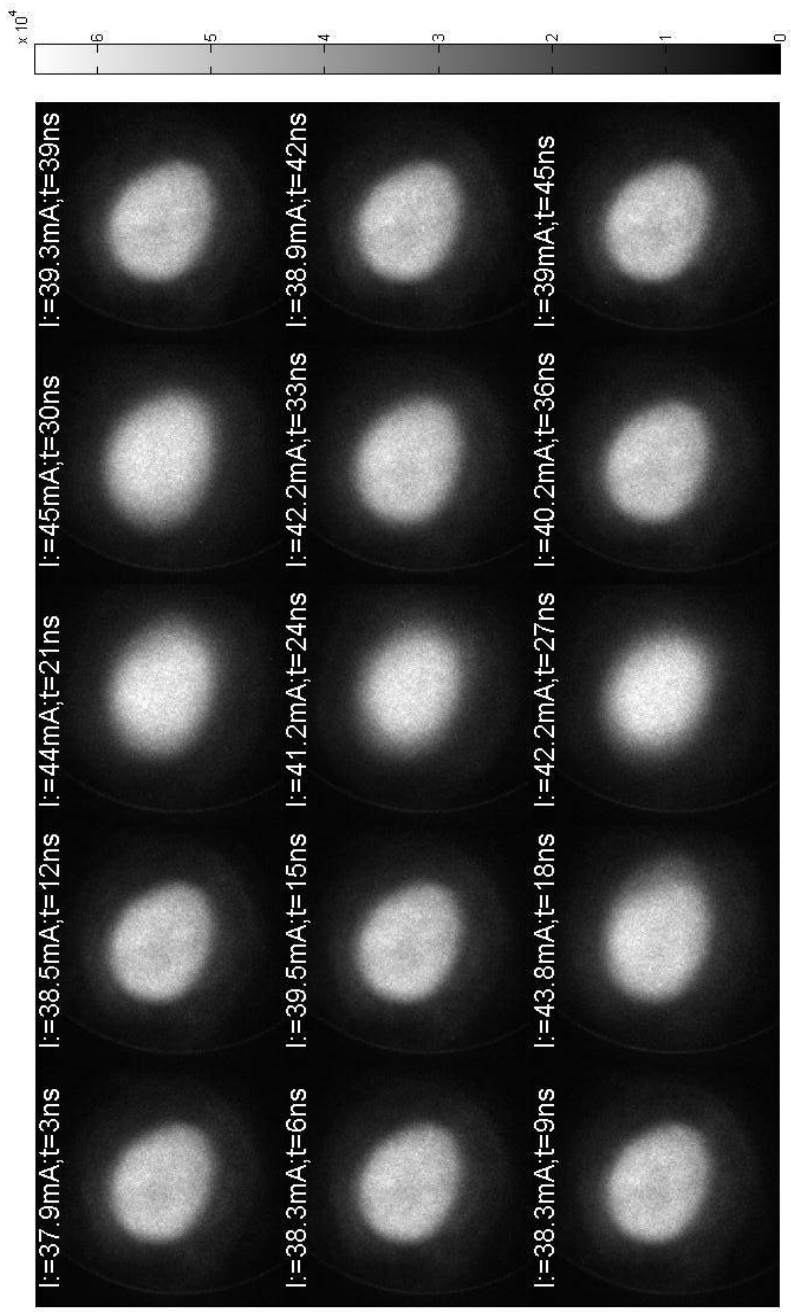

Figure 3.13: (Landscape) Black and white montage of the images captured by the camera in the 51-ns window at RC15. The total intensity of each image is calculated expressed in terms of the peak current. The peak beam current is 45mA. The montage is read from top to bottom starting from left to right. This is done to capture the x-motion of the beam.

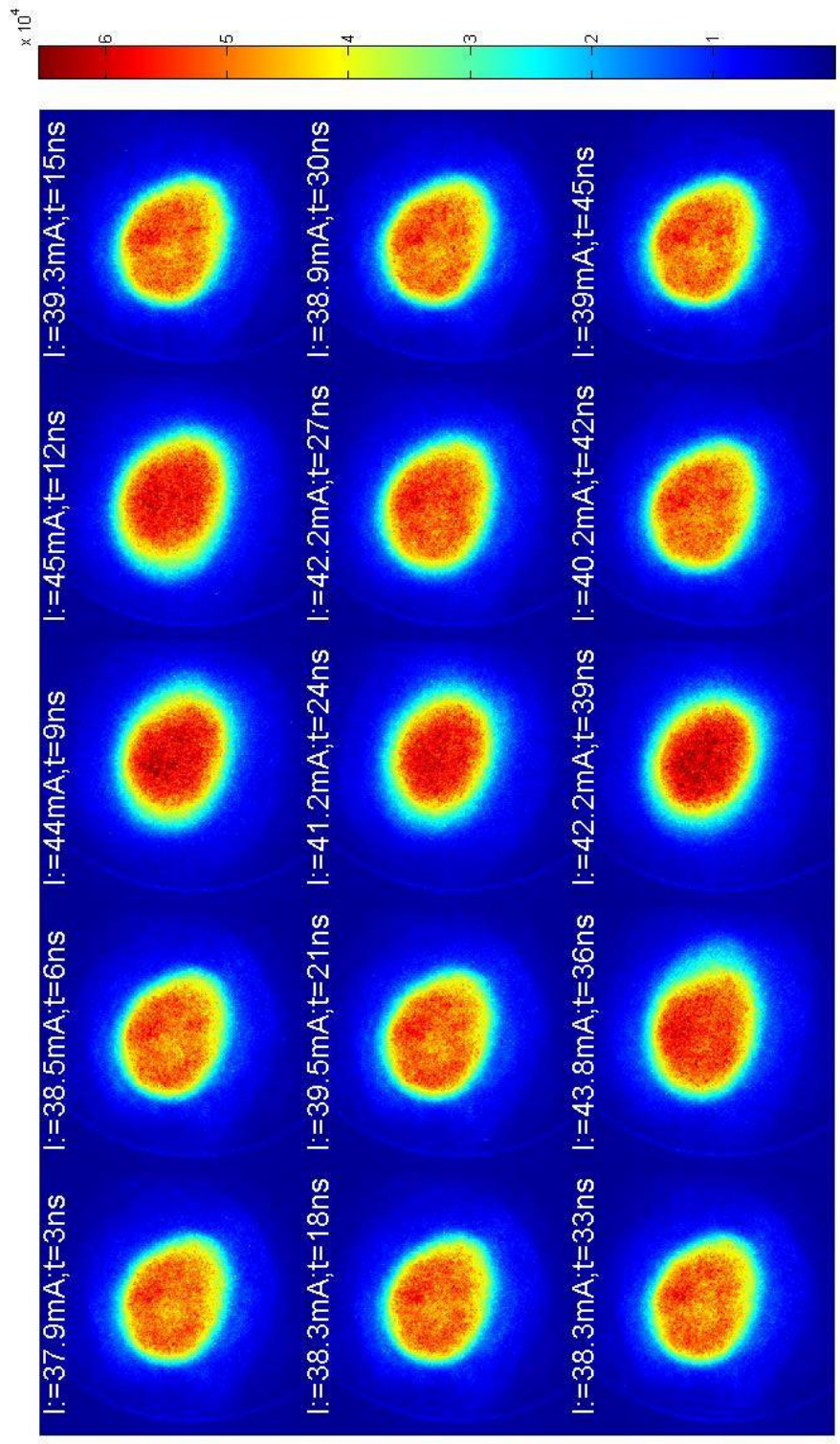

Figure 3.14: (Landscape) Color montage of the images captured by the camera showing transverse density waves at RC15. The beam size of the perturbed part of the beam is larger in x and the beam centroid moves transversely in the x-direction possibly to the dispersion effect of the ring.

We follow the following algorithm [54] to calculate the beam current and the centroid from each image of the montage. First, the total intensity of the image is calculated by adding intensity at each point of the image.

$$I = \sum_{i}^{N} \sum_{j}^{N} G(i, j), \tag{3.27}$$

where G(i, j) represent the intensity of the i-th row and j-th column of the image. The x and y centroid is then calculated by taking the first moment as following:

$$\begin{aligned} x_c &= \sum_{i}^{N} \sum_{j}^{N} iG(i, j) / I \\ y_c &= \sum_{i}^{N} \sum_{j}^{N} jG(i, j) / I, \end{aligned} \tag{3.28}$$

Where x_c and y_c are the x and y centroid respectively. The code similarly calculated the beam size by taking the second moment. Once the intensity is calculated for all the images, the image with the maximum intensity corresponds to the peak beam current. The rest of the images are then scaled to calculate the beam current for each image. The calculated sliced current for each gating is plotted as a function of time. This is shown in Figure 3.15.

The intensity pattern follows the current profile seen with the current monitor and hence confirms the linearity of the fast-screen with respect to charge.

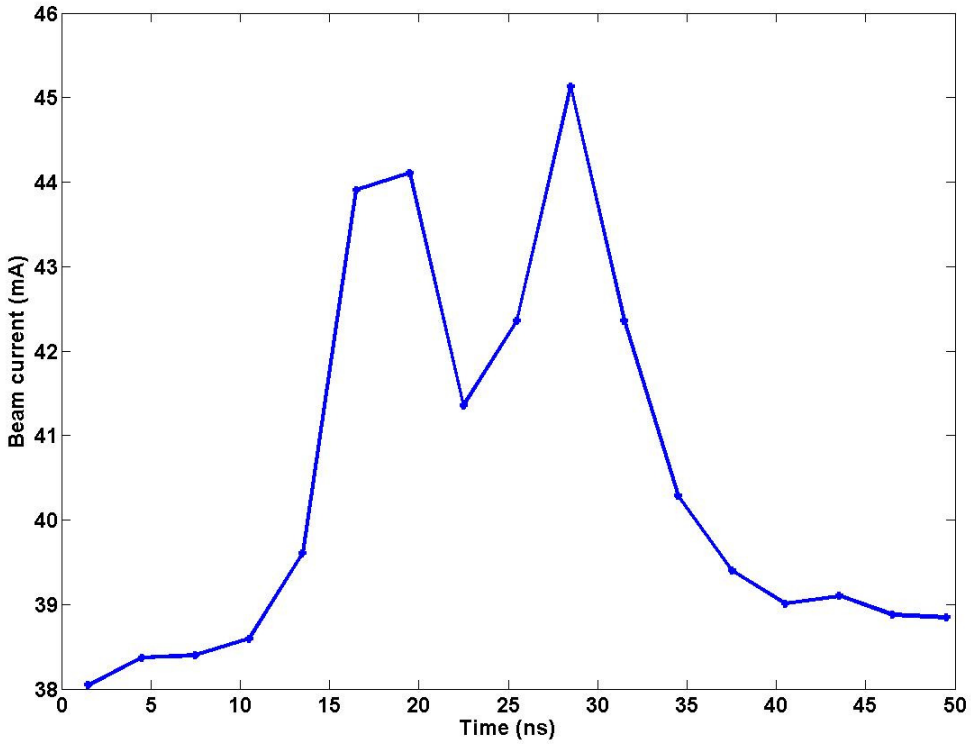

Figure 3.15: The plot of the slice beam current as a function of time. The total light intensity from the fast screen follows the fast and the slow waves. The measurements are at RC15 with a peak current of 45mA with a perturbation of 12%. The plot allows confirms the linearity of the screen with the charge.

The radius and the centroid of the beam are affected by the perturbation and are shown in Figure 3.16 and Figure 3.17 shows a displacement of centroid in the x-direction only. This is likely due to the velocity modulation introduced by the space-charge waves. The fast and the slow waves create an energy modulation within the beam which causes the perturbed part of the beam to move transversely in x-direction due to dispersion. This experiment indicates that a pure density modulation evolves into an energy modulation over time. The beam size increase is more pronounced in the x-direction because of the placement of the screen with respect to the UMER

FODO lattice. The plane of the phosphor screen is 2.7 cm from the lattice centre, so the UMER beam looks elliptical with major axis along x-direction [55]. Hence, though the beam radius increases inside the perturbation, the radius appears to increase only in the x-plane. In order to cross check these result from WARP, we need to perform a WARP 3-D simulation that takes into account the quads and the bends. A WARP R-Z simulation will not be sufficient.

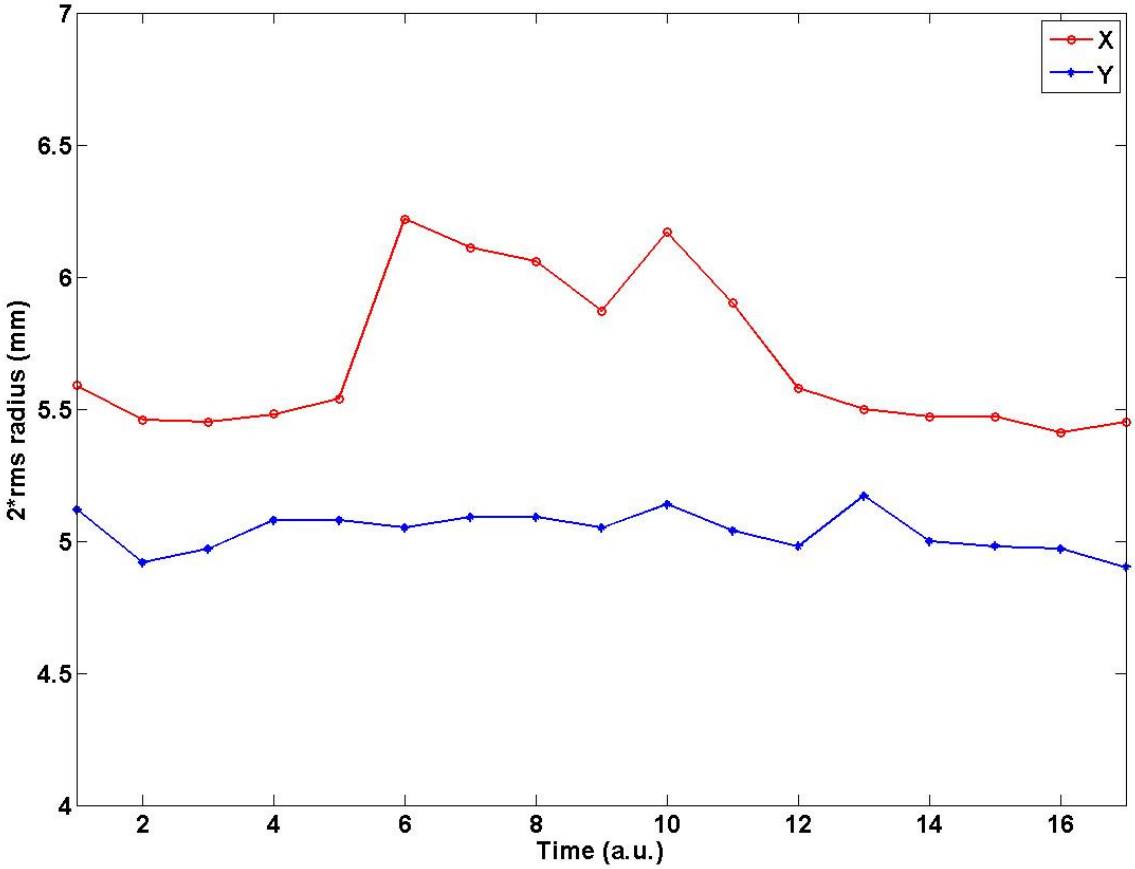

Figure 3.16: The RMS beam radius measured from the images collected at RC15 using the fast screen and camera as a function of time. There is a 10% increase in the x-radius with the perturbation. As predicted by the theory, the perturbation causes a radius change in a space charge dominated beam to keep the volume charge density a constant.

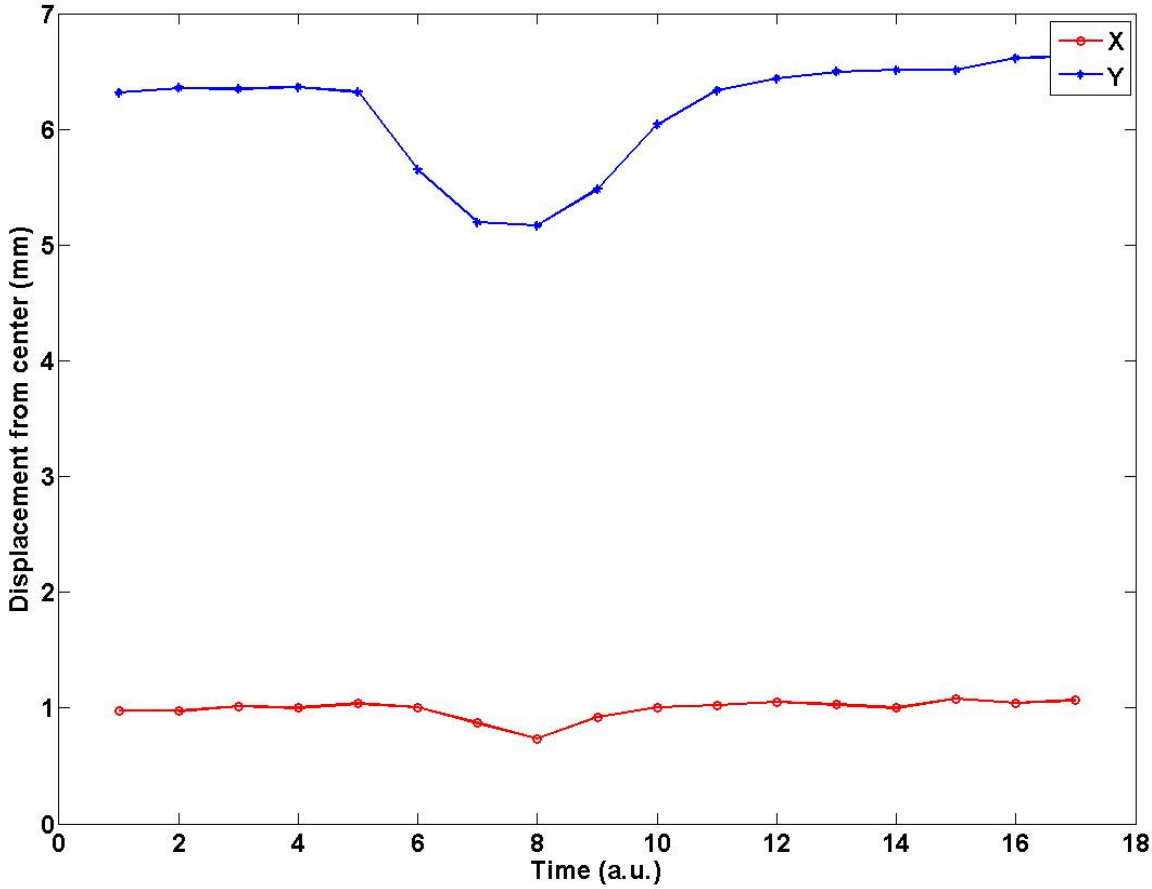

Figure 3.17: The centroid shift, the distance between the beam center and the pipe center, as measured from the images as function of time. The x-position of the beam centroid oscillates while the y-position of the beam centroid is relatively unchanged. This is due to the effect of the velocity modulation of the perturbation causing a shift in beam position due to the dispersion in the ring.

3.11 Summary

In this chapter, we derived the wave speed formula from 1-D cold fluid theory. We compared the measured values of the sound speed with theory and WARP simulation. The agreement is good within the linear regime and there is an evidence of non-linear behavior at larger amplitudes. We showed that space charge waves can also be used as diagnostics to measure beam size in UMER and finally we performed

progressive, time-sliced imaging of the fast and the slow waves using the imaging diagnostics to show the transverse effects of longitudinal perturbation due to space-charge. The experiment concluded that a pure density modulation evolves into an energy modulation over time. In free electron lasers, this mechanism can lead to an increase in the energy spread of the beam as follows: In a high brightness electron beam, density modulations at low-energies can evolve into energy modulations due to space-charge. Once, the beam gets accelerated and goes through a bunch compressor or a bend, these energy modulations can get converted into density modulations through dispersion. Now, due to these density modulations, the longitudinal charge density of the beam is not smooth anymore but is modulated at wavelengths much smaller than the bunch length. This can lead to coherent synchrotron radiation (CSR) in the bunch compressor and thus introduce additional energy modulation, which distorts the transverse and longitudinal phase-space of the beam and affects the FEL performance.

Chapter 4: Multiple perturbations: Propagation, Control and Nonlinearities

In this chapter we look at how multiple perturbations propagate in a space-charge dominated beam and ways to control them. We also show how a large perturbation can launch nonlinear wave that can lead to pulse train formation.

In real laboratory beams, often the beam has more than one perturbation. It may have multiple modulations resulting from cathode non-uniformities, RF fluctuations, varying impedances along the beam pipe, etc. Such modulations occur throughout the beam and can vary in their frequency and amplitude. Hence, by understanding how multiple perturbations evolve in a space-charge dominated beam, we can control them in real laboratory beams. In Section 4.1, we discuss generating and propagating multiple perturbations on a beam. In Section 4.2, we then present experimental results on how to control the density perturbation by modulating the beam energy. Finally in Section 4.3, we show how a large perturbations can lead to non-linear wave propagation and thus to pulse train formation.

4.1 Generating multiple perturbations on a beam:

In the previous chapter, we showed how a single perturbation can be generated using a laser. Here, we take advantage of the photoemission technique to add a second perturbation. For this, we installed another Minilite laser system that used the same optics as the first one to introduce a second density modulation on the beam. By adjusting the timing of the pulses that trigger the laser systems, the distance between the two perturbations can be adjusted. This allows us to introduce independently controlled modulations (by adjusting the laser power) with controlled

separations (by changing the trigger timing). Figure 4.1 shows a beam current profile with two density perturbations (A and B) measured at the current monitor in the injection line.

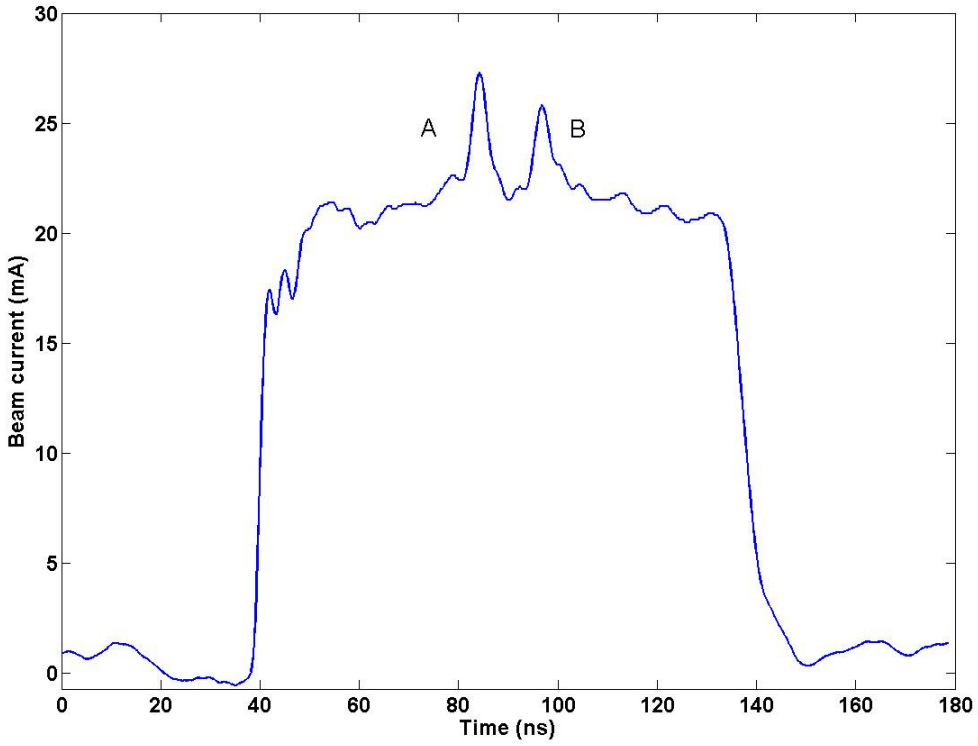

Figure 4.1 : Beam current profile measured using the Bergoz current monitor before injection into the ring. Two 5-ns pure density perturbations are introduced using two lasers. The time between A and B is 15ns. The beam current is 21 mA with 6 mA (A) and 4.5 mA (B) perturbation.

4.1.1 Experiments on a beam with multiple perturbations:

The beam shown in Figure 4.1 was injected into the UMER ring and the beam current profile was measured using the wall current monitor at RC10 for nine turns. Figure 4.2 shows a 3-D turn by turn plot of the measured beam current profiles. After the perturbation splits into a fast and a slow wave, the fast and slow waves from each perturbation travel toward the head and the tail of the beam, respectively, at the sound speed as discussed in Chapter 3. The slow wave from one of the perturbations (A-closer to the head) and fast wave from the other perturbation (B-closer to the tail) superimpose on each other in the second turn and then cross each other. Hence, in the second turn, the amplitude of the perturbation near the center is higher compared with the other peaks. The wave velocity of each of the perturbation (A and B) is measured and is shown along with 1-D cold fluid theory predictions in Figure 4.3. The black curve is the value of wave speed calculated from theory using the measured peak current. The red line corresponds to the experimentally measured value of C_s using the center-difference method described in Chapter 2. The blue line values are from the WARP simulation which we discuss in the following section.

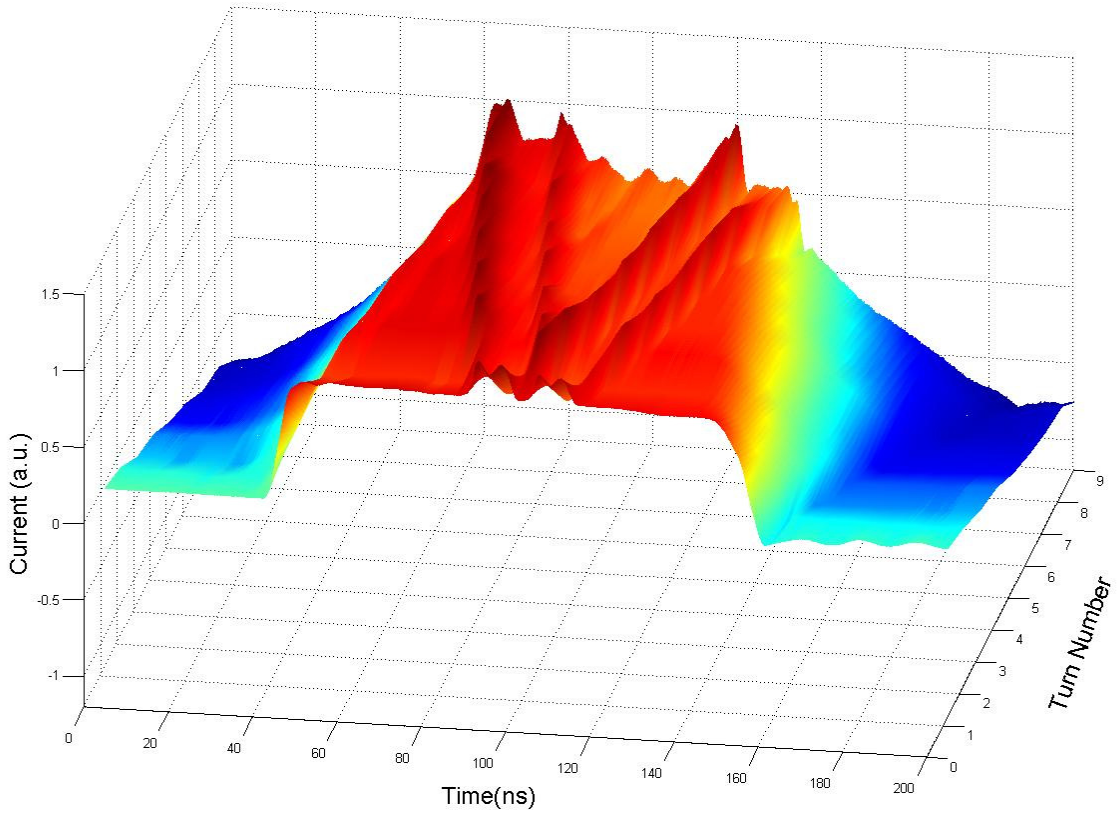

Figure 4.2: : 3-D plot of beam current evolution with two density perturbation. The plot is generated by interpolating the turn by turn data obtained using the wall current monitor. The waves are observed to superimpose and cross each other between turns 2 and 4. The injected beam current is 24mA.

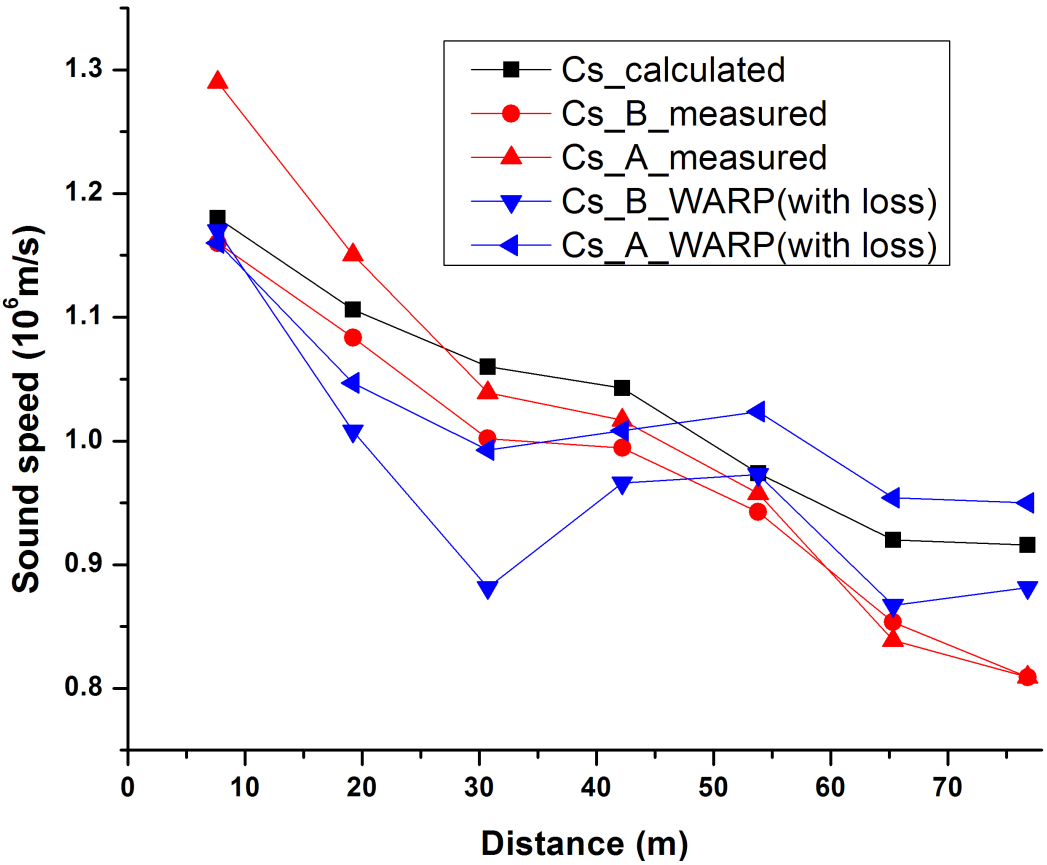

Figure 4.3:Graph showing the value of sound speed of the perturbations A and B compared with the theoretically predicted values over multiple turns. The sound speed is higher for A compared to B because of the higher strength of the perturbation A (see Chapter 3) . The injected beam current is 24 mA.

4.1.2 WARP Simulation of beam with multiple perturbations:

The beam profile obtained from the current monitor shown in Figure 4.1 is used to initialize the current distribution in WARP. The profile is then smoothed using a weighted average filter (of width 3) in the simulation to filter noisy spikes in the current distribution due to the injection and re-circulation pulsing circuits. The initial transverse distribution used is a semi-Gaussian (uniform in density and Gaussian in velocity). We used one million particles in the R-Z simulation and took measured beam loss into account. We used 64 cells in R-direction and 256 cells in Z-direction with a thermal spread of 1.5e5. After calculating the necessary smooth

focusing for matching the beam, the beam is transported to a distance equivalent to 8 turns.

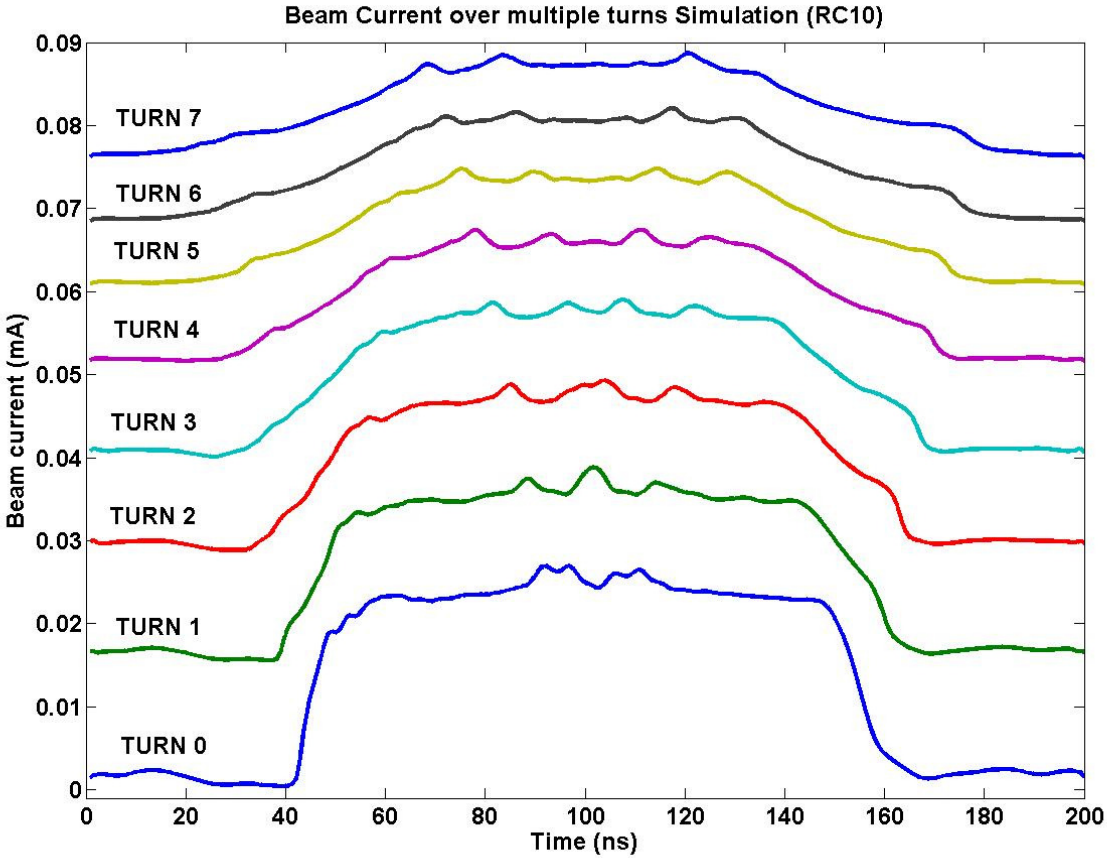

Figure 4.4: WARP Simulation results of a beam with multiple density perturbations. The slow wave of one perturbation and the fast wave from the other perturbation superimpose each other on the second turn and then cross. The beam used in simulation is the beam shown in Figure 4.1. The WARP simulation used one million particles.

Seven turns from the WARP simulation in Figure 4.4 shows how the fast and the slow waves from each perturbation superimpose and cross each other. We calculated C_s from WARP and compared with the experimental and the theoretical values. This is plotted in Figure 4.3 as blue lines. The same procedure to calculate C_s using the center-difference method mentioned in Chapter 3 is also followed here. As the graph shows, the waves from perturbation A travel faster than the perturbation B. This is

because of the large amplitude perturbation (A) travels faster compared to low amplitude perturbation (B) as discussed in Chapter 3. The slightly larger discrepancy with the theory may be possibly due to the multiple perturbations on the beam changing the beam size along the beam causing a variation in g-factor, which the 1-D theory ignores. In other words, transverse effects like variation in g-factor due to beam loss must be taken into account in a lab-frame, WARP 3-D simulation.

A long pulse length experiment with multiple perturbations:

To track the evolution of the waves over a long timescale, we need the waves to remain in the flat top portion of the beam for a longer time. So, we increased the beam pulse length to 150 ns and performed the two laser experiment. The beam current was 12.6 mA with a 1.7 mA perturbation (A) and 1.0 mA perturbation (B). We show the result of the experiment in Figure 4.5 . A straight line fit of the wave peaks of the respective perturbation is also shown. It shows the linear variation of the distance between the waves (with a slight change due to change in current) as the turn increases. In conclusion, within the linear regime, the presence of another density perturbation does not affect the velocity of the waves and each perturbation behaves as if it were the only perturbation present on the beam.

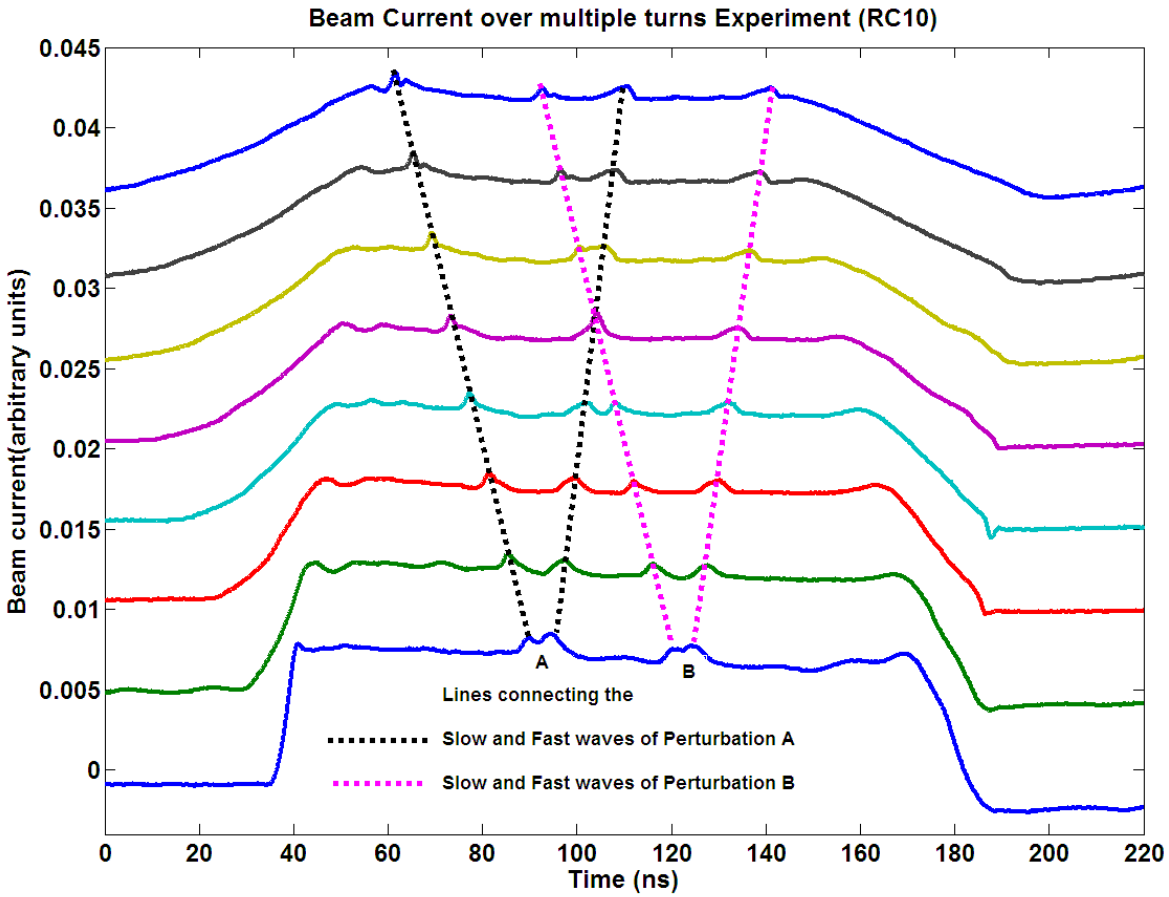

Figure 4.5: Experimental results of a UMER beam with multiple perturbation. The beam current is 12.6mA with a 1.7mA perturbation (A) and 1 mA perturbation (B). The waves approaching each other, superposing each other and then crossing each other is clearly observed. The lines connect the peaks of the fast and the slow waves in each perturbation.

4.2 Controlling density perturbations on a beam:

In most applications density or velocity perturbations on a beam is undesirable. So any method to eliminate or at least control the perturbation will be useful in preserving the beam quality. As an example, to clean a beam pulse before it is injected into a bend can prevent unwanted radiation. In this section, we discuss techniques for controlling a density perturbation using a energy modulation.

Several beam experiments were conducted at UMER, either by changing the perturbation strength while keeping the beam current constant or by changing the beam current while keeping the perturbation current constant. All these experiments showed a trend: space-charge waves superpose and cross each other just like linear waves would. This is because of the dispersionless property of the space-charge waves. The waves behave as if they are independent of each other and hence superimpose and cross each other without a change in shape. Since linear waves superimpose each other constructively, they can also superpose destructively. Thus, if a space charge wave interacts with another space charge wave of the same amplitude and pulse width but different polarity, then the waves will cancel each other. This principle can be used to cancel the propagation of a fast or a slow wave.

In order to test this principle, introduced a density modulation to create a positive slow wave and then we used an energy modulation to create a fast wave with negative polarity. By adjusting the timing, amplitude, and the pulse width of the modulation carefully, we were able to suppress the propagation of the fast wave.

We show how energy modulations can be used to control density modulations in a beam in the following section. The basic idea behind the technique can be described as follows: the electrons in the fast or slow waves are travelling with a velocity v_0+C_s or v_0-C_s in a density modulated beam, respectively, where v_0 is the beam velocity. Adding energy modulation to such a beam creates velocity waves that interfere constructively (depending on the phase) with the velocity waves produced by the density modulation. By appropriately choosing the amplitude and the phase of the energy modulation, we can cancel the fast or the slow wave. The perturbation beam current becomes zero. We call this coherent pulse flattening. This technique

assumes that the density perturbation is small. In other words, the perturbation is in the linear regime and the waves are not dispersing. Also, the time scale for applying the correction should be small compared to the time scale for the waves to phase mix. In other words, the beam should have low incoherent energy spread.

We show in the next section how an energy modulation can produce current waves of opposite polarity [30] and how waves in a density modulated beam can be controlled using energy modulation.

4.2.1 Coherent pulse flattening and 1-D cold theory:

From cold-fluid theory, an initial velocity perturbation of the form: $v_1(z=0,t)=\delta v_0 h(t)$ and a density perturbation of the form: $i_1(z,t)=i_1(0,t)=\eta i_0 h(t)$, where the h(t) is the shape of the velocity perturbation with unit amplitude ,δ is the strength of the velocity perturbation and η the strength of the density perturbation, evolves according to the following linearized equations [56].

$$i_1(z,t)=-\frac{i_0}{2}\left[\delta\frac{v_0}{c_s}-\eta+(\eta-\delta)\frac{c_s}{v_0}\right]h\left(t+\frac{z}{c_s}\right)+\frac{i_0}{2}\left[\delta\frac{v_0}{c_s}+\eta+(\eta-\delta)\frac{c_s}{v_0}\right]h\left(t-\frac{z}{c_s}\right) \tag{4.1}$$

$$\lambda_1(z,t)=-\frac{\lambda_0}{2}\left[\delta\frac{v_0}{c_s}-(\eta-\delta)\right]h\left(t+\frac{z}{c_s}\right)+\frac{\lambda_0}{2}\left[\delta\frac{v_0}{c_s}+(\eta-\delta)\right]h\left(t-\frac{z}{c_s}\right) \tag{4.2}$$

$$v_1(z,t) = \frac{v_0}{2}\left[\delta - (\eta-\delta)\frac{c_s}{v_0}\right]h\left(t+\frac{z}{c_s}\right) + \frac{v_0}{2}\left[\delta + (\eta-\delta)\frac{c_s}{v_0}\right]h\left(t-\frac{z}{c_s}\right) \tag{4.3}$$

First of all, we notice that if η=0, then the current exhibits a pair of space charge waves with opposite polarity. This shows that a pure energy modulation creates a pair of space charge waves in beam current which has opposite polarity.

Let us suppose we want to cancel the slow wave (or fast wave) through energy modulation. By setting the first or second term, respectively, to zero in eqn. (4.1), we get:

$$\delta\frac{v_0}{c_s} \mp \eta + (\eta-\delta)\frac{c_s}{v_0} = 0$$
$$\Rightarrow \delta = \eta\left(\frac{c_s}{v_0 \mp c_s}\right) \tag{4.4}$$

Where the + sing is for the fast wave and – sign is for the slow waves. So, for a given strength of the density modulation (η), a particular value for the strength of the velocity modulation (δ) calculated from the eqn (4.4) can cancel the fast wave. To cancel the slow wave we set the second term of the eqn (4.1) to zero and again we get eqn (4.4) but with a sign change in the denominator.

By modulating the charge, we get waves in velocity and current. Similarly by modulating velocity we get waves both in charge and current. Therefore, by simultaneously introducing a density and a velocity wave, we can control the current

perturbation on a beam. The value of δ to cancel a given density modulation depends on both η and the sound speed (C_s), and therefore depends on the beam current (I) and beam energy as well. We plot the values of δ as a function of η and C_s for a 10-keV beam. This is shown in the Figure 4.6 . As expected, a larger current with a stronger density modulation requires a stronger energy modulation to cancel the density perturbation.

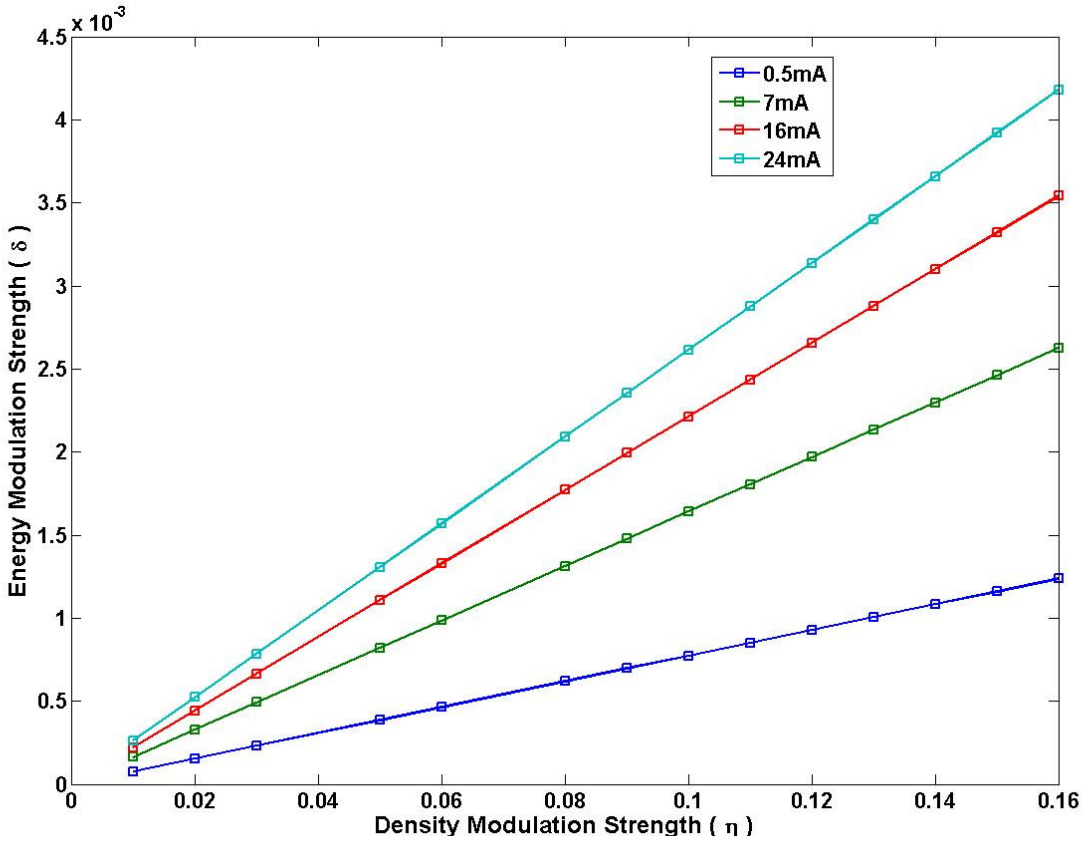

Figure 4.6: Graph showing the strength of velocity modulation (δ) required to cancel density modulation of initial strength (η) for different UMER beam currents at 10 keV. A high current beam with a larger perturbation needs a larger energy modulation.

4.2.2 Analytical Modeling of Coherent pulse flattening using MATLAB:

We used a MATLAB to numerically solve eqns (4.1), (4.2) and (4.3) to observe how a density modulated beam behaves when it is energy modulated. We assumed a Gaussian shaped perturbation with a full-width half maximum of 5ns. First, we show what happens when a beam starts with a pure density modulation. Next, we show what happens when a beam starts with a pure energy perturbation and show that a fast and a slow wave of opposite polarity are generated. To get a clearer view, we show the evolution of all the quantities, charge, velocity and current with respect to time. Finally, we superimpose both the density and the energy modulation to show how, by choosing the correct strength (δ) for the energy modulation from equation (4.4) , one of the waves could be cancelled. We note that the energy modulation is applied at a distance of RC4 (z =3.8 m) downstream.

In the simulation, we use a 20 mA beam with a 10% density modulation (η=0.1). We begin the simulation with no energy modulation (δ=0). The results are shown in the Figure 4.7. We then set η=0 and set δ=0.0022, a pure velocity modulation. The results are shown in Figure 4.8 . Finally, we set η=0.1 and δ=0.0022 , so that the beam starts with a density modulation and then a velocity modulation is applied. The results under this condition are shown in Figure 4.9 illustrating the cancellation of the fast wave but the amplitude of the slow wave is doubled. By reversing the polarity of δ, we can also cancel the slow wave. This is shown in Figure 4.10. We used three colors in the simulation to indicate the following: the blue color indicates a beam with just a density modulation, the red

color indicates a beam with just a velocity modulation and the black color sums the two beams to bring out the effect of the modulation. We add them due to the linearity of fluid equations in the 1-D cold fluid theory.

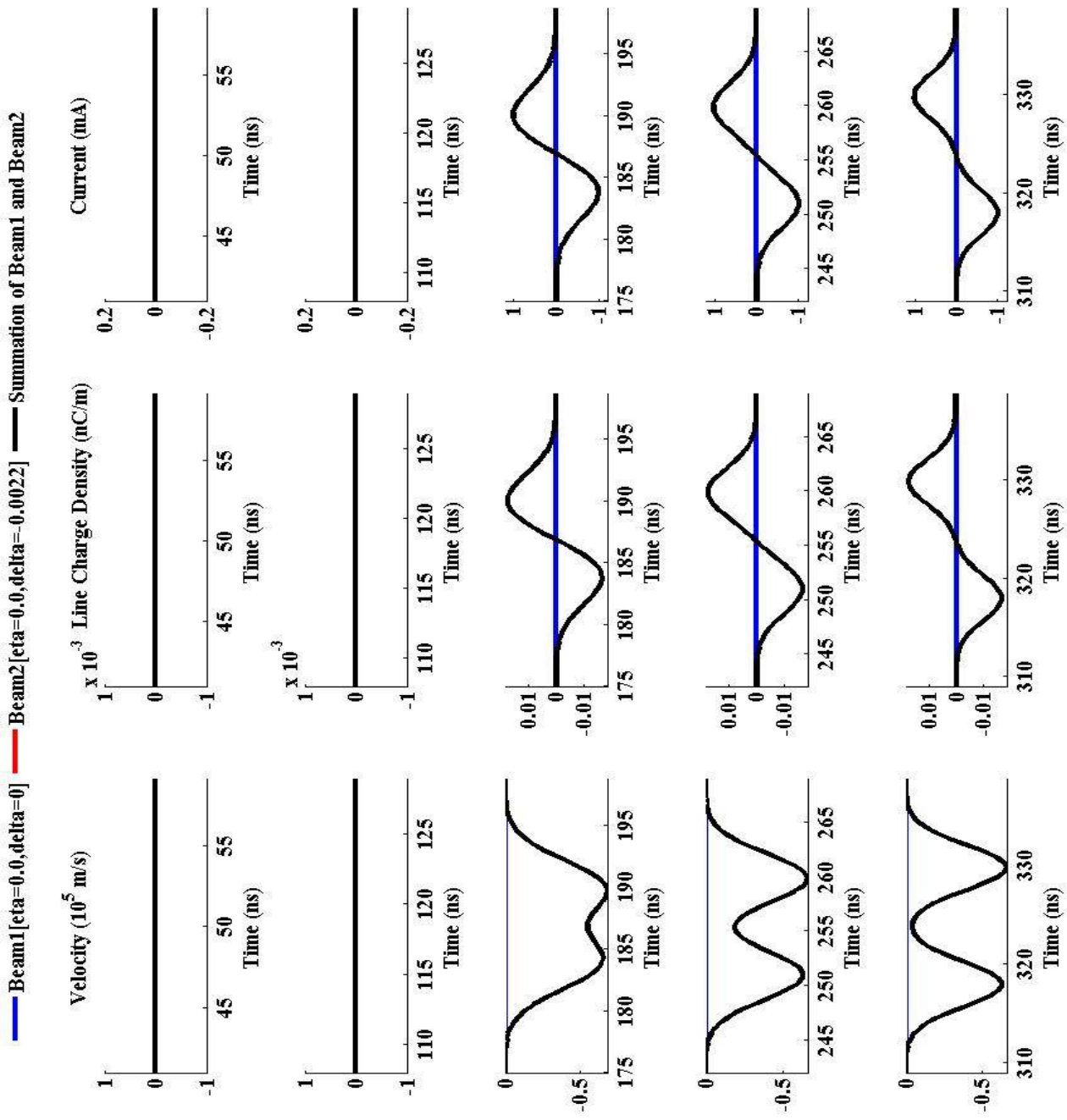

Figure 4.7: (Landscape) MATLAB Simulation showing the effect of velocity modulation on a beam. The beam current is 20mA and the velocity modulation is 0.2%. In the current space, the fast and the slow wave have opposite polarity.

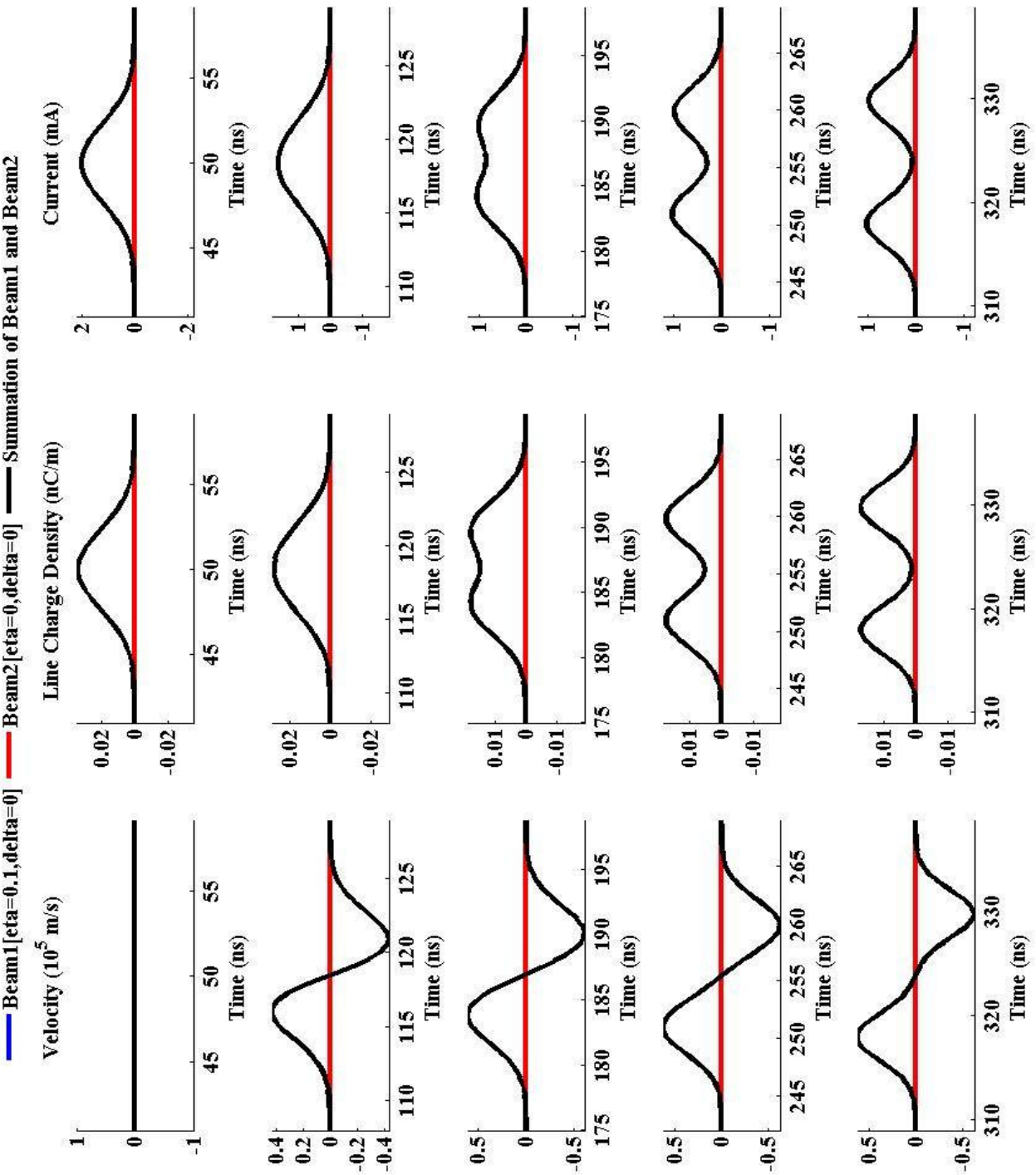

Figure 4.8: (Landscape)) MATLAB Simulation showing the effect of density modulation on a beam. The beam current is 20mA and the density modulation is 10%. In the current space, the fast and the slow wave have same polarity, while they have opposite polarity in the velocity space.

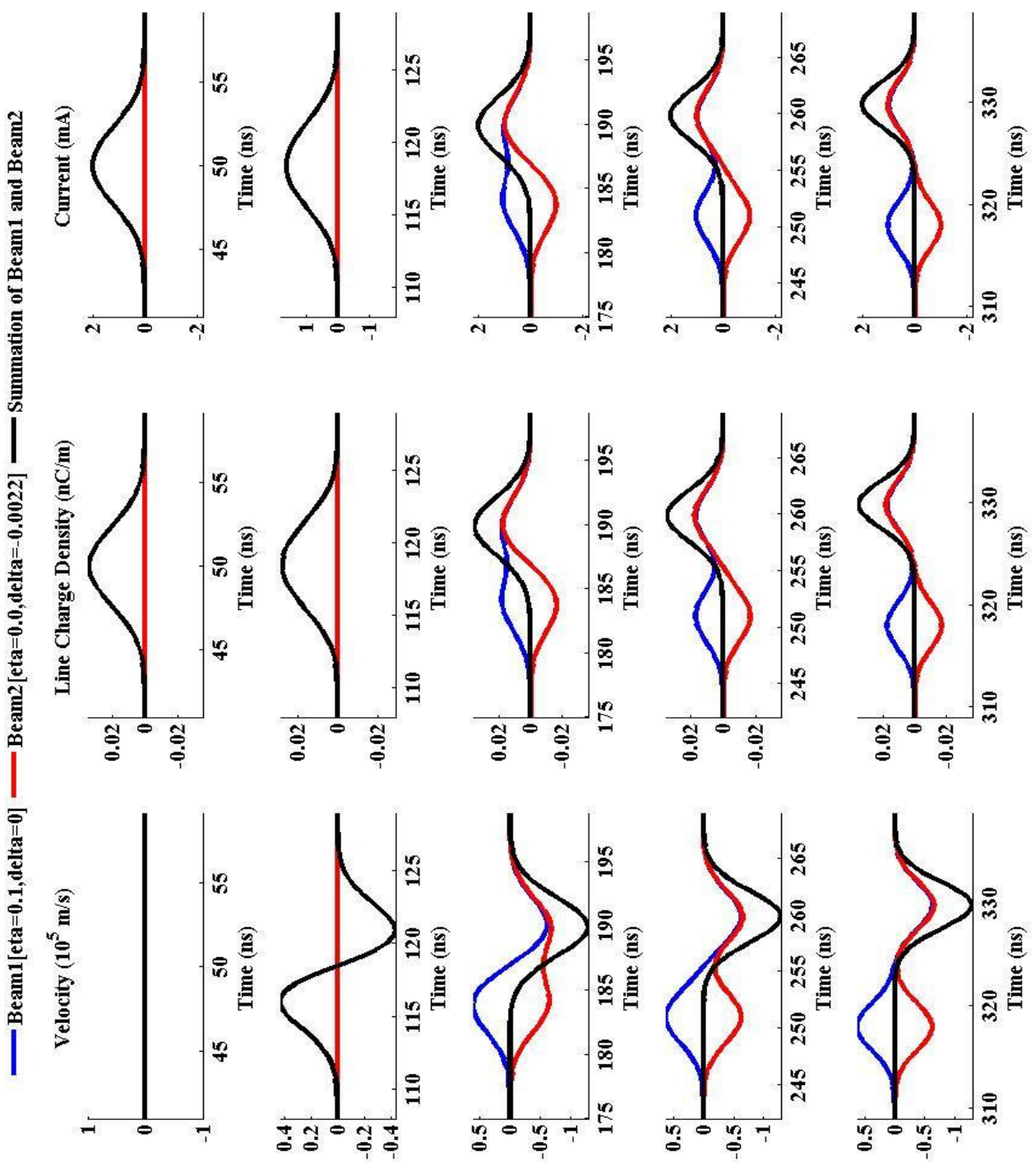

Figure 4.9: MATLAB Simulation showing the cancellation of the fast wave. The beam current is 20mA and the density modulation is 10% with a velocity modulation of 0.2%. Though the fast wave is cancelled, the amplitude of the slow wave increases.

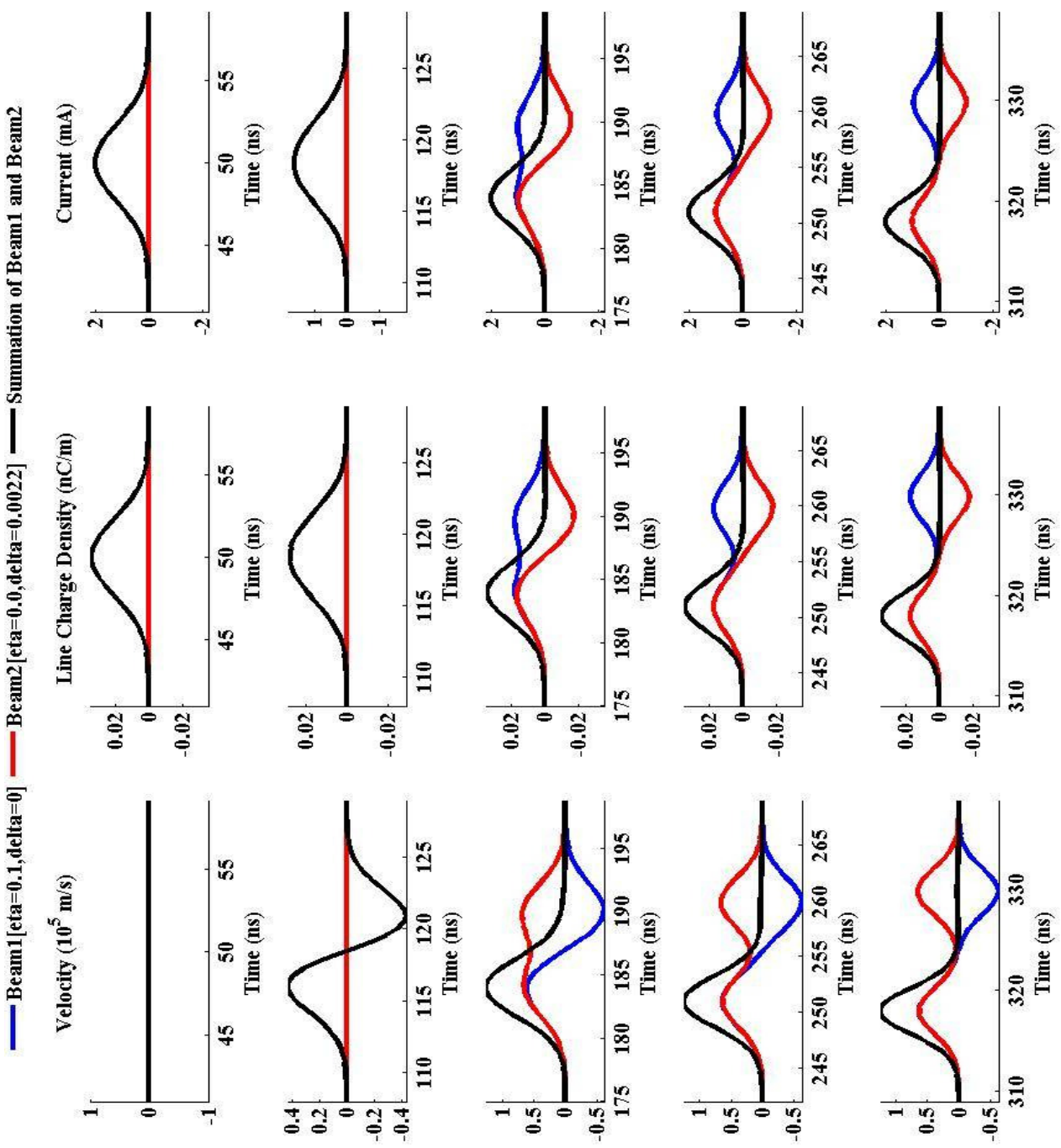

Figure 4.10: (Landscape) MATLAB Simulation showing the cancellation of the slow wave. The beam current is 20mA and the density modulation is 10% with a velocity modulation of 0.2%. Though the slow wave is cancelled, the amplitude of the fast wave doubles.

4.2.3 Experimental cancellation of density modulation by controlled energy perturbation:

In order to test the prediction from analytical calculation, we injected a 7 mA beam with a density perturbation of duration 8 ns. Because the width of a single laser pulse is 5 ns, we combined two laser pulses (from two similar laser sources) and created a single 8ns density perturbation. We injected the beam into the UMER ring, as shown in Figure 4.11. Next, the lasers were switched off and we introduced an energy modulation on the beam. The beam after the energy modulation is shown in the Figure 4.12. After making the timing adjustment to make the energy modulated waves occur at the same time as the fast (or slow wave) from the density perturbation, the density perturbation was turned on. The amplitude of the energy modulation was increased to cancel the fast wave as shown in the Figure 4.13. It also shows that the slow wave is not propagating as predicted by the simulation. We then repeated the experiment by changing the polarity of the energy modulation, to cancel the slow wave. We repeated the experiment for the 23 mA and 1 mA beam. In each case, the fast wave was cancelled and the beam carried only the slow wave.

These experiments show that when a controlled energy modulation is introduced on a density modulated beam and when the shape and the timing of the modulation is matched with the original perturbation, coherent pulse flattening occurs. In the experiment, we apply an external voltage to the beam ($E_{applied}$) to the beam. In order to compare the experimental values $E_{applied}$ with the theoretical

values of δ in equation (4.4) , we use the following conversion in the non-relativistic limit:

$$\Delta E = 0.5m(\upsilon_1 + \upsilon_0)^2 - 0.5m\upsilon_0^{\,2} \Rightarrow 0.5m\upsilon_1(\upsilon_1 + 2\upsilon_0)$$
$$\frac{\Delta E}{E} = \frac{0.5m\upsilon_1(\upsilon_1 + 2\upsilon_0)}{0.5m\upsilon_0^{\,2}} = \frac{\upsilon_1^{\,2}}{\upsilon_0^{\,2}}\left[1 + 2\frac{\upsilon_0}{\upsilon_1}\right] = \delta^2 + 2\delta \qquad (4.5)$$
$$\Rightarrow \delta^2 + 2\delta - \frac{\Delta E}{E} = 0$$
$$\cong \delta = \frac{\Delta E}{2E} = \frac{E_{applied}}{4E}$$

ΔE is the coherent energy spread for a single wave and E is the beam energy. We note that the factor of two arises because when the wave splits, the strength of the energy modulation is halved.

Table 4-1: Table comparing of the velocity modulation strength predicted by theory to cancel the perturbation and the experimental values.

Beam current	η	δ **(theory)**	$\Delta E = \frac{E_{applied}}{2}$ **(V)**	δ **(Experiment)**
1 mA	0.06	4.6e-4	20	5e-4
7 mA	0.05	8.2e-4	40	1.0e-3
23 mA	0.1	0.026	160	0.040

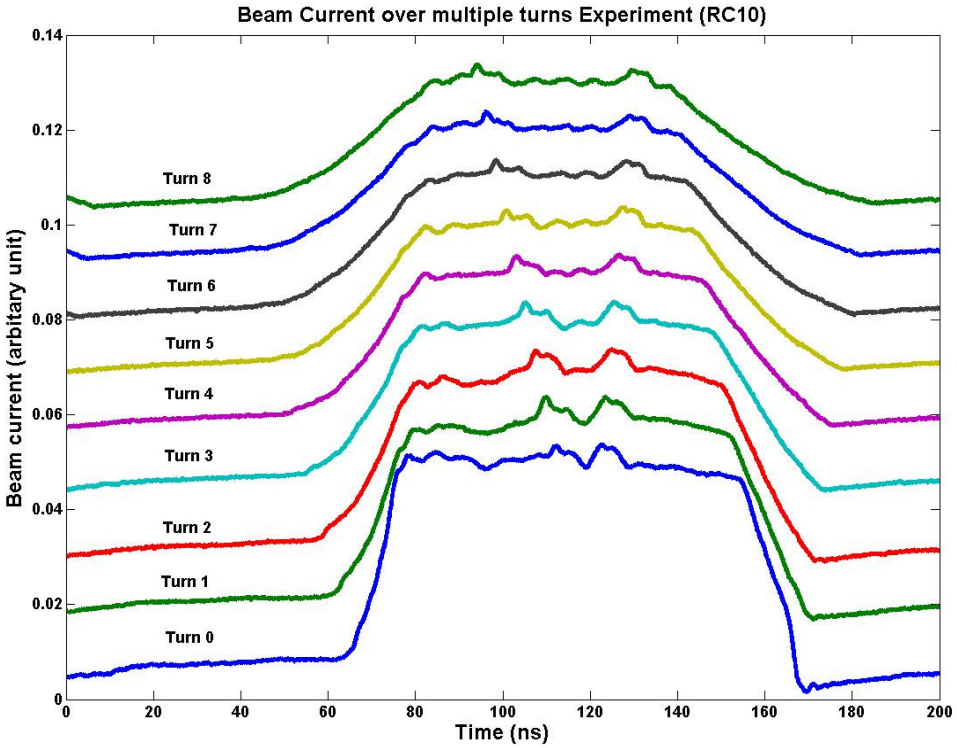

Figure 4.11: Turn-by-Turn plot of the UMER beam (7 mA) with a density perturbation (8-ns). The perturbation width is 5ns from a single laser. Therefore, two lasers were combined to get an 8 ns density perturbation. The fast and the slow waves have the same polarity.

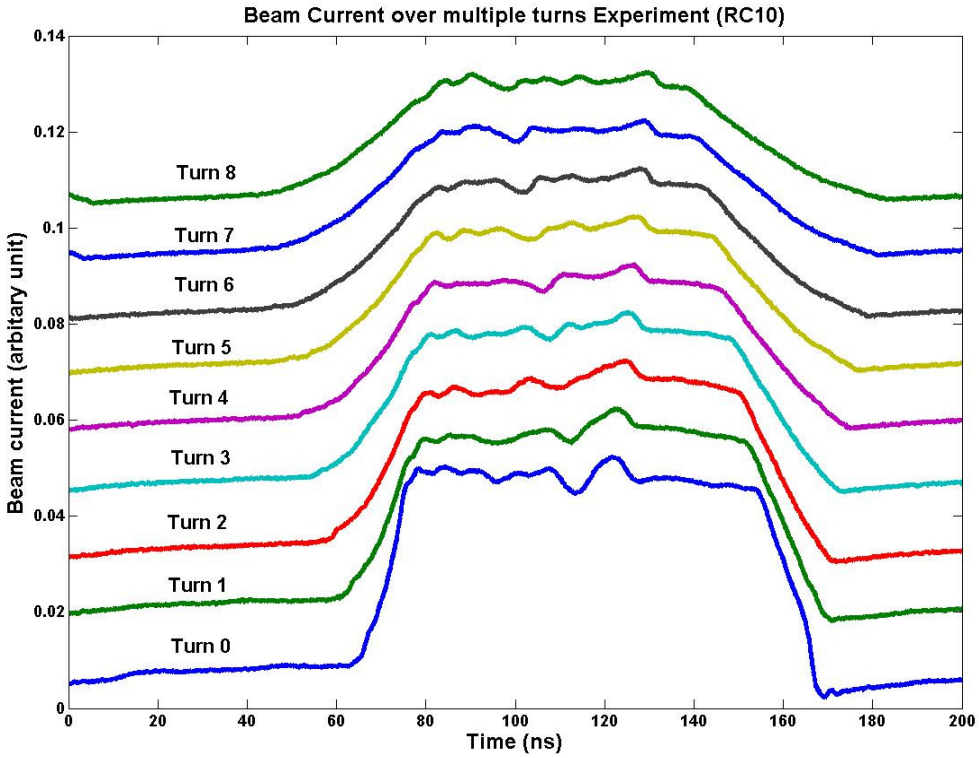

Figure 4.12: Turn-by-Turn plot of the UMER beam (7 mA) with a velocity perturbation (8-ns). The fast and the slow waves have opposite polarity. This property allows the velocity perturbation to cancel a density perturbation, which generates a fast and a slow wave but with the same polarity.

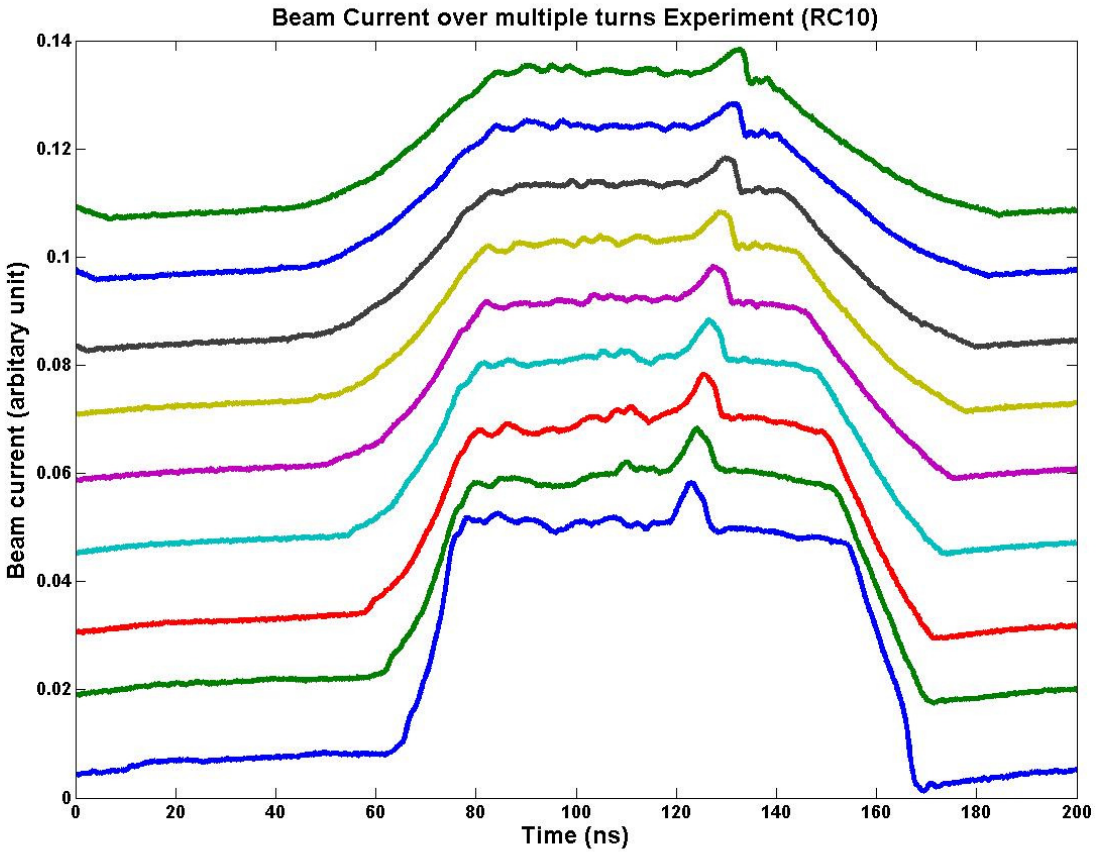

Figure 4.13: Turn-by-Turn plot of the UMER beam (7 mA) with a velocity perturbation (8-ns) and a density perturbation (8 ns). Only the slow wave is propagating on the beam. The fast wave of the density modulation is cancelled by the fast wave of velocity modulation because of opposite polarity while the slow waves, which are of same polarity, adds up.

The experimentally determined value δ for different beam current for different perturbation strength is listed in Table 4-1. As the Table 4-1 shows the value of the voltage need to cancel a perturbation increase with the strength of the initial density perturbation. The discrepancy between the theory and the experiment is possibly due to variation of beam size inside the perturbation.

In our experiment we used a coasting UMER beam with 10-keV with no acceleration. Accelerating the beam would change the beam energy and hence reduce the required value of δ for cancelling the density modulation. When a low energy

beam is accelerated, C_s decreases and v_0 increases, causing the ratio of C_s/v_0 decrease substantially. Therefore if a density-modulated beam is accelerated quickly, the energy modulation required to cancel the density modulation will be reduced from eqn (4.4). Ongoing work on acceleration [57] will clarify the timescale needed to perform the cancellation experiment in UMER.

4.2.4 Limitations of the coherent pulse flattening technique:

There are some limitations in the coherent pulse flattening experiment demonstrated above. In principle, either the fast or the slow wave can be cancelled but not both of them. This is because UMER, as of writing, has only one energy modulator to cancel either the fast or the slow wave. By adding another energy modulator we can, in principle, cancel the other wave. Also, if we start with a pure fast or a pure slow density wave, we can use the coherent pulse flattening technique to cancel the wave. Methods to generate a pure fast or slow density wave in a beam has been investigated before [25]. In UMER, out of the three glass gaps, currently one of the glass gaps is used as an induction module to introduce the energy modulation on the beam while the second glass gap is used as a current monitor. We still have one glass gap left which could be used to cancel the remaining wave in the beam. Also, in our experiment when the density modulation was in the linear regime and the energy modulation was applied in a time scale of nanoseconds. This assumes that the waves do not disperse appreciably and phase mix with other particles. In reality, the timescales involved are short and the energy modulation might have to be applied before the wave becomes nonlinear and dispersive.

In this technique, the coherent energy spread of the beam increases substantially because while one of the waves is cancelled, the amplitude of the remaining wave is increased. A good technique would be to measure the energy profile created by the density perturbation and then apply an energy modulation that exactly negates the profile. However, this assumes we can measure the energy profile of the beam on an appropriate timescale/resolution which can be a limitation in bigger machines. We therefore discuss another technique for controlling the space-charge effect of perturbations on the beam.

4.2.5 Experimental results of the perturbation-compression scheme:

When the electron beam is injected into the UMER ring without longitudinal focusing, the beam ends expand at a speed of $2C_s$ until the beam fills the ring. This is primarily due to longitudinal space-charge forces, which defocus the beam longitudinally. Hence, in order to contain the beam in the longitudinal direction, appropriate longitudinal electric fields must be applied repeatedly. This is done in UMER presently through the induction cell. Like the beam ends, the perturbation also expands and splits into a fast and a slow wave when the beam is allowed to freely expand. So, by longitudinally compressing the perturbation part of the beam periodically, we can contain the perturbation from splitting into a fast and a slow wave. We show experimental results of the perturbation compression in the following section.

We injected a 23 mA beam with a 10% density perturbation into a ring and applied no longitudinal focusing. This is shown in Figure 4.14 with a dark blue curve. We then applied longitudinal electric field at RC4 with varying strength, to contain or

"compress" the perturbation. We tracked the beam current for each turn in all theses cases at RC10. The results of the experiment are shown for up to 4 turns in Figure 4.14. Every color within a sub-plot shows the beam current for a specific value of compression voltage. As the applied voltage is increased, the waves become closer or in other words, the wave splitting is delayed. Due to the limitation in the apparatus, we applied the longitudinal focusing only for a single turn. Because of the circular layout of UMER, we can in principle apply the same longitudinal focusing field periodically for every turn, and thus "hold" the perturbation without splitting. This technique is very similar to the previously discussed coherent pulse flattening experiment except here we introduce the energy waves at the very beginning before the wave splits. This allows us to delay the perturbation from splitting. We summarize this technique in the next section.

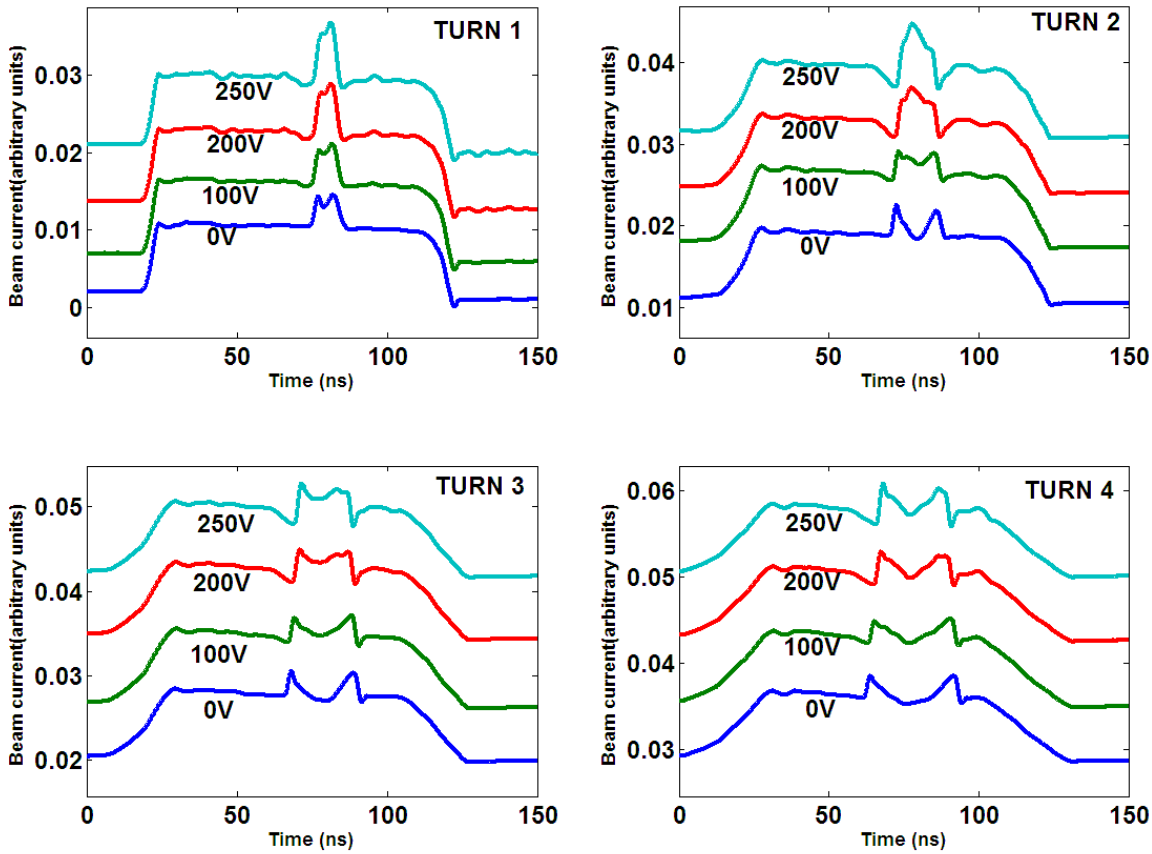

Figure 4.14: Experimental results of perturbation compression for a 23mA beam current with a 10% density perturbation. The sub-graphs show the effect of compression on every turn for different values of electric field strength. The perturbation, when compressed, takes a longer time to evolve into a slow and a fast wave. For the case shown, the perturbation was applied only once in the first turn at RC4.

4.2.6 Perturbation compression scheme:

We start with the observation that it is because of space-charge that the density perturbations are converted into energy modulation, which can then create problems when the beam goes through a bunch compressor. So, we want to prevent the density perturbation from splitting into a fast and a slow wave. We do this by compressing the density perturbation near the gun/injector by applying a linear electric field which prevents the perturbation from splitting. This is similar to ear-

fields applied at the beam ends for longitudinal focusing, but we apply them for the perturbation alone.

Initial experiments in UMER using this approach show that by applying ear-fields to a perturbation, we can control the wave speed. If a density modulation is compressed before it splits into fast and slow waves, we have in effect compensated for the space-charge mechanism. We are then left with a space-charge dominated beam with a density modulation that remains as a single density modulation and does not split into fast and slow waves as long as the compression is applied periodically.

If the beam is now accelerated to relativistic energies, particles within the perturbation are travelling with approximately the same velocity as that of the other particles. The space-charge effects were compensated for at the beginning. So, when such a "space-charge compensated" beam goes through a dispersive section we have no additional density modulation because the effect of dispersion on a beam with uniform energy is same for all particles. There are some limitations in this technique. First, the beam will still have a density bump which could lead to coherent radiation and thus start an energy modulation again. Secondly, it is not clear how does the perturbation evolve under compression and acceleration combined. Future experiments in UMER involving acceleration will give us some clues to understand these limitations.

4.3 Non-linear space charge waves

Previous experiments by using a localized, single density perturbation showed that the wave speed depends on the strength of the perturbation. The higher the

relative strength of the perturbation compared to the main beam, the faster the waves propagate. This is a general property of non-linear wave propagation. We also know from the physics of nonlinear waves that non-linear waves are prone to wave-breaking [58]. Wave-breaking occurs when the crest of the wave travels faster compared to the other part of the wave leading to steepening and eventually breaking. It is a phenomenon most commonly observed in ocean waves. Though the problem of wave-breaking is mathematically involved, we extend the fluid equation presented in the previous chapter to understand some elementary ideas in non-linear wave propagation. The original dispersionless, *linear* equation for the space-charge waves can be written in the form,

$$C_s \frac{\partial \lambda_1}{\partial z} + \frac{\partial \lambda_1}{\partial t} = 0 \tag{4.6}$$

The solution of equation (4.6) can be written as $\lambda_1(z,t) = f(z - C_s t)$ where C_s is the wave velocity and λ_1 is the line-charge density of the perturbation. From experiments, we know that the velocity of the waves is dependent on the amplitude i.e. $C_s = G(\eta\lambda_0) = G(\lambda_1)$, where η is the strength of the perturbation and λ_0 is the line-charge density and let G be a corresponding function between the perturbation strength and the wave speed. Keeping the dispersionless transport assumption but including the *nonlinear* behavior, the solution changes to $\lambda_1(z,t) = f(z - C_s(\lambda_1)t)$. As shown in the appendix A, as the waves of the form $\lambda_1(z,t) = f(z - C_s(\lambda_1)t)$ propagate, they steepen and then break. An intuitive way

to understand this would be to think of the apex of the wave travelling faster than the base of the wave causing the apex to overtake. At this point, the wave curls like a large ocean wave. Now, the wave becomes multi-valued at a certain time due to steepening and we say that the wave breaks.

4.3.1 Experiment showing wave train formation:

We introduced a relatively large perturbation (η=0.5) compared to the main beam to test wave-breaking in space-charge waves. The beam current was 36 mA and the perturbation current was 17.5 mA. For clarity, the perturbation was introduced near the edge so that either the slow wave or the fast wave alone propagates along the whole length of the beam. The turn-by-turn profile of the beam current is shown in Figure 4.15.

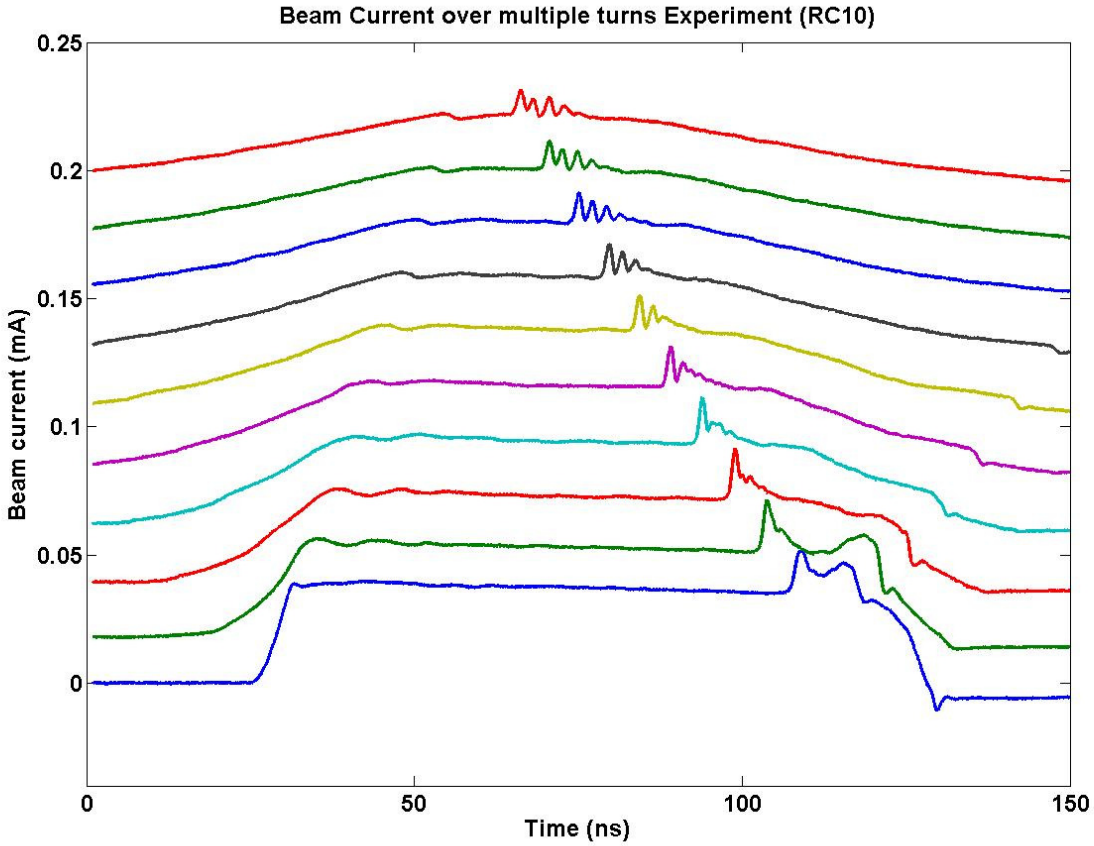

Figure 4.15: Turn-by-turn plot of the beam current (36 mA) with a 17.5 mA perturbation showing wave train formation in the third turn. As the turn increases, the number of waves increases. The perturbation is introduced near the tail of the beam to allow the fast wave to spend a longer time in the flat-top portion of the beam.

As seen from Figure 4.15, the perturbation introduced near the tail splits into a fast and a slow wave. The fast wave propagates along the beam toward the beam head while the slow wave rolls off the edge of the beam tail. The fast wave starts to steepen and then starts to break into sub-pulses after second turn and continues to break in the subsequent turns as well. The distance between each peak is 2 ns (on average). The plasma frequency of the beam is approximately 400 MHz confirming that the sub-pulses oscillate close to the plasma frequency. We show in the next few sections that these sub-pulses are due to the excitation of non-linear waves and wavebreaking.

4.3.2 KdV equation, Burgers equation and Dawson limit:

We take a simplified approach to present how an initial perturbation can become steep and break [59]. We begin with eqn (1.20) discussed in Chapter 1. Let the initial condition be expressed as

$$\lambda(z, t=0) = \lambda_0(\xi)$$

where λ is the line charge density. We do a change of variable as $\xi = z - \lambda t$.

Now, we take the temporal and the spatial derivatives to get,

$$\begin{aligned}
\frac{\partial \lambda}{\partial t} &= \frac{\partial \lambda_0}{\partial \xi}\left(\frac{\partial \xi}{\partial t} + \frac{\partial \xi}{\partial \lambda}\frac{\partial \lambda}{\partial t}\right) \\
&\Rightarrow \frac{\partial \lambda}{\partial t}\left[1 + t\frac{\partial \lambda_0}{\partial \xi}\right] = -\lambda\frac{\partial \lambda_0}{\partial \xi} \qquad (4.7) \\
\frac{\partial \lambda}{\partial z} &= \frac{\partial \lambda_0}{\partial \xi}\left(\frac{\partial \xi}{\partial z} + \frac{\partial \xi}{\partial \lambda}\frac{\partial \lambda}{\partial z}\right) \\
&\Rightarrow \frac{\partial \lambda}{\partial z}\left[1 + t\frac{\partial \lambda_0}{\partial \xi}\right] = \frac{\partial \lambda_0}{\partial \xi}
\end{aligned}$$

Combining the two parts of equation (4.7) into equation, we get the following condition

$$\left(1 + t\frac{\partial \lambda_0}{\partial \xi}\right)\left(\frac{\partial \lambda}{\partial t} + \lambda\frac{\partial \lambda}{\partial z}\right) = 0 \qquad (4.8)$$

So if,

$$\left(1 + t\frac{\partial \lambda_0}{\partial \xi}\right) \neq 0, \qquad (4.9)$$

then $\lambda(z - \lambda t)$ is a solution to the Burgers equation.

Let us take a concrete example to demonstrate that the Burgers equation with a smooth initial profile can lead to wave steepening and then wave breaking over

time. Let $\lambda_0(z) = \cos(\pi z); \lambda_1(z,t) = \cos(\pi(z - \lambda t))$, then according to equation (4.9) we get,

$$t \neq \frac{1}{\pi \sin(\pi z)} \tag{4.10}$$

This equation is satisfied for all $t < \frac{1}{\pi} = t_B$, where t_B is the breaking time. So, until $t < t_B$, the wave just propagates and steepens. But at $t = t_B$, the initial perturbation becomes steep and breaks.

The summary of the previous discussion is that we have shown that once the 1-D cold fluid theory is reduced to KdV equation, the KdV equation can then be simplified into the inviscid Burgers equation to explain the observation of wave breaking at large amplitude perturbation. We conclude this section by applying equation (4.9) to a parabolic shaped perturbation of the form: $\lambda_0(z) = \rho_{L0}(1 - z^2/z_m^2)$, where ρ_{L0} is the peak line-charge density (amplitude) of the perturbation and z_m is the maximum length of the pulse. Differentiating with respect to z and substituting we get the breaking time to be,

$$t_B \propto \frac{z_m}{2\rho_{L0}} \Rightarrow \rho_{L0} t_B = \text{constant} \tag{4.11}$$

This implies that for a perturbation of given width (5ns in our case) a larger line-charge density perturbation can cause the wavebreaking to occur sooner than with a lower charge density one. This behavior is observed regularly in UMER beam perturbation experiments. In the non-linear regime, a larger perturbation causes the

space charge waves to break earlier compared to a perturbation with relatively smaller amplitude. The phenomenon of wavebreaking was first predicted in cold plasmas by Dawson [60] and has been demonstrated to accelerate particles [61]. Even nonlinear longitudinal plasma oscillations are harmonic with the plasma frequency [62] , as can be seen from Figure 4.15.

We note that we have ignored dispersion in all our calculation in trying to explain wavebreaking. Dispersion can become a critical factor, once the wave steepens. For example, when the wave breaks, the pulse width of the secondary waves are of the order of 2ns, which is 11.5cm long while the pipe diameter is 5.08 cm. When the ratio of the pipe diameter to the beam length becomes comparable, dispersion effect must also be included [31, 36].

4. 4 Summary:

In this chapter we have experimentally shown how multiple perturbations propagate in a space-charge dominated beam. Space-charge waves behave like linear waves and so superpose and cross each other. We applied this principle to demonstrate the cancellation of a space charge wave through energy modulation. We also showed that by compressing the perturbation at the start we can prevent the perturbation from splitting into a fast and slow wave. Finally, we showed that when there is a large perturbation, space-charge waves behave like non-linear waves and can undergo wavebreaking.

Chapter 5: Longitudinal perturbations due to space charge effects in the gun

Up until now, we have discussed the effects of space charge on perturbations over a long distance under different initial conditions. In this chapter, we focus on studying space charge effects near the gun. We begin with the experimental observation of pulse splitting near the gun at higher laser power. Then we briefly discuss the 1-D virtual cathode theory (VC) and short-pulse Child-Langmuir limit (short pulse space-charge limit) to explain the sub-pulse formation. We conclude this chapter by discussing the relevance of such short pulse effects for photoinjectors.

5.1 Pulse splitting near the gun

In UMER, it is possible to photoemit a short electron beam pulse using a laser, without any thermionic emission. Under such conditions, the beam current profile follows the laser profile up to a critical value of laser power. Above the critical value, the beam pulse starts splitting into multiple sub-pulses within the gun as shown in Figure 5.1.

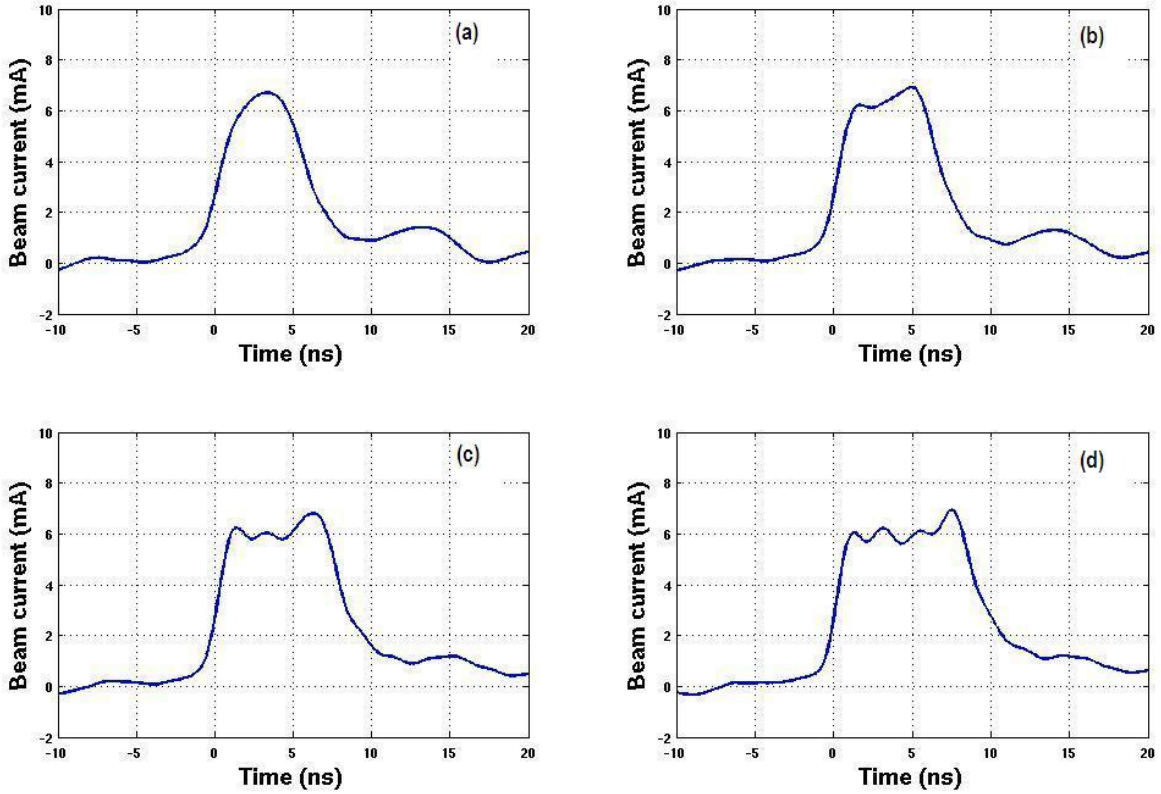

Figure 5.1: Single perturbation pulse splitting into multiple sub-pulses at (a) Laser generated electron beam (b) Pulse splitting into two sub-pulses (0.68mJ) (c) Three sub-pulses (1.3mJ) (d) Four sub-pulses observed at (2.7mJ). This measurement is taken at the Bergoz (placed 64 cm from the anode exit) in the injection line.

Similar effects have been observed before in high current RF photoinjectors and other low energy electron guns [28, 29, 42]. We compare our observations with those theories and discuss the relevance of such effects for future photoinjectors. This effect is likely due to the formation of a virtual cathode. A virtual cathode is formed when the total injected current in the cathode exceeds the space charge limit of the gun. We discuss the 1-D virtual cathode theory in the following section.

5.2 Time-independent diode behavior

The space-charge fields inside a diode can become large to form a virtual cathode. In order to explain the formation of virtual cathode, we do a simple DC analysis of the diode under the absence of the applied field. This problem is well-known and is treated in several papers on vacuum tubes [63, 64].

Our goal in this section is to perform a DC analysis of a 1-D diode to see how and at what critical input current to a diode does the virtual cathode forms. We follow Birdsall and Bridges[65] in the subsequent derivation.

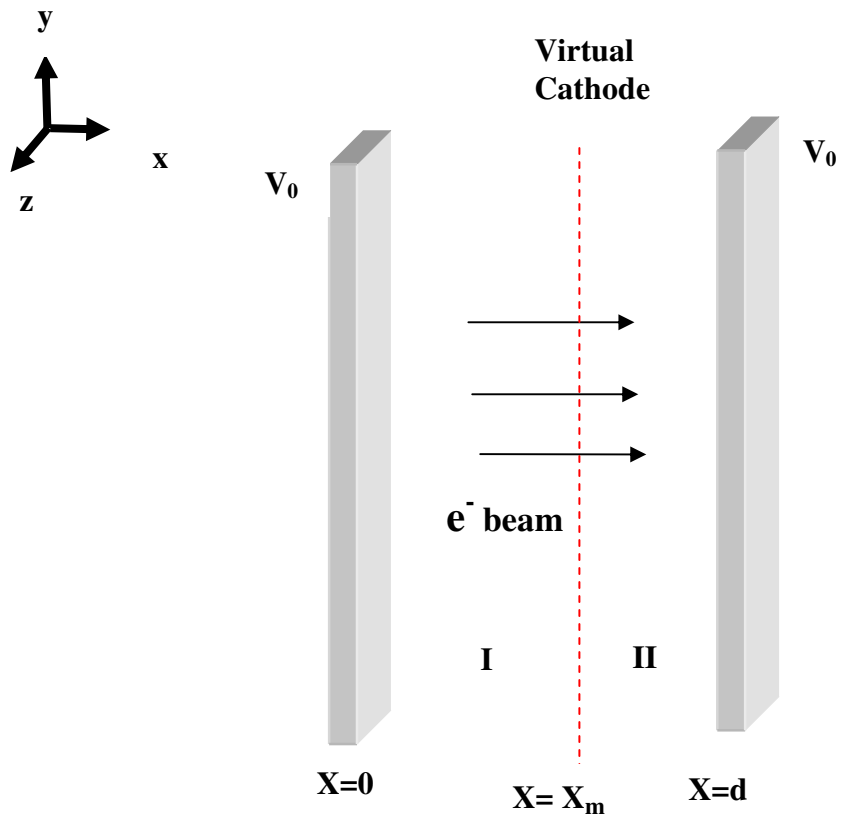

Figure 5.2: A short-circuited diode showing the virtual cathode and the electron beam direction. The virtual cathode separated the gap into Region I and Region II.

Let us assume two infinite (in y and z) parallel plates held at potential V_0 and separated by a distance d. This is shown in Figure 5.2. By writing the Poisson equation and continuity equation, and simplifying the equations give,

$$\left(\frac{dV}{dz}\right)^2 = \frac{4J_0}{\varepsilon_0(-2e/m)^{1/2}}\left(V^{1/2} - V_m^{1/2}\right), \tag{5.1}$$

where V_m is a constant of integration. V_m is the minimum potential inside the space between the cathode and the anode. In order to proceed from here, we have to solve the above equation for two boundary conditions. They are (i) $V_m > 0$ and (ii) $V_m = 0$.

(i) $\underline{V_m > 0}$:

The parameter α is defined as the following:

$$\alpha = \frac{J_0}{-2.33\times10^{-6}V_0^{1/2}d^{-2}} \tag{5.2}$$

When $\alpha = 1$, we simply get the Child-Langmuir limit. The solution of these equations for Vm >0 are reported elsewhere [65]. We used MATLAB to plot the potential minimum as a function of the input current α as shown in Figure 5.3.

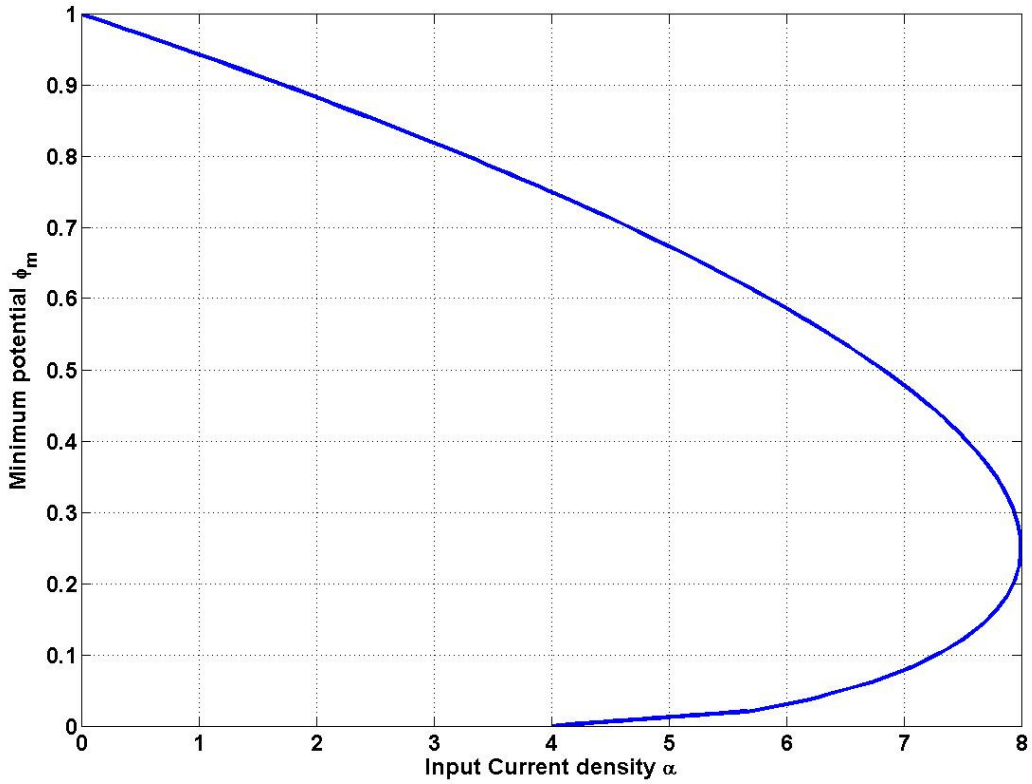

Figure 5.3: The plot shows the value of the normalized potential minimum as a function of the input current density. When the input current density exceeds 8, the potential minimum starts to reduce and then vanishes.

We also plot potential minimum as a function of distance for a few values of the input current. This is shown in Figure 5.4.

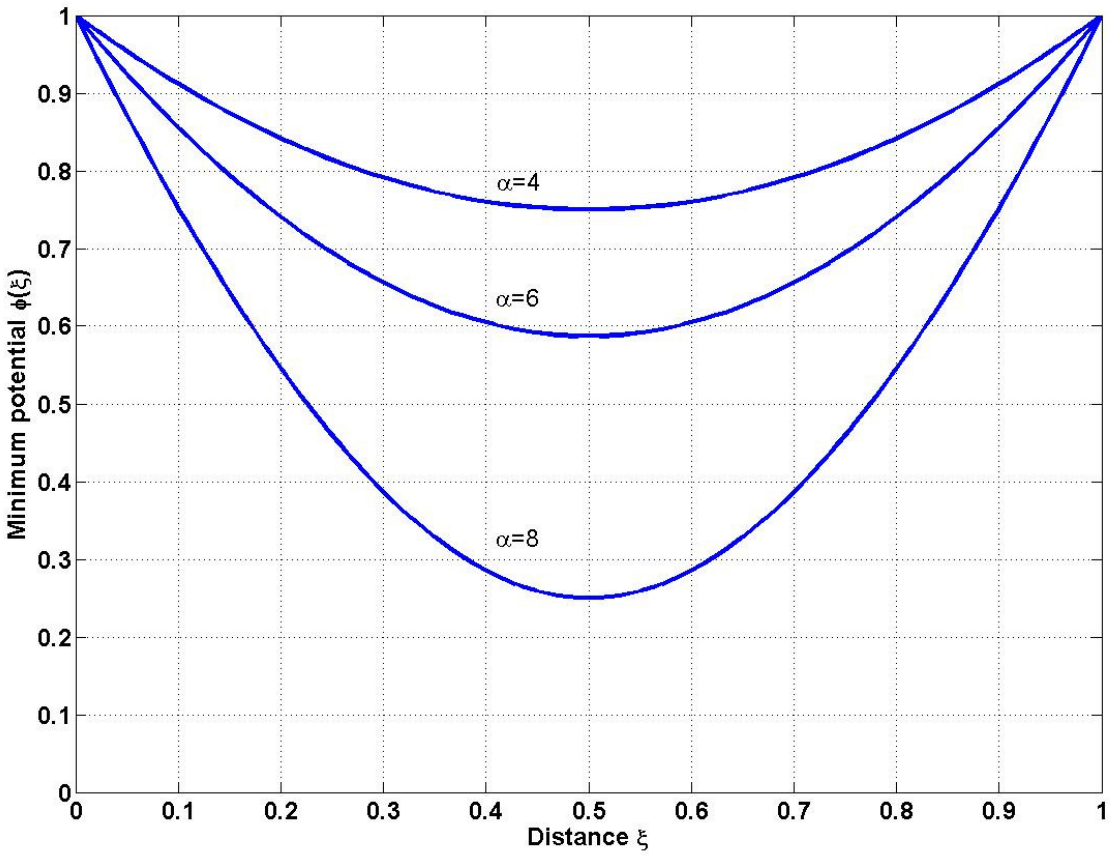

Figure 5.4: The plot shows the potential profile inside a diode as a function of distance and the input current density. As the input current density increases, the potential profile sags until it vanishes when α >8.

From these plots, we can conclude that between $0<\alpha<8$, the potential minimum is symmetric about the center. For $\alpha>8$, V_m approaches zero, causing reflection of charges towards the cathode. At this point, the potential minimum becomes a virtual cathode. At the virtual cathode, both the potential and the electric field are zero, while at a potential minimum only the electric field is zero.

Now we solve the equation (5.1) *after* the virtual cathode is formed. i.e. $V_m=0$.

(ii) V_m =0:

When V_m =0, some of the electrons will be transmitted through the virtual cathode while others will be reflected back toward the cathode. Hence though the velocity of the electrons may change, the net current will remain unchanged. Let us assume that a fraction *f* of the injection current is transmitted and (1-*f*) is reflected. We can write,

$$\rho_I = \frac{J_0}{v} + \frac{-(1-f)J_0}{-v} = \frac{(2-f)J_0}{v}$$
$$\rho_{II} = \frac{fJ_0}{v}, \tag{5.3}$$

where I and II refers to the regions before ($0< x< x_m$) and after ($x_m < x< d$) the virtual cathode respectively. This is shown by a red dotted line in Figure 5.2. Figure 5.6 plots the fraction of the input current that is transmitted as a function of the input current.

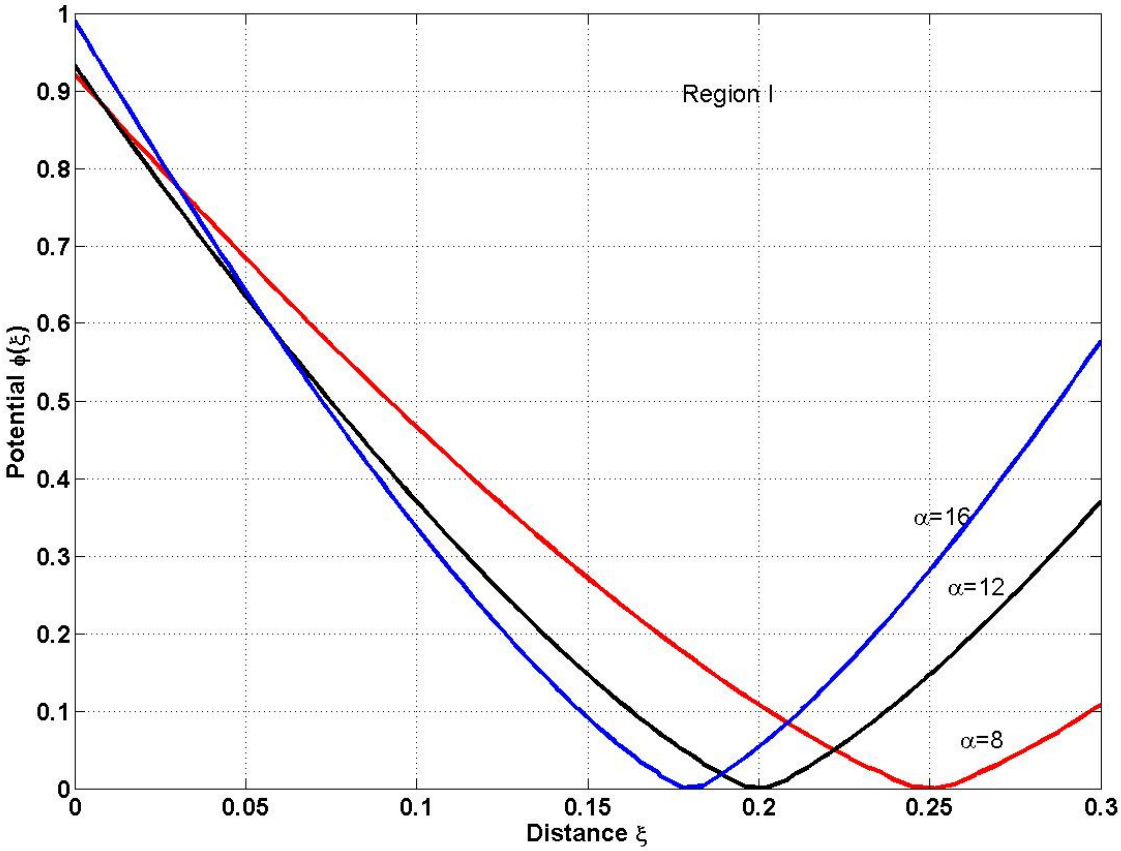

Figure 5.5: The plot shows the variation of the potential profile in the region before the virtual cathode (Region I). After the virtual cathode is formed, increasing the injected current moves the virtual cathode closer toward the cathode causing the output current to follow the Child-Langmuir limit.

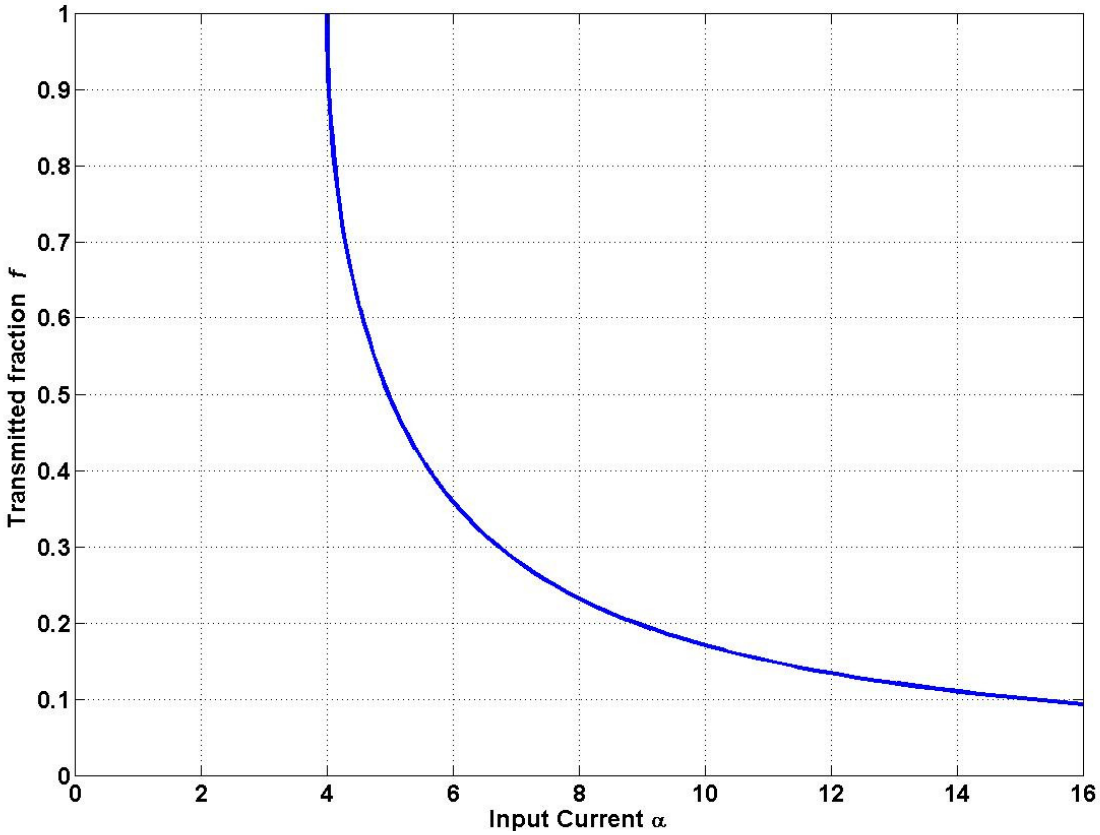

Figure 5.6: The plot shows the transmitted current as a function of input current after the virtual cathode is formed. Once the virtual cathode is formed, complete transmission occurs only when the value of input current (α) is reduced to 4.

The minimum value of α for which all the current is transmitted without reflection is α=4. When α>4, the virtual cathode moves towards the cathode and for large values of α, the ξ_m=0 and we get the Child-Langmuir limit. This is shown in Figure 5.5 for some potential profiles as a function of the input current α.

So, to summarize, we have the range of currents 4< α<∞ for V_m=0 and the range 0<α<8 for V_m >0. Both of these solutions can cover the entire range of input currents. Next, we will see how the classical behavior of the diode can be explained using these two solutions. Figure 5.7 shows the transmitted current as a function of the input injected current.

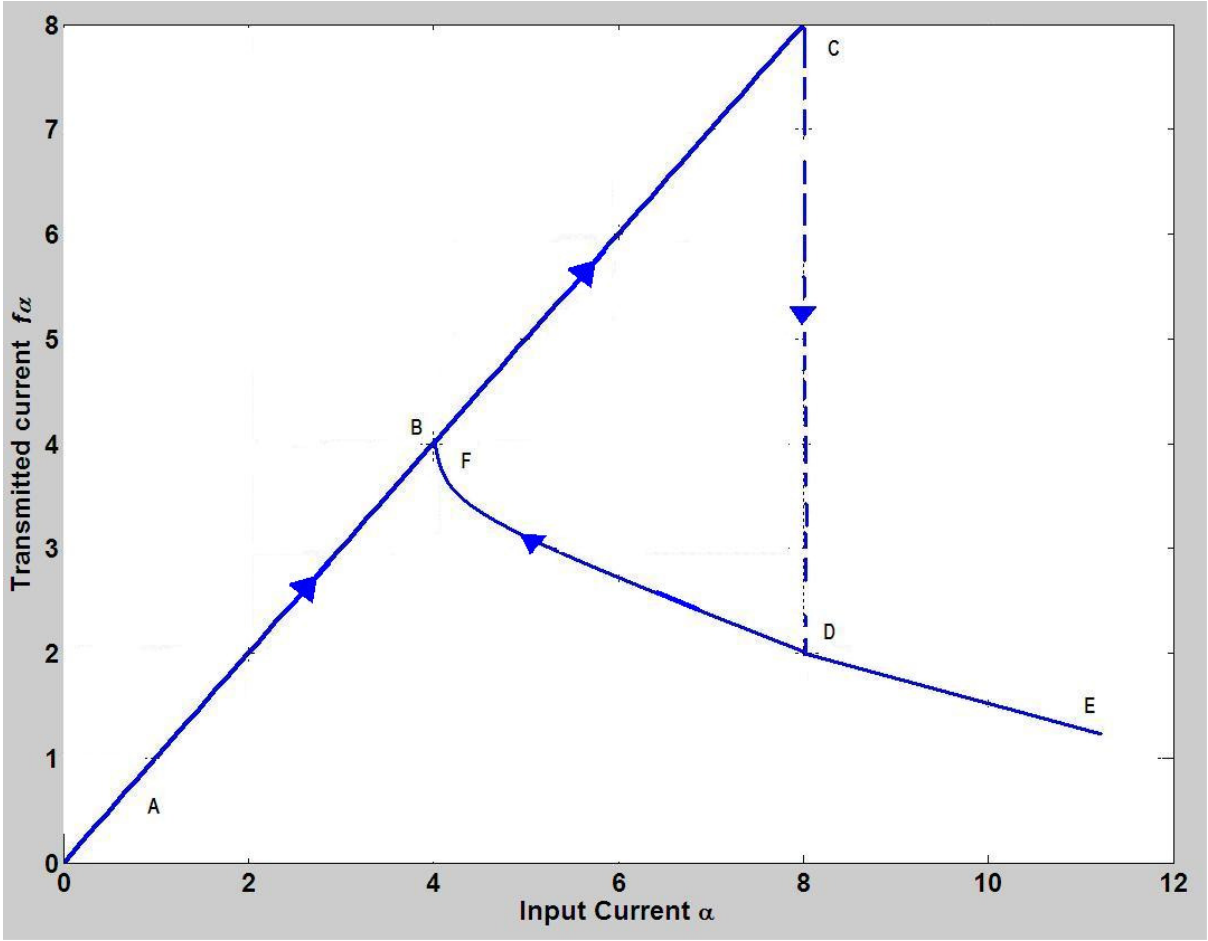

Figure 5.7: The diode output current as a function of the input current. The output current follows the input current up to a critical value of the input current after which there is a sudden drop in the output. The path CD constitutes the virtual cathode formation.

As α is increased from 0 to 8, there is complete transmission of the injected current shown by the points A, B and C. If the input current is increased beyond α>8, there is a drop in the transmitted current to the point D. Any further increase in the input current causes the transmitted current to decrease and it asymptotically reaches the Child-Langmuir limit (point E). Now, if we then decrease the input current, the transmitted current increases through the point (E, D and F). After reaching the point F, it follows the original curve through B and C. Note that, though

the point B and F are transmitting the same current, the point F has a virtual cathode in the potential profile while point B doesn't. (Refer Figure 5.5).

The jump from the point C to point D cannot be captured by the classical DC analysis. We have to do a transient analysis to understand the changes in the diode region between those points. Since a complete AC analysis is beyond the scope of this work, we refer time-dependent analysis to works by Birdsall and Bridges[65] and references therein.

5.3 Potential minimum oscillation

When the current diode is increased beyond the α=8, a steady oscillatory solution is found for both the value and the position of the potential minimum [66, 67]. A schematic of this behavior is shown in Figure 5.8.

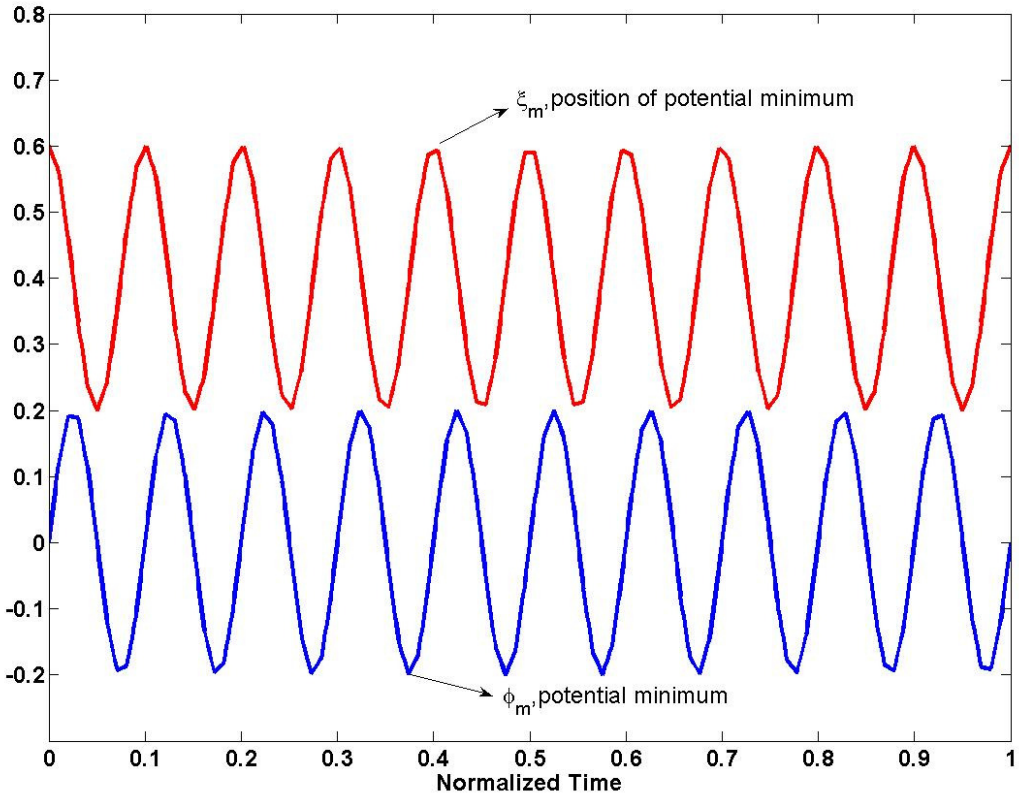

Figure 5.8: The plot shows that the virtual cathode after it forms is not stable. It oscillates in position as well as in amplitude. The blue curve plots the value of the normalized potential minimum and the red curve plots the normalized position of the potential minimum.

Figure 5.8 shows that not only does the value of the potential minimum oscillates but the position oscillates as well. This means that the number of electrons crossing the virtual cathode to reach the anode will also vary with respect to time. This cycle can be explained as follows: Initially, all the electrons injected from the cathode reach the anode. Once the charge density becomes high inside the diode, a virtual cathode is formed. When a virtual cathode is formed, some of the electrons get reflected back to the cathode while others pass through the virtual cathode to the anode. Due to this reflection, the number of electrons near the virtual cathode decreases, causing the potential to increase and hence the potential minimum shifts

again. This causes more electrons to pass through the virtual cathode and the cycle repeats again. In our experiment, the laser creates a virtual cathode inside the diode causing the sub-pulses to form. Since, the virtual cathode formation depends on the electron density which increases with laser power, the larger the laser power, the greater the number of sub-pulse formation.

We have discussed why the virtual cathode forms when the Child-Langmuir limit is exceeded. Now, we will look into how we can exceed the Child-Langmuir limit when the pulse duration is short compared to the transit time in the diode.

5.4 Classical Short – Pulse Child-Langmuir Law (SCL)

We follow Valfells [28] to derive the short-pulse Child-Langmuir limit using a single sheet model. A much more accurate approximation is the equivalent diode approximation which was also done by Valfells [28]. We assume a planar 1D diode with a transit time of T_{CL} in the Child-Langmuir limit.

Single Sheet Model

In this model, we treat the electron pulse as a sheet of charge with charge density σ. When there are no electrons in the gap, the electric field in the gap is $\frac{V_g}{D}$, where Vg is the gap voltage and D is the separation of the electrodes. Once the sheet is injected, the electric field changes by $\Delta E = \frac{\sigma}{\varepsilon_0}$ and at the virtual cathode, the effective electric field becomes zero. So, at the virtual cathode, the charge density is $\sigma = \frac{\varepsilon_0 V_g}{D}$. Since we are treating the pulse as a single sheet of charge, we can write

$\sigma = J\tau_p$, where J is the injection current density and τ_p is the pulse length. An important condition in this is that the pulse length is short compared to the transit-time i.e. τ_p < $T_{CL.}$ So, combining these equations, we can write J_{SCL} the maximum current density in the short-pulse limit, before the virtual cathode is formed as:

$$\mathbf{J}_{\mathrm{SCL}} = \frac{\varepsilon_0 V_g}{D\tau_p} \tag{5.4}$$

From the classical Child-Langmuir law we know that,

$$J_{CL} = \frac{4\varepsilon_0}{9}\sqrt{\frac{2e}{m}}\left(\frac{V_g^{3/2}}{D^2}\right)$$
$$T_{CL} = 3D/\sqrt{2eV_g/m} \tag{5.5}$$

So, eqn (5.4) can be rewritten as,

$$J_{SCL} = \frac{3J_{CL}}{4X_{CL}}, \tag{5.6}$$

where $X_{CL} = \frac{\tau_p}{T_{CL}}$ is the ratio of the beam pulse duration to the transit time of the 1-D planar diode in the Child-Langmuir limit. Equation (5.6) indicates that when X_{CL} <<1, the current density (J_{SCL}) can exceed the 1-D Child-Langmuir limit J_{CL}.

We note that the planar 1-D Child-Langmuir was extended to 2-D by Lunginsland [68] using PIC simulation and shown to be monotonically decreasing function of W/D where W is the width of the emitting strip and D is the gap separation according to, $J_{2D} = \left(1 + \frac{C}{W/D}\right) J_{CL}$, where C is a constant depending on the shape of the emitter and W is the characteristic length of the emitter. Valfells

experimentally estimated the dependence of the current density on the emitter area to be $J_{crit} \propto \frac{1}{R^{-1.8}}$. From both Valfells' estimation and the single-sheet model, we can conclude that the total charge emitted (without virtual cathode formation) is weakly dependent on the pulse-length and depends on the charge-density of the emitter material and the surface electric field. i.e., $Q = J\tau_p = \sigma E$. From (5.6) we can write the total charge in the short-pulse limit as a function of the total charge in the Child-Langmuir limit as

$$Q_{SCL} = \frac{3Q_{CL}}{4}, \tag{5.7}$$

where Q_{CL} is the charge emitted in the Child-Langmuir limit and Q_{SCL} is the charge emitted in the short-pulse limit before virtual cathode formation.

In summary, in the short-pulse limit with no virtual cathode formation, the current density can exceed the Child-Langmuir limit, but we cannot exceed the limit on total charge in the pulse. Therefore, future photoinjectors where $X_{CL} << 1$ should be operated with bunch charges well below Q_{SCL} to prevent virtual cathode oscillations on the electron beam.

5.5 Explanation for the experimental observations

In this section, we explain the observation of pulse splitting in the UMER gun. The laser generated electron beam has a rise time of 1 ns which is comparable to the 0.75 ns transit time of the anode-cathode gap under the Child-Langmuir limit in UMER. When the laser is switched on, the measured value of charge extracted from the gun before the splitting (the critical point) is, $Q_{crit} = I_{peak} T_{FWHM} = 56\,pC$, where I_{peak} and T_{FWHM} are the peak beam current and FWHM (Full Width Half-Maximum) of the beam pulse obtained from Figure 5.1. Q_{crit} is the value of charge extracted before the pulse splits further.

The maximum current density when the UMER gun is in the Child-Langmuir limit is $J_{CL} = 3.73\,{}^{kA}/_{m^2}$. The corresponding charge $Q_{CL} = J_{CL}\pi r_{laser}^2 t_{laser} = 84.4\,pC$, where t_{laser} = 5 ns is the FWHM of the laser and r_{laser} =1.2 mm is the laser spot radius The ratio of $\frac{Q_{crit}}{Q_{CL}} = 0.66$. From theory, at very short pulse-duration injection, the maximum charge that can be obtained before the onset of virtual cathode oscillations is $\frac{Q_{crit}}{Q_{\max}} = 0.75$, which is in good agreement with the measured value of 0.66.

The oscillation frequency of the virtual cathode is expressed in terms of a planar diode peak current density as $f(GHz) = 10.2\sqrt{\frac{J({}^{kA}/_{cm^2})}{\beta\gamma}}$ [69]. For a 10 keV electron beam in UMER ($\beta\gamma$=0.2) with a photo-emitted beam current of 7 mA and a radius of 1.2 mm, $t_{split} = \frac{1}{f}$, where t_{split} is the time period of the virtual cathode oscillation. The time period for a 7 mA beam of radius 1.2 mm

is in agreement with the observed experimental value of 2.5 ns. Since $\beta\gamma$ is varying inside the gun, the value of $\beta\gamma = 0.1$ is taken for calculating the frequency of oscillation.

The above experiment indicates that though it is possible to extract more current from a cathode using a short pulse, there is a critical current density above which the pulse starts to develop unwanted temporal structure on it. Thus, it is important to operate below the critical current density in a short-pulse injection scenario.

5.6 Extending the results for a high gradient photoinjector

In the case of photoinjectors, which remain the primary choice for electron sources for next generation machines, it is important to consider effects introduced due to transient behavior owing to the very short pulse length compared to the anode-cathode gap.

Let us take an example of a high-gradient gun (e.g. LCLS gun [9]) and calculate the maximum charge the gun can handle: $Q_{\max} = \frac{E_{\max}}{\varepsilon_0 A}$, where A is the cathode emission area with $E_{\max}$ = 120 MV/m. Let the emission radius be 1.2mm, so $Q_{\max} = 4.8nC$. This is the maximum charge that can be extracted from the cathode. For the beam inside the RF-cell, γ_f = 6 for 2.5 MeV and E_A=60 MV/m. Assuming a 10ps laser pulse, the transit time $T = \frac{mc\gamma_f}{eE_A}\sqrt{1-\frac{1}{\gamma_f^2}} = 0.16\,ns$, where γ_f is the

relativistic factor at the gun exit and E_A is the average applied field. The transit time is much longer than the 10ps. Hence, short pulse effects are important in such a gun.

From 1-D virtual cathode theory, at very short pulse-length injection, the maximum charge that can be obtained before the onset of cathode oscillations is $Q_{crit} = 0.75 Q_{\max} = 3.6nC$, which is much less than the maximum obtainable value of 4.8 nC. A typical gun (e.g. LCLS gun) uses a Cu cathode with a 255nm laser at $500\,\mu J$ and a pulse length of 10 ps. So, $I(A) = \dfrac{\lambda(nm) Power(W) QE(\%)}{124} = 108.2\,\mathrm{A}$ which amounts to a charge of 1 nC, which is well below the critical value. This is a good limit to operate for a generating a high quality beam. Any efforts to operate the gun at a much higher charge should then take the space charge effects into consideration.

5.7 Limitation of the theory

There are some limitations in the above derivation of the single sheet theory. Firstly, it ignores the transverse effects such as beam size, which depends on the critical current density and hence on the total charge. When the beam does not fill the diode region, the beam is all-ends and it is essential to take into account the complete 3-D effects inside the gun to calculate the charge limit. Secondly, our calculations for the high-gradient gun overlooked acceleration that occurs inside the gun. Acceleration reduces the effects of space-charge. So, a 3-D simulation taking both space charge and acceleration into account will give a better understanding of the physics near the gun.

5.8 Conclusion

In summary, we have seen how space charge effects in the gun can lead to undesirable modulation on the beam pulse through space charge. The self-fields of a bright beam can initiate density modulations as well as energy modulations by splitting the beam pulse. In the case of modern photoinjector generating bright and ultra-short beams, the critical current density for such effects to start is much lower than the maximum current density achievable. Hence to prevent such behavior and maintain beam quality, the gun should be operated well below the space charge limit. This also indicates that there might be a space-charge imposed limit to the beam brightness that can be obtained from photoinjectors.

Chapter 6: Conclusion and Future work

In this chapter, we summarize the dissertation work and conclude by suggesting some ideas for possible future work.

6.1 Summary and Conclusion

We started by using photoemission from a laser to produce a controlled, localized density perturbation on an intense beam. We showed that the density perturbation evolves as fast and slow space charge waves. We then calculated the wave speed for different beam currents at different perturbation strengths. We showed that we have good agreement with both the 1-D theory and PIC simulation (WARP) in the linear regime. We then proceeded to investigate experimentally the effect of multiple perturbations on a beam. We did this by adding another laser to generate a density perturbation. We found that multiple perturbations behave just like linear waves – superposing and crossing each other. We exploited this property to control a density modulation by applying an energy modulation to cancel either the fast or the slow wave, thus showing that modulations can be controlled.

In the non-linear regime, where the strength of the perturbation is large (>25% compared to the beam current), we observed wave breaking of the fast and slow waves. We also showed that linear space-charge waves can be used as non-interceptive transverse beam diagnostics in UMER. We did a time-sliced imaging of the perturbation and showed that a density perturbation can become an energy modulation and, through dispersion, affect the beam centroid.

Finally, we explained the observation of multiple sub-pulse formation near the cathode above a critical value. We extended the analysis for a high-gradient gun to

show that there might be a practical limit on beam brightness that can be obtained from photoinjectors determined by space-charge.

From this work, we conclude that density modulation on an intense beam can produce fast and slow waves, which can be controlled through energy modulation in the linear regime. Moreover, a large amplitude density modulation, when allowed to propagate, can break into sub-pulses, causing energy modulation. Hence, a density modulation should not be allowed to grow and must be controlled at the very beginning. Such effects can also occur near the gun, where high space charge can break a density modulation into multiple sub-pulses. This can be prevented by operating the gun below the space-charge limit.

6.2 Suggestion for future work

This dissertation focused on the effect of a density perturbation on a coasting beam without any longitudinal focusing. This work can be extended in three possible ways: long distance experiments, short-pulse experiments and parabolic pulse transport.

In the long distance experiments, the first step would be to investigate the effects of a perturbation with the longitudinal focusing turned on. This will answer the question on what happens to the fast and slow waves as they reach the beam ends. Secondly, while this thesis demonstrated cancellation of either a fast or a slow wave, by adding one more induction module in UMER it should be possible to cancel both the fast and the slow wave. Moreover, by loading the induction gaps, the effect of impedances on the waves can be studied.

In addition, there are still unresolved issues in the evolution of a large perturbation due to non-linear behavior. In the large amplitude limit, PIC simulation of pulse train formation in the non-linear regime should be investigated. Understanding the dispersive behavior of the space charge waves can give clues about the collective effects in a space-charge dominated beam. Also, extending the 1-D cold fluid theory to include large amplitude perturbation will answer some unresolved issues in the large amplitude limit to get better agreement between experiment and theory. By varying the wave speed such as by beam acceleration or beam compression, further understanding might be achieved about the wave breaking phenomenon. The velocity space of a density perturbation can be measured by installing an energy analyzer in UMER.

In the short-pulse limit, the effect of transverse beam size on the critical current density needed to start virtual cathode oscillations can be studied. This can be done by focusing the laser beam to different spot sizes and measuring the critical current density that triggers virtual cathode oscillations.

A rich set of experiments can be done by using the 5-ns, parabolic beam pulse generated by photoemission from the laser. Since such a beam is "all ends", without any flat-top, it is realistic and is similar to the ultra-short beams generated in modern accelerators. Thus, studying the evolution of a space-charge dominated parabolic pulse with focusing and compression is of direct relevance to other machines.

Appendix- A

In this appendix, we show that equation of the form $\frac{\partial u}{\partial t} + c(u)\frac{\partial u}{\partial x} = 0$ with the initial form $u_0(x) = u(x,0) = f(x)$ and the solution $u(x,t) = f(x - c(u)t)$ is prone to wave breaking using a simple example of a triangular wave. The piecewise linear initial data (a triangle) is shown in the figure below can be expressed as:

$$f(x) = \begin{cases} u_0 x & 0 < x < 1 \\ u_0(2-x) & 1 < x < 2 \\ 0 & x \le 0; x \ge 2 \end{cases}$$

By changing the frame of reference, by substituting $\theta = x - t$ we get:

$$u(\theta,t) = \begin{cases} u_0(\theta\text{-}ut) & 0 < \theta - ut < 1 \\ u_0(2-\theta+ut) & 1 < \theta - ut < 2 \\ 0 & x \le 0; x \ge 2 \end{cases}$$

Now, we have an equation which is intrinsic in u, which can be solved to obtain:

$$u(\theta,t) = \begin{cases} \frac{u_0\theta}{1+u_0 t} & 0 < \theta - ut < 1 \\ \frac{u_0(2-\theta)}{1-u_0 t} & 1 < \theta - ut < 2 \\ 0 & x \le 0; x \ge 2 \end{cases}$$

We differentiate the above equation with respect to θ and calculate the gradient of the wave as time progresses as:

$$\frac{\partial u}{\partial \theta}=\begin{cases}\dfrac{u_0}{1+u_0 t} & 0<\theta-ut<1\\ \dfrac{-u_0}{1-u_0 t} & 1<\theta-ut<2\\ 0 & x\le 0; x\ge 2\end{cases}$$

The gradient of the right side of the triangle (the part of the wave between ($1<\theta-ut<2$) changes from negative to positive i.e. it becomes vertical at $t=1/u_0$. The gradient of left side of the triangle slowly decreases over time. This is illustrated by the following diagrams.

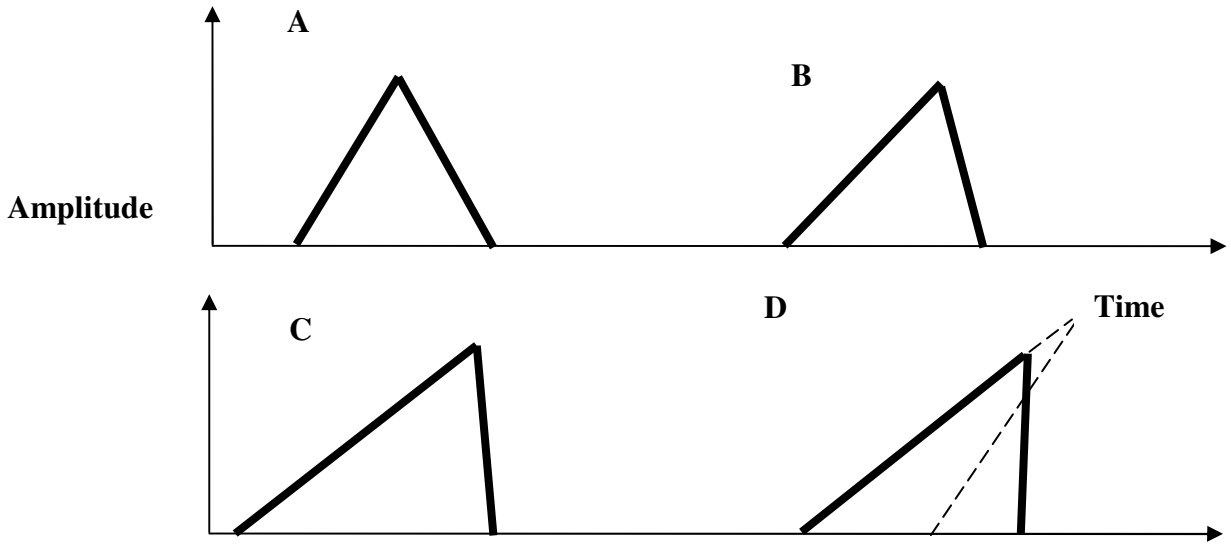

Illustrating the wavebreaking of a triangular waveform through nonlinear steepening. The x-axis is time and y-axis is amplitude. The plot shows at various time (A,B,C,D), how the apex of the wave overtakes the base of the wave and lead to steepening. The dotted line is what happens if the steepening continues without breaking

Bibliography

[1] H. Wabnitz *et al.*, Nature **420**, 482 (2002).
[2] P. G. O'Shea, and H. P. Freund, Science **292**, 1853 (2001).
[3] AckermannW *et al.*, Nat Photon **1**, 336 (2007).
[4] H. N. Chapman *et al.*, Nat Phys **2**, 839 (2006).
[5] J. E. Clendenin, and others, AIP Conf. Proc. **915**, 1067 (2007).
[6] L. Merminga, in Particle Accelerator Conference, 2007. PAC. IEEE2007), pp. 22.
[7] T. Shaftan, and Z. Huang, Physical Review Special Topics - Accelerators and Beams **7**, 080702 (2004).
[8] Z. Huang *et al.*, Physical Review Special Topics - Accelerators and Beams **7**, 074401 (2004).
[9] R. Akre *et al.*, Physical Review Special Topics - Accelerators and Beams **11**, 030703 (2008).
[10] C. J. Bocchetta, ICFA Beam Dyn. Newslett. **42**, 58 (2007).
[11] H. Loos, and others, in 30th International Free Electron Laser Conference (FEL 2008),Gyeongju,Korea, 2008).
[12] C. M. Celata *et al.*, Physics of Plasmas **10**, 2064 (2003).
[13] D. Callahan *et al.*, Journal of Applied Physics **81**, 3398 (1997).
[14] J. Wang, and M. Reiser, Physics of Plasmas **5**, 2064 (1998).
[15] J. G. Wang *et al.*, Physical Review Letters **72**, 2029 (1994).
[16] J. Wang, D. Wang, and M. Reiser, Physical Review Letters **71**, 1836 (1993).
[17] J. Wang *et al.*, Physical Review Letters **74**, 3153 (1995).
[18] H. Suk *et al.*, Journal of Applied Physics **86**, 1699 (1999).
[19] Y. Zou *et al.*, Physical Review Letters **84**, 5138 (2000).
[20] H. Suk, J. G. Wang, and M. Reiser, Physics of Plasmas **3**, 669 (1996).
[21] J. G. Neumann *et al.*, Journal of Applied Physics **105**, 053304 (2009).
[22] Y. Huo, in *Electrical and Computer Engineering* (University of Maryland College Park, 2004).
[23] J. Harris, in *Electrical and Computer Engineering* (University of Maryland College Park, 2005).
[24] J. G. Neumann *et al.*, Review of Scientific Instruments **76**, 033303 (2005).
[25] K. Tian, in *Department of Electrical and Computer Engineering* (University of Maryland, College Park, 2008).
[26] M. Reiser *et al.*, Fusion Engineering and Design **32/33**, 293 (1996).
[27] P. O'Shea *et al.*, Nuclear Inst. and Methods in Physics Research, A **464**, 646 (2001).
[28] Valfells *et al.*, Physics of Plasmas **9**, 2377 (2002).
[29] D. Dowell *et al.*, Physics of Plasmas **4**, 3369 (1997).
[30] B. Beaudoin, in *Electrical and Computer Engineering* (University of Maryland, College Park, 2008).
[31] M. Reiser, *Theory and Design of Charged Particle Beams* (WILEY-VCH Verlag GmbH & Co. KGaA, Weinheim, 2008).
[32] V. K. Neil, and A. M. Sessler, Review of Scientific Instruments **36**, 429 (1965).

[33] J. Wu, Z. Huang, and P. Emma, Physical Review Special Topics - Accelerators and Beams **11**, 040701 (2008).
[34] A. Dubinov, Plasma Physics Reports **33**, 210 (2007).
[35] H. Suk, in *Department of Electrical and Computer Engineering* (University of Maryland, College Park, 1996).
[36] J. Bisognano *et al.*, Nuclear Science, IEEE Transactions on **28**, 2513 (1981).
[37] H. Washimi, and T. Taniuti, Physical Review Letters **17**, 996 (1966).
[38] R. A. Kishek *et al.*, Nuclear Instruments and Methods in Physics Research Section A: Accelerators, Spectrometers, Detectors and Associated Equipment **544**, 179 (2005).
[39] S. Bernal *et al.*, in 13th Workshop on Advanced Accelerator Concepts (AAC) (New York: AIP Press, Santa Cruz, CA, 2008).
[40] J. Thangaraj, in *Electrical and Computer Engineerin* (University of Maryland College Park, 2006).
[41] C. Wu, in *Electrical and Computer Engineering* (University of Maryland College Park, 2008).
[42] D. Feldman *et al.*, Proceedings of the Particle Accelerator Conference, 2001. .
[43] J. R. Pierce, Journal of Applied Physics **11**, 548 (1940).
[44] D. Stratakis, in *Department of Electrical and Computer Engineering* (University of Maryland, College Park, 2008).
[45] C. D. Child, Physical Review (Series I) **32**, 492 (1911).
[46] I. Langmuir, Physical Review **2**, 450 (1913).
[47] ContinuumLasers, Inc. Minilite II Catalog, Santa Clara,CA.
[48] B. Quinn *et al.*, in Particle Accelerator Conference, 2003. PAC 2003. Proceedings of the2003), pp. 2571.
[49] K. Fiuza *et al.*, in 11th European Particle Accelerator ConferenceGenoa, Italy, (2008).
[50] L. Imaging, Lexel Imaging (http://www.lexelimaging.com/).
[51] P. Instruments, Princeton Instruments Inc.(PIMAX).
[52] K. Tian *et al.*, Physical Review Special Topics - Accelerators and Beams **9**, 014201 (2006).
[53] J. G. Wang, and M. Reiser, Review of Scientific Instruments **65**, 3444 (1994).
[54] R. Kishek, Program to calculate centroid,beam size from camera images (*Private communication*).
[55] S. Bernal *et al.*, in 45th Annual Meeting of the APS Division of Plasma Physics (AIP, Albuquerque, New Mexico (USA), 2004), pp. 2907.
[56] J. Harris *et al.*, Physical Review E **76**, 26402 (2007).
[57] R. A. Kishek, and K. Fiuza, Acceleraton in UMER, Technical note (2009)).
[58] G. Whitham, *Linear and Nonlinear waves* (John Wiley & Sons, Inc., 1974).
[59] Murawski.K., *Analytical and Numerical Methods for Wave Propagation in Fluid Media* (World Scientific Publishing Company, 2003).
[60] J. M. Dawson, Physical Review **113**, 383 (1959).
[61] S. P. D. Mangles *et al.*, Nature **431**, 535 (2004).
[62] W. B. Mori, and T. Katsouleas, Physica Scripta, 127 (1990).
[63] B. Salzberg, and A. Haeff, RCA Review **2** (1938).
[64] C. Fay, A. Samuel, and W. Shockley, Bell System Technical Journal **17**, 49 (1938).

[65] C. K. Birdsall, and W. B. Bridges, *Electron Dynamics of Diode Regions* (Academic Press, New York, 1966).
[66] J. Lomax, Proc. I.E.E. (London) **108**, 119 (1981).
[67] C. K. Birdsall, and W. B. Bridges, Journal of Applied Physics **32**, 2611 (1961).
[68] J. W. Luginsland, Y. Y. Lau, and R. M. Gilgenbach, Physical Review Letters **77**, 4668 (1996).
[69] D. J. Sullivan, J. E. Walsh, and E. A. Coutsias, in *High-Power Microwave Sources*, edited by V. L. Granatstein, and I. Alexeff (Artech House, Inc., Norwood, MA, 1987).